Mikko Leino

Integrating Phase Shifters in a Waveguide-fed Antenna Array

School of Electrical Engineering

Thesis submitted for examination for the degree of Master of Science in Technology.

Espoo 23.1.2017

Thesis supervisor:

Prof. Ville Viikari

Thesis advisor:

D.Sc. (Tech.) Juha Ala-Laurinaho

Aalto University
School of Electrical
Engineering

AALTO UNIVERSITY
SCHOOL OF ELECTRICAL ENGINEERING

ABSTRACT OF THE
MASTER'S THESIS

Author: Mikko Leino

Title: Integrating Phase Shifters in a Waveguide-fed Antenna Array

Date: 23.1.2017 Language: English Number of pages: 9+80

Department of Electronics and nanoengineering

Professorship: Radio Science and Engineering Code: ELEC3038

Supervisor: Prof. Ville Viikari

Advisor: D.Sc. (Tech.) Juha Ala-Laurinaho

In this master's thesis, phase shifter integration for the future 5G base station antennas is studied using electromagnetic simulations and measurements. The integration is done for two antenna prototypes, which operate at 71–86 GHz band (E-band) and 26–30 GHz band (cm-band), respectively.

The base station antenna is a waveguide-fed phased array and the phase shifters are integrated on a PCB, which is installed between the feeding network and a horn antenna array. Two waveguide-to-microstrip transitions are designed and simulated for both frequency bands. The average insertion losses of the transitions are 0.7 dB at E-band, and 0.35 dB at cm-band, confirming suitability for the antenna prototypes. A sensitivity analysis of the main transition parameters suggests that manufacturing precision should be ±30 µm at E-band and ±50 µm at cm-band, respectively.

Fixed microstrip line-based true time delay phase shifters are designed for E-band. Their performance is validated by simulations and measurements. The results show that the phase shifters have full 360°phase shift range for the beam-steering demonstration of the prototype antenna.

TGP2100 phase shifters from TriQuint are used for cm-band. A test structure is fabricated and measured to characterize the phase shifter but it is damaged during the phase shifter installation. Other test structures are designed and measured to evaluate losses due to wire bonding of the phase shifter to the PCB. The measurement results show the insertion loss from the wire bonding is around 4 dB. Also, a phase shifter test structure made by Nokia Bell Labs is simulated and measured. The results show that the used phase shifter simulation model does not predict the phase shifter performance correctly when the RF-grounding is defected e.g. due to unsuitable glue or solder. The simulations indicate that the main source of antenna prototype transmission losses are the phase shifters. Still, the phase shifters are suitable for the beam-steering demonstration. Future work includes fabricating the final antenna prototype for the cm-band and its measurements.

Keywords: Beam-steering, cm-band, E-band, Phase shifter, Phased array, Waveguide-to-microstrip transition, 5G

AALTO-YLIOPISTO
SÄHKÖTEKNIIKAN KORKEAKOULU

DIPLOMITYÖN
TIIVISTELMÄ

Tekijä: Mikko Leino

Työn nimi: Vaiheensiirtimien integrointi aaltoputkiohjattuun antenniryhmään

Päivämäärä: 23.1.2017 Kieli: englanti Sivumäärä: 9+80

Elektroniikan ja nanotekniikan laitos

Professuuri: Radiotiede ja -tekniikka Koodi: ELEC3038

Valvoja: Prof. Ville Viikari

Ohjaaja: TkT Juha Ala-Laurinaho

Tässä diplomityössä on tutkittu vaiheensiirtimien integrointia tulevaisuuden 5G tukiasema-antenneihin käyttäen apuna sähkömagneettisia simulaatioita ja mittauksia. Integrointi on toteutettu kahdelle antenniprototyypille, jotka toimivat 71–86 GHz (E-kaista) ja 26–30 GHz (cm-kaista) taajuuksilla.

Tukiasema-antenni on aaltoputkilla syötetty, vaiheohjattu antenniryhmä ja vaiheensiirtimet integroidaan piirilevylle, joka asennetaan syöttöverkon ja torviantenniryhmän väliin. Kaksi aaltoputki-mikroliuska-siirtymää on suunniteltu ja simuloitu molemmille taajuuskaistoille. Simulaatiotulokset osoittavat, että siirtymillä on pienet keskimääräiset väliinkytkemisvaimennukset: 0,7 dB E-kaistalla ja 0,35 dB cm-kaistalla, joten ne sopivat käytettäväksi antenniprototyypeissä. Siirtymän tärkeimmistä mitoista tehty herkkyysanalyysi osoittaa että ±30 µm valmistustarkkuus on riittävä E-kaistalle ja ±50 µm valmistustarkkuus cm-kaistalle.

Kiinteät mikroliuskapohjaiset vaiheensiirtimet on suunniteltu E-kaistalle. Niiden toiminnallisuus on varmistettu simuloinneilla ja mittauksilla. Tulokset osoittavat, että vaiheensiirtimillä voidaan toteuttaa 360°:een vaiheensiirto ja ne sopivat käytettäväksi prototyyppiantennin vaiheistamiseen.

TriQuintin valmistamia TGP2100-vaiheensiirtimiä käytetään cm-kaistalla. Testirakenne valmistettiin vaiheensiirtimen karakterisointia varten, mutta testialustalle asennetun vaiheensiirtimen havaittiin olevan vahingoittunut. Muita testirakenteita on suunniteltu ja mitattu vaiheensiirtimen lankabondauksesta johtuvien häviöiden selvittämiseksi: lankabondauksesta aiheutuu noin 4 dB:n häviöt. Lisäksi Nokia Bell Labsin valmistama testirakenne on simuloitu ja mitattu. Tuloksista nähdään, että vaiheensiirtimen simulaatiomalli ei toimi oletetulla tavalla, jos vaiheensiirtimen RF-maadoitus on viallinen. Tämä voi johtua esimerkiksi sopimattomasta liimasta tai juotteesta. Simulaatiot osoittavat, että vaiheensiirtimet ovat antenniprototyyppien pääasiallinen siirtohäviölähde, mutta ne sopivat antennin vaiheistamisen esittelyyn. Tutkimusta aiotaan jatkaa valmistamalla antenniprototyyppi cm-kaistalle ja mittaamalla sen toiminta.

Avainsanat: Aaltoputki-mikroliuska siirtymä, cm-kaista, E-kaista, Keilansäätö, Vaiheensiirrin, Vaiheistettu antenniryhmä, 5G

Preface

My thesis is finally done and the final part of my studies is coming to an end. This thesis reflects quite well my seven-year long studies here in Aalto: It took some time, but I did it with my whole heart. I am very proud of what I have done and I regret nothing.

First, I want to thank my supervisor, Prof. Ville Viikari, for letting me work in his research group and giving me this challenging topic, and for his valuable comments and for his continuous support throughout the whole journey. This work is done in collaboration with Nokia Bell Labs and I want to thank everyone, who I have had chance to work with from there. I want to thank my advisor D.Sc. (Tech.) Juha Ala-Laurinaho for listening my problems with the thesis and for his valuable comments and feedback that helped to make this thesis what it is. Also, thanks goes to everyone in Professor Viikari's research group for helping me at the times I needed the help most and for encouraging me towards the end.

Many people have influenced my time here in Otaniemi. They have reminded me that studying is not always the most important thing on the list: networking is sometimes as important and of course you should always enjoy your life. I have met so many people, who have influenced me, but I would especially like to thank Ismo and Joni for their valuable friendship. It is very important for me to know that you are there and I can always count on you. I would also like to thank all the groups that I've been member to: HTMK11, ITMK12, SIKH13, FTMK13, SIK-fuksit13, FTMK14, Teekkarijaosto 14 and 15, and Polytechnical Students' Museum. Special thanks goes to Vapaateekkarit for giving me adventures I could have never imagined. And similar thanks goes to Autokoulu Sompaveikko, its leader Veikko Sompa and all the driving school students that have been spending Kimble time with me.

My relatives and family have been supporting me my whole life. I want to thank my mother and father for always believing in me and taking care of me, and I want to thank my brother Tuomo for being the best little brother there could be. Also, I want to thank the the two furballs Maxwell and Boltzmann, who are nothing like their namesakes and bring constant joy to my life.

Finally, the most sincerest and loving thanks I point to my beloved Riina. Without you I could have never done this, thank for your love and support. You are the most important to me and you make me very happy each day.

Iuvenis in Aeternum! Tekniikan kehdossa, 23.1.2017

Mikko K. Leino

Contents

Symbols and Abbreviations

Symbols

a	width of the rectangular waveguide [mm]
b	height of the rectangular waveguide [mm]
b_{tapered}	height of the tapered rectangular waveguide [mm]
C, C'	capacitance of the capacitor and the variable capacitor, respectively [F]
c	speed of light in vacuum $\approx 3 \cdot 10^8$ [m/s]
d	via diameter in the substrate integrated waveguide [µm]
d_x, d_y	antenna array row and column spacing, respectively [mm]
d_1	microstrip length inside the feeding network waveguide [mm]
d_2	microstrip length inside the antenna feed waveguide [mm]
f	frequency [GHz]
f_c, $f_{c,mn}$	cut-off frequency [GHz]
$f_{c,10}$	cut-off frequency of the TE_{10} mode [GHz]
f_p	$Z_0/(2\mu_0 h)$ [GHz]
f_T	cut-off frequency for the lowest order TM-mode in microstrip line [GHz]
f_{CT}	cut-off frequency for a transverse resonance [GHz]
G	empirical factor suggested to be $0.6 + 0.009Z_0$
h	substrate thickness [mm]
h_1	microstrip distance from the short end of the feeding network [mm]
h_2	microstrip distance from the short end of the antenna feed [mm]
I_{mn}	amplitude of the excitation current signal for the array element [A]
j	imaginary unit
l	microstrip line length [mm]
L	inductance [H]
M	number of rows in the antenna array
m	positive integer
N	number of columns in the antenna array
n	positive integer
p	period length of the SIW [mm]
P_p	power flown down the waveguide [W]
r	positive real number
R_s	surface resistivity of the conductor [Ω]
s	ground plane distance from the stripline [mm]
t	microstrip line thickness [µm]
T	periodic time [s]
t_0	transmission time for a constant phase point [s]
$\tan\delta$	loss tangent
U	voltage obtained by integrating the electric field over the cross section of the waveguide [V]
v_p	phase velocity [m/s]
w	microstrip line width [mm]
x	varied length for the E-band phase shifter [mm]

x, y, z	Cartesian coordinates
Z_0	characteristic impedance of the microstrip line [Ω]
Z_{TE10}	characteristic impedance for the TE_{10} mode wave [Ω]
$Z_{0\mathrm{TE10}}$	characteristic impedance of the waveguide supporting the TE_{10} mode [Ω]
α_c	attenuation constant due to conductor loss [Np/m]
$\alpha_{c\mathrm{TE10}}$	attenuation constant for the TE_{10} mode [Np/m]
α_d	attenuation constant due to dielectric loss [Np/m]
α_{mn}	phase term of the array factor [m]
β	propagation constant or wave number [1/m]
Δf	frequency change [GHz]
$\Delta\theta$	beam squint angle [°]
ε	permittivity [F/m]
ε_r	relative permittivity or dielectric constant
ε_{reff}	effective dielectric constant
ε_0	permittivity in vacuum $\approx 8.854 \cdot 10^{-12}$ [F/m]
η	intrinsic impedance [Ω]
θ	elevation angle [°]
θ_0	elevation angle of main beam pointing direction [°]
λ	wavelength [mm]
λ_0	wavelength in the vacuum [mm]
μ	permeability [H/m]
μ_0	permeability in vacuum $= 4\pi \cdot 10^{-7}$ [H/m]
ξ_{mn}	element distribution term of the array factor [m]
π	mathematical constant Pi ≈ 3.14159
σ	conductivity [S/m]
ϕ	azimuth angle [°]
ϕ_0	azimuth angle of main beam pointing direction [°]
φ	phase of the electromagnetic wave [rad]
ω	angular frequency [rad/s]

Abbreviations

AF	array factor
BST	barium strontium titanate
CBCPW	conductor-backed coplanar waveguide
CPW	coplanar waveguide
CST	computer simulation technology, electromagnetic simulation software
DC	direct current
DRL	dual resonant load
EM	electromagnetic
FDTD	finite difference time domain
GaAs	gallium arsenide
IC	integrated circuit
InP	indium phosphide
I/O	input/output
LLPS	loaded-line phase shifter
MEMS	micro electro mechanical systems
MMIC	monolithic microwave integrated circuit
mm-wave	millimeter wave
MOSFET	metal-oxide-semiconductor field-effect transistor
NBL	Nokia Bell Labs (not official abbreviation)
NI AWR	National Instruments Applied Wave Research, circuit simulation and design software
PCB	printed circuit board
PEC	perfect electric conductor
PTFE	polytetrafluoroethylene, Teflon is the best known brand name
QTEM	quasi-TEM
RF	radio frequency
RMS	root mean square
RTPS	reflection-type phase shifter
RWG	rectangular waveguide
SiGe	silicon-germanium
SIW	substrate integrated waveguide
SLPS	switched-line phase shifter
S-parameter	scattering parameter
SPDT	single pole, double throw
SPST	single pole, single throw
TE	transverse electric
TEM	transverse eletromagnetic
TM	transverse magnetic
VGA	variable gain amplifier
WR-xx	EIA standardized rectangular waveguides
3D	three dimensional
5G	5th generation mobile networks

1 Introduction

The wireless data traffic has been steadily increasing for past several years and mobile devices are increasingly used for other purposes than traditional calls and text messages. The global mobile data traffic is predicted to increase 53% annually between 2015 and 2020, mainly due to increased video streaming [1]. The existing mobile networks cannot meet the capacity and higher data rate demands of the increasing data traffic.

The fifth generation mobile communication networks (5G) have been intensively developed during the past few years [2] and the new standardized systems are expected to come into use by 2020. Generally accepted ways to increase the capacity and lower the latency include wider spectral band, denser networks with more cells, and higher spectral efficiency [3]–[6]. More spectrum and wider bandwidths are available at frequencies higher than those conventionally used for mobile communications.

Millimeter-wave frequencies such as 28, 38, 60 GHz and E-band (71–76 and 81–86 GHz) have been proposed to be used in 5G communications [6]. However, at the proposed millimeter-wave frequencies, the propagation losses are higher and the range of communication is limited if the antenna gain is not increased. Also, to have lower latencies, more access points are required for end users. This is achieved with denser networks by shrinking the cell size and thus, increasing the number of base stations. Therefore, the base station antenna solutions are required to be of low-cost, have low power consumption, and have small size for discrete installation. Furthermore, the new networks should support wireless backhauling, as the wired connections to the antennas would restrict the installation and be costly. The requirements and challenges for wireless millimeter-wave backhauling are discussed in [7].

The higher efficiency necessitates that the radiated power is efficiently directed to the mobile terminals which are often moving. The beam direction of the base station antenna must be reconfigurable so that it can follow moving user. Furthermore, the limited range of the communications requires high antenna gain to maximize the link budget [8].

The antenna beam can be electrically steered at mm-waves in several ways: e.g. with beam switching networks, reconfigurable high impedance surfaces, phase shifting, and time-delay networks. Several antenna types with electrical beam-steering have been proposed. These include: integrated lens antennas [9], passive beamforming networks like the Rotman lens [10], leaky wave antennas [11], reconfigurable reflectarrays [12], and phased arrays [13]. However, none of these solutions can simultaneously offer all the desired features.

The antenna solution potentially capable of offering all the wanted benefits is presented here. The design prototypes are done in collaboration with Nokia Bell Labs, and the requirements set for the base station antenna are the following:

- Operating frequency 26–30 GHz (referred to as cm-band in the thesis), or operating frequency 71–86 GHz (i.e. E-band).
- Low profile and small physical size.

- Electronically steerable in the range of $\pm 45°$.
- Low switching time (< 1 µs).
- 20-40 dBi gain.

To answer the requirements, a new kind of base station antenna is proposed. The proposed antenna is partly based on another antenna earlier studied at Aalto University [14]. The general outline can be seen in Figure 1. Obviously, two different structures are required for two different operation bands. Nonetheless, the design of both antennas are somewhat similar: the main difference is the physical dimensions, which are relative to the wave length. The presented structures consists of three parts:

- Feeding network.
- PCB for phase shifters.
- Horn antenna array.

The proposed system has potentially low losses, low profile, wide beam-steering range, and high gain. Furthermore, all the elements in the array are identical, and thus, the phased array is also scalable. Finally, the antenna and the feeding network support low-cost plastic injection molding manufacturing techniques followed by metallization. These techniques could prove to facilitate the manufacturing process substantially and allow precise manufacturing with low cost.

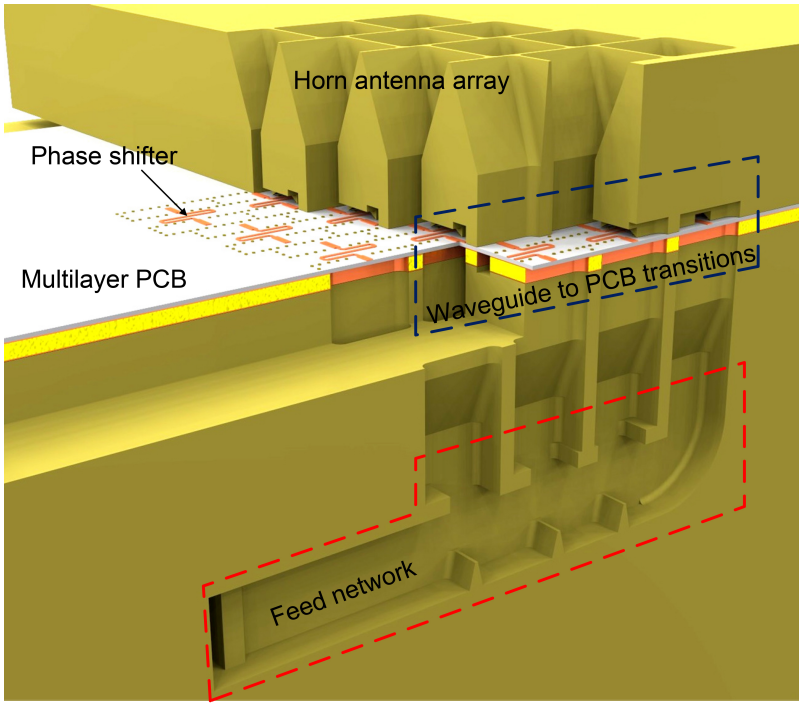

Figure 1: General outline of the proposed phased array system. From bottom to top it consists of the waveguide feeding network, the PCB for the phase shifters, and the horn antenna array. Figure by Eino Kahra.

Antenna prototypes are fabricated for E- and cm-band to verify that the presented system is feasible and suitable for upcoming 5G networks. The designed structures are 4 by 4 arrays ideally providing 20-dBi gain. As the design is scalable, the array can be expanded for example up to 100 elements to improve the array gain. These smaller versions related to this thesis are used to study the feasibility of the concept.

The feeding network and the horn antenna array are based on rectangular waveguides to have low losses at high operating frequencies. Horn antennas are chosen as array elements because they have high efficiency. The feeding network and antenna part for E-band were designed previously by the researchers at Aalto University and they are presented in [15]. The cm-band structures were designed by Mr. Resti Montoya Moreno in his Master's Thesis [16].

The phase shifters are required to electrically control the array beam, and a planar transmission line structure is required for the phase shifter implementation. The phase shifters are integrated on the same PCB, which is used throughout the whole antenna to make the antenna assembly is more straightforward. However, low-loss transitions between the microstrip lines on the PCB and waveguide structures are required as both transmission line structures are adopted in the design.

The main objective of this thesis is on integrating the phase shifters in the presented E-band and cm-band antenna prototypes. The phase shifter integration is highly related to the previously discussed transitions and the transition structure designs are presented. Furthermore, the methods for phase shifter characterization are shown for both E-band and cm-band. Additionally, the different phase shifters at the millimeter-wave frequencies are described.

This thesis has the following structure. Chapter 2 presents the basic components related to the 5G base station antenna, which includes phased antenna arrays and different feeding network structures. As the electrically beam-steered antenna relies heavy on the utilized phase shifter, an extensive survey of available phase shifters at the millimeter waves is presented. Additionally, the used electromagnetic simulation tools are described. Chapter 3 explains the transitions between the waveguides and the PCB that are required for the phase shifter integration. The transitions are discussed for both E-band and cm-band and the simulated results of their performance are given. Chapter 4 presents the designed phase shifter for E-band and the simulations and measurements related to it. For the cm-band, the chosen commercial phase shifter is evaluated and the simulations and different test structures for the phase shifter characterization are discussed. Finally Chapter 5 gives some summarizing notes and concludes the thesis.

2 Background

2.1 Beam-Steerable Antennas

Radiation pattern, which is one key antenna characteristic, describes how an antenna spreads the energy fed to it in angular domain, and it is defined in the far-field [17], [18]. For an ideal dipole or monopole the radiation pattern is omnidirectional, but generally the antenna radiates to one direction better than to the others. Towards this direction the main lobe or the main beam of the antenna is formed. The beam-steering refers to the user-controlled change of the main radiation direction.

A beam-steering antenna can be implemented in several ways. Mechanical steering of an aperture antenna, such as reflector antenna, is a traditional way to realize a scanning beam [17]. However, the realization of the mechanical structure to control the antenna can be large, costly, and it requires constant maintenance. More importantly, the approach limits the scanning rate to the mechanical speed of changing the antenna orientation.

The radiation pattern of an antenna array can be shaped through element spacing and excitation. Furthermore, the main beam can be steered by electronically adjusting the excitations phases. These kinds of antenna structures are referred to as phased arrays [17]–[19]. Electronic beam-steering is typically much faster than mechanical one and therefore preferred in the mobile communication systems. This section focuses on beam-steerable phased-array antennas and their characteristics.

2.1.1 Antenna Arrays

An antenna array is constructed by multiple antenna elements in a single structure as presented in [17] and [18]. The total radiation field is achieved by superpositioning the vector fields of the individual elements together in the far-field. Phase and amplitude of each element are selected such that the fields add constructively in the wanted main beam radiation direction and destructively in other directions. The phased arrays can be used instead of a single antenna when a precise control of the radiation pattern is desired. With similar antenna elements in the array, the radiation pattern of the array can be controlled with the element spacing and excitation. Other antenna array traits are that they tend to be fairly directive and thus, have a high gain. In the case of a single antenna, the increase of the directivity requires larger antenna aperture size. With array antennas the individual element sizes can be maintained small and the directivity can be increased by adding more elements to the array. The array elements can differ from each other, but generally similar elements are used as it is more convenient, simpler, and practical.

As concluded before, the physical movement of the antenna is hardly a suitable feature for a fast and continuous beam-control. The excitation phase adjustment provides faster and more precise control over the scanning. Although this requires a more complex feeding network the trade-off is affordable. The excitation signal can be controlled either with variable phase or with true time delay [18]. These controlling schemes are more closely inspected in section 2.3. In addition to the scanning rate, the other important antenna characteristics of phased arrays include

the gain, beamwidth, sidelobe level, and bandwidth [19]. These characteristics depend on the chosen elements, the geometrical configuration of the array, and the relative displacement of the elements, along with the excitation phase, amplitude, and radiation pattern of the individual elements. In the following review, the array elements are assumed to be identical and their mutual coupling in the near-field is neglected to simplify the array inspection. In reality, the elements have different performance depending on their location in the array - generally the elements near the edges do not have as strong mutual coupling as the ones in the middle [18].

For construction of the basic array model, the performance of the single element and the ideal array with isotropic radiators is needed. Radiation properties of an array depend on the radiation properties of array elements, element locations, and amplitude and phase of excitation signal of each element. The effect of the single element in an array is taken into account in the element pattern, which describes the radiation pattern provided by the element. Furthermore, the array factor (AF) describes the radiation pattern of the array when the elements are replaced with isotropic point sources. The final model is the product of these two if the array elements have the same pattern and are similarly oriented [17]. The array elements considered in this thesis are pyramidal horn antennas, which have square apertures. The horn antennas are known for their high gain, and thus, they are suitable for high gain arrays. They have generally rectangular waveguide-based feeding networks which are discussed later in the section 2.2.3. As the element pattern of such antenna is not affected by the excitation phase, the further inspection of the element pattern is neglected here. Further analysis can be found in [17].

Linear, equispaced array is very traditional array geometry which is described in [17] and [18]. However, the arrays discussed here are planar. Equispaced planar array is used if beam-steering is required in two orthogonal directions. The behaviour of such array can be simplified by treating it as a sum of two linear arrays. The two-dimensional array has an advantage of two-dimensional scanning range and higher gain compared to the linear arrays. The geometrical configuration of the elements in the planar array can be, for example, circular, rectangular, or triangular. In this thesis, the presented arrays are rectangular with identical elements, which have equal row and column spacing $d_x = d_y$. Thus the array is said to be square. An array with M rows and N columns is considered in the following. Such an array is presented in Figure 2, which also describes the coordinate system that is utilized in phased array analysis. The amplitude of the excitation current signal for each element is denoted as I_{mn}. The array factor for a square array as a function of the elevation angle θ and the azimuth angle ϕ is [17]

$$AF(\theta, \phi) = \sum_{n=0}^{N-1} \sum_{m=0}^{M-1} I_{mn} e^{j\beta(\xi_{mn} - \alpha_{mn})} \tag{1}$$

where

$$\xi_{mn} = m d_x \sin\theta \cos\phi + n d_y \sin\theta \sin\phi \quad \text{and}$$
$$\alpha_{mn} = m d_x \sin\theta_0 \cos\phi_0 + n d_y \sin\theta_0 \sin\phi_0.$$

β denotes the wave number of the radiating field and ξ_{mn} denotes the effect of the array element distribution. α_{mn} on the other hand denotes the effect of the excitation phase shift between elements, whereas θ_0 and ϕ_0 describe the main beam pointing direction which is controlled by the phase shifters.

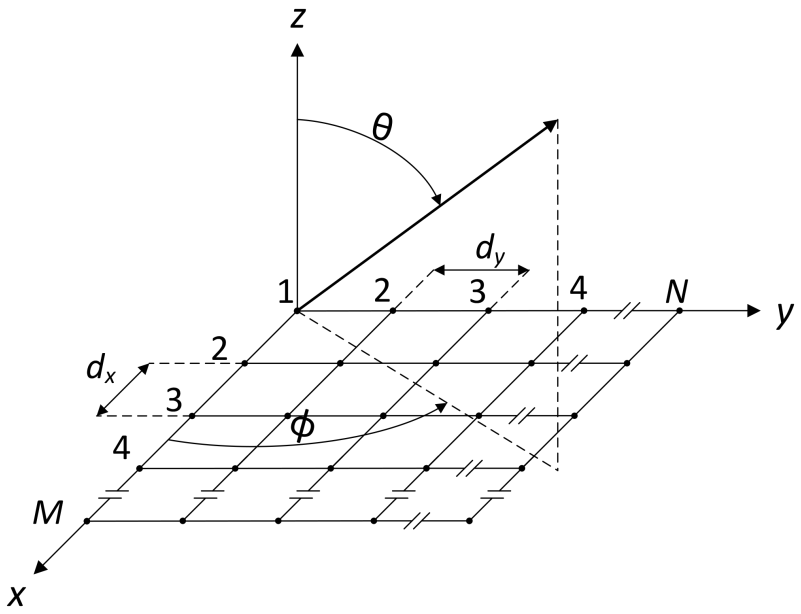

Figure 2: Planar array with M rows and N columns. The main radiation direction of the array is the z-axis. The elements are distributed evenly over the xy-plane with spacing of d_x and d_y accordingly. θ and ϕ are the variables over which the array factor is investigated. Adapted from [18].

If the steering angle is too large for the chosen element spacing, far-fields of array elements add constructively in other directions in addition to the main beam direction. These other strong lobes are referred to as grating lobes and they are typically avoided as they increase the sidelobe level of the array. To avoid grating lobes appearing in the visible region of the array, the following condition is required [17]

$$d_{x/y} < \frac{\lambda}{1 + |\sin\theta_0|}. \tag{2}$$

Equation (2) shows that the element spacing must be equal or less than $\lambda/2$, if 180° scanning is required. Here λ is the wavelength at the operating frequency and θ_0 is the main beam pointing angle.

The increased sidelobe level can be sometimes compensated by choosing alternate array grid geometry, notably the triangular lattice. Other way to improve array performance is by tapering the array excitation so that the center elements are excited more strongly than the ones near the array boundaries. This manipulation of the excitation distribution typically increases the beamwidth of the array. Further examination of the array beam-forming can be found in [19]. There is also a quite extensive review of the phased array error forming. The decreased phased array performance due to the amplitude and phase errors include: the increased sidelobe

level, the beam pointing errors, and the decreased directivity. However, further error analysis is neglected in this thesis.

As shown in (1), the phased array beam can be used for scanning the arbitrary space by varying the excitation phase of the array elements. This is achieved by utilizing phase shifters, which are more profoundly described in 2.3. The phase shift is desired to be done in the RF-path as each element must be controlled separately. Therefore, a common feeding network distributing the signal from the transceiver to each antenna element is required. Possible feeding networks for the phased arrays in micro- and millimeter waves are described in the following section.

2.2 Feeding Network

Planar transmission lines and waveguide structures are the main methods to transfer the micro- and millimeter wave signals. From the application point of view, the main characteristics of feeding networks include the losses, bandwidth, size, and the capability to integrate components [20]. Furthermore, the knowledge of the wave modes related to the different transmission line structures is required for the analytical examination.

The waves related to these structures are transverse electromagnetic (TEM), transverse electric (TE), and transverse magnetic (TM) waves. TEM waves can exist for example in the coplanar waveguides. They do not have longitudinal electric or magnetic field components to the propagation direction, only the transversal field components. The waves propagating in the microstrip lines can be approximated by the TEM waves as the field components are almost transversal. These waves are called quasi-TEM (QTEM). Waveguides on the other hand support TE or TM waves depending of the waveguide structure and dimensions. TE and TM waves have the longitudinal magnetic or electric field components, respectively, according to the transversal field component. The different waves are more profoundly discussed in [21] and [22].

The planar transmission lines and waveguides considered in this thesis are a microstrip line and a coplanar waveguide (planar structures), and a rectangular waveguide and a substrate integrated waveguide (SIW) (waveguide structures). Firstly, the microstrip line is examined.

2.2.1 Microstrip Line

The microstrip line is the most popular planar transmission line and it is described in many textbooks [20]–[24]. Planar transmission lines are straightforward to manufacture for example with photolithographic processes and can be quite easily miniaturized compared to the waveguides and the coaxial lines. Additionally, the integration of the microwave components to the planar lines is very facile. However they have strong attenuation and high losses. This makes the utilization of the large planar transmission line feeding networks impractical if the power consumption is of importance.

Figure 3 shows the geometry of the microstrip line structure. The structure consists of a conducting signal line with the thickness of t and the width of w, and the ground plane. Conducting planes are separated by a dielectric layer (substrate) with the thickness of h. Substrates are typically evaluated by their loss tangent $\tan\delta$ and dielectric constant or relative permittivity ε_r [20]. Dielectric losses in the microstrip line are typically less than ohmic ones. The loss tangent is the main contributor to the dielectric attenuation constant as will be shown later on. The relative permittivity affects the physical dimensions of the microstrip line and is also an important parameter.

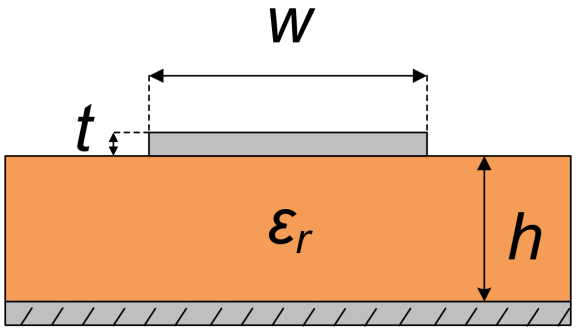

Figure 3: Microstrip line structure.

If the medium around the microstrip is homogeneous, the line supports a pure TEM wave and the characteristic impedance is related to the dielectric constant of the medium. However, the fields in the microstrip line propagate partly in the substrate and partly in the medium above the signal line, which is usually air. For further notice, the actual wave in the microstrip line is a hybrid TM-TE wave, but with a thin substrate the propagating wave can be assumed to be quasi-TEM [21]. To correlate with the authentic circumstances, the dielectric constant must be replaced with the effective dielectric constant ε_{reff} which satisfies the following relation [21]

$$1 < \varepsilon_{reff} < \varepsilon_r. \tag{3}$$

The effective dielectric constant can be approximated by [21]

$$\varepsilon_{reff} = \frac{\varepsilon_r + 1}{2} + \frac{\varepsilon_r - 1}{2}\frac{1}{\sqrt{1 + 12h/w}}. \tag{4}$$

The microstrip lines are often designed for a certain characteristic impedance for the application purposes. Also, the available substrates and their properties are normally known. The literature presents several formulas for the microstrip line dimensioning and the following formulas yield an approximate solution for the w/h-relation when the characteristic impedance of the line Z_0 and the dielectric constant of the substrate ε_r are known. The following equation is adapted from [20].

$$\frac{w}{h} = \begin{cases} \dfrac{8e^A}{e^{2A} - 2} & \text{for } w/h < 2 \\ \dfrac{\pi}{2}\left[B - 1 - \ln(2B-1) + \dfrac{\varepsilon_r - 1}{2\varepsilon_r}\{\ln(B-1) + C\}\right] & \text{for } w/h > 2 \end{cases} \tag{5}$$

where

$$A = \frac{Z_0}{60}\sqrt{\frac{\varepsilon_r + 1}{2}} + \frac{\varepsilon_r - 1}{\varepsilon_r + 1}\left(0.23 + \frac{0.11}{\varepsilon_r}\right),$$
$$B = \frac{377\pi}{Z_0\sqrt{\varepsilon_r}},$$
$$C = 0.39 - \frac{0.61}{\varepsilon_r}.$$

The aforementioned formulas assume the stripline thickness to be zero. In the real microstrip line the increase in the thickness increases the stripline capacitance which decreases the characteristic impedance of the line. This indicates that the effective width of the microstrip line is a bit wider than the actual width of the line. Also, the increase in the microstrip thickness suggests that the greater share of the propagating wave is in the medium above the substrate thus decreasing the effective dielectric constant according to [24]

$$\varepsilon_{reff}(t) = \varepsilon_{reff} - \frac{(\varepsilon_r - 1)t/h}{4.6\sqrt{w/h}}. \tag{6}$$

Furthermore, the effective dielectric constant is affected by the frequency dispersion of the line. The increase of the frequency f distorts the propagating wave and the waveform begins to resemble more a hybrid form than a quasi-TEM. The longitudinal field components become more significant and this causes the fields to be centered in the substrate. Thus, the effective dielectric constant is actually increased by the dispersion and it approaches the dielectric constant of the substrate. The frequency dependence of the ε_{reff} can be approximated by [24]

$$\varepsilon_{reff}(f) = \varepsilon_r - \frac{\varepsilon_r - \varepsilon_{reff}}{1 + G(f/f_p)^2} \tag{7}$$

where $f_p = Z_0/(2\mu_0 h)$ and the G is an empirical factor suggested to be $G = 0.6 + 0.009Z_0$.

The attenuation in the microstrip line is mainly caused by the conductor loss, the dielectric loss, and the microstrip line radiation. The radiation is not a desired feature especially in an antenna feeding network. To prevent this, the microstrip line can be enclosed with a metallic cover or the antenna can be otherwise shielded from the disturbing radiation. Of the aforementioned losses, the conductor loss is often the dominating one. The attenuation constant due to conductor loss is given by [20]

$$\alpha_c = \frac{R_s}{Z_0 w} \tag{8}$$

where $R_s = \sqrt{\pi f \mu_0/\sigma}$ is the surface resistance of the conductor. The σ is the conductivity of the conductor. The attenuation constant due to dielectric loss originated from the substrate is [20]

$$\alpha_d = \pi \frac{\varepsilon_r(\varepsilon_{reff} - 1)}{\sqrt{\varepsilon_{reff}}(\varepsilon_r - 1)} \frac{\tan\delta}{\lambda_0} \tag{9}$$

where λ_0 is the wavelength in vacuum.

Additionally, the microstrip lines might encounter difficulties at higher frequencies with the higher order modes. The TM and TE surface waves can be excited along the substrate and they are particularly problematic if the power from the desired microstrip wave modes couples to them. The coupling to the lowest order TM-mode is strong at the frequencies above [21]

$$f_T = \frac{c \arctan \varepsilon_r}{\sqrt{2}\pi h \sqrt{\varepsilon_r - 1}}. \tag{10}$$

Moreover, if the microstrip is particularly wide, a possibility of a transverse resonance is imminent. The cut-off frequency for a transverse resonance is [23]

$$f_{CT} = \frac{c}{2\sqrt{\varepsilon_r}(w + 0.4h)}. \tag{11}$$

To prevent power coupling to these modes, the operation frequency of the microstrip line must be chosen to be less than both f_T and f_{CT}. Formulas (4)–(11) present approximate solutions to support the microstrip line design and they are from the time before the computer aided design. However, the formulas provide an adequate insight to the different parameter effects to the microstrip line performance. Nowadays, there are multiple simulation tools to help an RF-engineer to design a proper microstrip line structure. In this thesis, TX-LINE® transmission line calculator from NI-AWR Design Environment is used to calculate the initial values for the microstrip line dimensions. Subsequently, the values are verified and the attenuation is calculated in the 3D EM-simulation software.

The preceding paragraphs do not discuss the signal phase behaviour in the microstrip line, which is obviously a significant factor for a feeding network that is used in a phased antenna array. The phase delay due to a microstrip line of a certain length depends on the propagation constant β. For the microstrip line, the propagation constant can be calculated by the following assuming the TEM wave propagation [20]

$$\beta = \frac{2\pi}{\lambda} = \omega\sqrt{\mu\varepsilon_0\varepsilon_{reff}}. \tag{12}$$

Furthermore, the propagation constant is related to the phase velocity, which dictates at what speed a constant phase point travels on the microstrip line. The phase velocity is [20]

$$v_p = \frac{\omega}{\beta} = \frac{c}{\sqrt{\varepsilon_{reff}}}. \tag{13}$$

Equation (13) shows that the phase velocity is inversely proportional to the square root of the effective dielectric constant of the substrate.

As the phase propagates at a definite velocity, the different lengths of the microstrip lines result in different change in the phase of the signal. Let us consider a microstrip line of the length l. The length can also be given in wavelengths as $l = r\lambda$. A constant phase point travels the physical distance l in the time

$$t_0 = \frac{l}{v_p} = \frac{r\lambda}{v_p}. \tag{14}$$

The propagating wave is sinusoidal and with 2π period and the periodic time of the wave is given by

$$T = \frac{1}{f} = \frac{\lambda}{v_p}. \tag{15}$$

Thus, the phase of the signal can be obtained by comparing the transmission time to the periodic time

$$\varphi = \frac{t_0}{T} \cdot 2\pi = \frac{l}{\lambda} \cdot 2\pi = r \cdot 2\pi. \tag{16}$$

As the wave has the period of 2π, the interest of the phase difference is usually expressed between $[0, 2\pi]$.

2.2.2 Coplanar Waveguides

The coplanar waveguide (CPW) is a planar transmission line structure on a dielectric substrate, where two ground planes are placed to both sides of the conducting stripline [20], [24]. The coplanar waveguide supports TEM-modes and the integration of the components in series and in parallel is very facile. Because of this, the coplanar waveguides are largely used in the millimeter-wave MMIC-circuits [20]. If a conducting ground plane is also attached to the reverse-side of the substrate, the structure is called conductor-backed coplanar waveguide (CBCPW) [24]. The conductor-backed coplanar waveguide is presented in Figure 4. As with the microstrip line, the substrate height h and the dielectric constant ε_r with the stripline width w and the thickness t determine the electric properties of the CBCPW. In addition, the ground plane distance from the stripline s is also of importance in designing the coplanar waveguide.

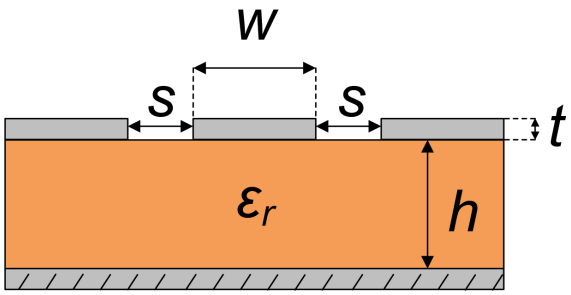

Figure 4: Conductor-backed coplanar waveguide structure.

The CBCPW can be quite problematic for the high frequency RF-structures. The ground planes above the substrate must be properly connected to the ground plane below to ensure that the undesirable waves are not excited. Thus, several vias must be implemented to connect the planes together. This makes the structure more complex to design and manufacture. To prevent this, a normal coplanar waveguide could be utilized, but if the available board is a multilayer PCB, the intermediate conducting layers can not be discarded and the CBCPW must be used.

In this thesis, there is only the need to integrate one microwave component in series on to the PCB. Thus, the coplanar waveguide is not a very suitable candidate

for the feeding network. The coplanar waveguide has similar qualities as the microstrip line considering the losses and the radiation but in a structure that focuses on the simplicity, the coplanar waveguide remains the second. Also, the matching to the coplanar waveguide is not as straightforward as with the microstrip line if the structure contains transitions between planar transmission lines and waveguides.

The CPW is an appropriate choice if the design requires multiple parallel components. The parallel components in a microstrip line structures require additional striplines and vias to the ground plane which makes the design more complex and lossy. In the coplanar waveguide, the stripline length for the parallel components can be minimized as the ground planes are next to the signal line. This also minimizes the losses and is one of the reasons why the coplanar waveguide is widely used in MMIC boards.

2.2.3 Rectangular Waveguide

The rectangular waveguide (RWG) is one of the earliest microwave transmission line structures [21]. It is a hollow structure with a conducting shell and the wave propagates inside the structure, which is filled with a material whose permittivity and permeability are ε and μ, respectively. As the name suggests, the rectangular waveguide has a rectangular profile. Generally a denotes the length of the long sidewall, the waveguide width, and b denotes the length of the short sidewall, the waveguide height. Figure 5 presents the outline of the rectangular waveguide.

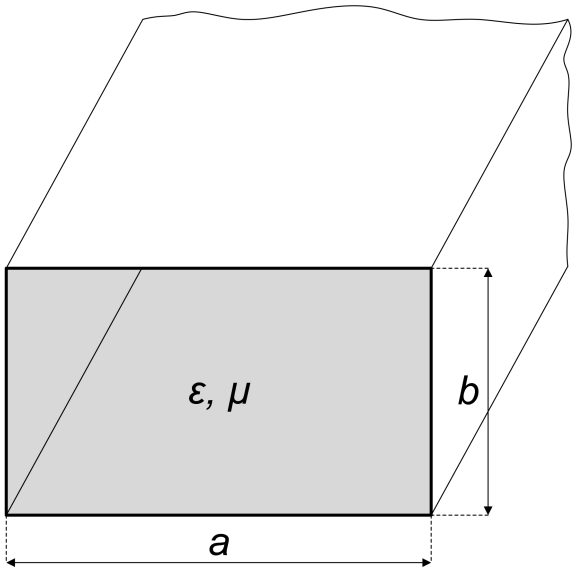

Figure 5: Rectangular waveguide structure.

The rectangular waveguide supports both TE and TM waves. The excited TE or TM mode can be determined by solving the Helmholtz equation for the longitudinal magnetic or longitudinal electric field respectively. The solutions for the equation are similar except the boundary conditions of the electric and magnetic field. These solutions are presented widely in the literature and the profound analysis can be found in [22].

The exciting modes in the RWG are determined by the cut-off frequencies related to the modes. The cut-off frequency is [22]

$$f_{c,mn} = \frac{1}{2\sqrt{\mu\varepsilon}}\sqrt{\left(\frac{m\pi}{a}\right)^2 + \left(\frac{n\pi}{b}\right)^2} \tag{17}$$

where m and n refer to the number of maximums in a transverse field distribution.

The TE_{10} is the lowest mode to excite in the rectangular waveguide and generally it is the mode used in the waveguide applications. Only one mode is typically used in the waveguides as the mixing between multiple wave modes inside the waveguide will cause losses. Otherwise, the energy would couple from the desired mode to undesired modes. The cut-off frequency for the TE_{10} is achieved from (17) when $m = 1$ and $n = 0$

$$f_{c,10} = \frac{1}{2a\sqrt{\mu\varepsilon}}. \tag{18}$$

Furthermore, the characteristic impedance for the TE_{10} mode is given by [20]

$$Z_{\mathrm{TE10}} = \frac{\eta}{\sqrt{1-(f_{c,10}/f)^2}} = \frac{\eta}{\sqrt{1-[\lambda/(2a)]^2}} \tag{19}$$

where $\eta = \sqrt{\mu/\varepsilon}$ is the intrinsic impedance of the material filling the waveguide. As can be seen from (18) and (19) the cut-off frequency and hence the wave impedance are not affected by the height of the RWG, b. However, the characteristic impedance of the waveguide is affected by the height. The characteristic impedance of the waveguide supporting the lowest order mode is given by [20]

$$Z_{0\mathrm{TE10}} = \frac{U^2}{P_p} = \frac{2b}{a} Z_{\mathrm{TE10}} \tag{20}$$

where U is the voltage that is obtained by integrating the electrical field over the cross section of the waveguide. P_p is the power flown through the guide obtained by integrating the cross product of the electric and magnetic field over the cross section of the waveguide.

If the width of the waveguide is kept constant (a is constant), the impedance of lowest propagating mode TE_{10} remains constant as seen from (19). Thus by changing the waveguide height, the waveguide impedance can be adjusted as shown in (20). For example by tapering the RWG in the direction of the height, the waveguide impedance can be reduced, which might be beneficial for the matching purposes as the impedances of the standard waveguides are generally several hundred ohms.

The lowest operation frequency of the waveguide is limited by the increase in the attenuation as the frequency approaches the cut-off frequency of the propagating mode. The highest operation frequency is limited by the excitation of the following mode, i.e. the cut-off frequency of the adjacent mode. For TE_{10} the adjacent mode is either TE_{01} or TE_{20} depending on the waveguide height [25].

The main attenuation of the RWG is determined by a lossy waveguide conductor and it can be found by calculating the power loss per unit length of the waveguide

[21]. The dielectric losses can also increase the attenuation if the waveguide is filled with a lossy dielectric material. However, commonly the waveguides are filled with air and the dielectric losses can be neglected. The attenuation constant as a result of conductor losses is given by [23]

$$\alpha_{c\mathrm{TE10}} = \frac{R_s}{\eta\sqrt{1-[\lambda/(2a)]^2}}\left(\frac{1}{b}+\frac{\lambda^2}{2a^3}\right). \tag{21}$$

Equation (21) gives a theoretical attenuation by the DC-conductivity and the attenuation in practice is 1.2-1.5 times larger (in decibels) [26]. The difference is mainly originated from the surface roughness of the waveguide and the increase in the operating frequency demands a smoother surface.

The advantages of the RWG are the fairly low losses even at the higher frequencies. The main disadvantages are the large size of the waveguides, which can not be changed without affecting the performance and the poor possibility to integrate microwave components in them.

Several standardized rectangular waveguides exist for the millimeter wave frequencies. Table 2 lists some of them with their sizes, cut-off frequencies, and operating frequencies. The WR-34 and WR-28 waveguides could be utilized for the cm-band and the WR-12 and WR-10 for the E-band. Even though separate rectangular waveguides with their own dimensions can be designed, the standardized waveguides should be kept in mind as the measurement equipment is based on them.

Table 2: Standardized waveguides for millimeter wave frequencies.

Abbreviation	a [mm]	b [mm]	f_c [GHz]	Operation frequency [GHz]
WR-34	8.64	4.32	17.4	22–33
WR-28	7.11	3.56	21.1	26.5–40
WR-12	3.10	1.55	48.4	60–90
WR-10	2.54	1.27	59.0	75–110

2.2.4 Substrate Integrated Waveguide

Substrate integrated waveguides (SIWs) are a fairly new addition to the transmission line family and they have been researched quite much in the past several years. One of the earliest proposals is presented in [27]. The SIW provides more compact solution than the traditional rectangular waveguides and less losses than the typical planar transmission lines. Furthermore, the SIW enables the utilization of the microwave components with waveguide to microstrip transitions, which are significantly more straightforward to realize than the transitions between the RWG and the microstrip line.

The solution presented by the SIW is that the rectangular waveguide is integrated into the microstrip substrate. This is possible due to the characteristics of the TE_{10}

mode. As presented in (18) and (19), the height b can be reduced without large impact to the propagation, and thus, a thin substrate can be used as a propagation medium. The waveguide width a is realized by using array of vias or metallized grooves as sidewalls of the rectangular waveguide. The vias are more typically utilized from these two possibilities. The ground plane and the metallization above the substrate provide the other metallic walls for the waveguide.

Important parameters in SIW design are obviously the SIW width, the properties of the substrate (height h, dielectric permittivity of the substrate material ε_r, loss tangent $\tan\delta$), the period length p, i.e. the length between two adjacent vias, and the via diameter d. The outline of the general SIW structure is presented in Figure 6. Simple design rules for choosing the proper parameter values are presented in [28]. The design is restricted so that the via diameter cannot be larger than the period length as it would be non-physical realization. Furthermore, the period length must be large enough as too dense via array will affect the mechanical rigidity of the structure. For practical reasons the number of vias is desired to be few but they must be apart from each other less than a quarter of the cutoff wavelength or else the bandgaps are formed into the waveguide. However, as the SIW is periodic structure without continuous walls, some of the EM field is leaked outside the waveguide. This clearly produce losses and the d and p must be chosen in such a way that the leakage loss does not become dominant.

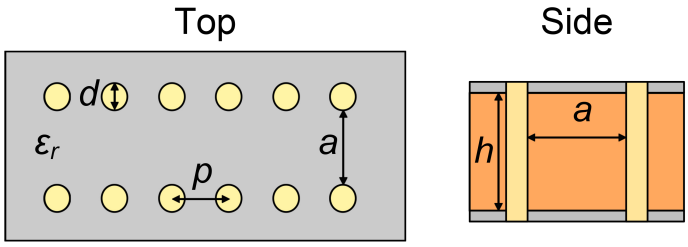

Figure 6: Outline of the substrate integrated waveguide.

In addition to the leakage loss, there are dielectric and conductor losses. In SIWs dielectric losses are typically dominant. These losses can be calculated by utilizing the conventional rectangular waveguide equations. This is because only the TE_{n0} modes can exist in the SIW structures and the SIW have similar dispersion characteristics as the rectangular waveguides have for these modes. However, the leakage losses are lesser known features and they have been researched quite widely to better understand the loss mechanism that is particularly related to the SIW. Sometimes the leakage losses are also called radiation losses due to their nature. Models and formulation for the leakage losses are comprehensively presented in [29] and [30], thus their further analysis is neglected in this thesis.

At the mm-wave frequencies the components and connectors are mainly for microstrip lines and rectangular waveguides. Furthermore the rectangular waveguides are typically more beneficial for the design of the high gain aperture antennas such as the horn antennas. Thus, to use the benefits of the other transmission line structures, the transitions between microstrip and SIW or rectangular waveguide and

SIW must be utilized. The microstrip to SIW transitions are typically quite simple as they are based on a single taper. Design equations for typical planar transition is presented in [31]. The RWG to SIW transitions are also normally based on tapering but they can be a more complex structure as demonstrated in [32].

The SIW components have been researched quite considerably. Especially the passive components for the higher frequencies like mm-wave range are considered as the planar structures tend to have high losses and the SIW components offer a good alternative. Also, the SIW-based antenna structures have raised interest. For example, a two-way and four-way power dividers for an antenna feed network are presented in [33]. These power dividers operate near the cm-band and the measured two-way power divider could be a suitable option for the feed network. Moreover, the substrate integrated waveguides can also contain phase shifting structures as presented in [34]. However, this kind of structure is not electrically controllable and provides only around 50° phase shift for the cm-band but these phase shift structures are still in early development stages. A more extensive review of the SIW circuits and antennas is presented in [35].

The substrate integrated waveguides provide very promising alternative for the traditional feeding networks, especially at the millimeter wave frequencies. They can outperform rectangular waveguides in size and planar transmission lines in losses thus enabling the design of low profile networks with high efficiency. However, the SIW structures are still fairly recent research area and they lack of commercial realizations at the time, especially when considering the components that have to be tailor made.

2.3 Phase Shifters

Phase shifters are commonly used in electrically steerable antenna applications to realize phased antenna arrays. The phase shifter is a key component to the beam-steerable antenna array and its properties heavily determine the overall performance of the phased array system.

The phase shifters are used to change the phase of the transmission signal. In principle, phase is the only parameter managed, and the amplitude of the signal should not change because the phase shifter. Furthermore, the power consumption in the antenna systems is desired to be low as the 5G networks aim to multiply the number of base stations. Thus, the insertion loss of the phase shifter is desired to be as low as possible. Another important characteristic of the phase shifter is the phase accuracy, which is desired to be high. The phase inaccuracy in phased arrays induces undesired grating lobes and increased overall sidelobe level. For many antenna applications the accurate control of the phase is thus extremely important. In addition, the switching time of phase shifters affects the operation. For example, in the modern mobile communication networks the latencies are to be minimized, which also means the beam-steering should be as fast as possible to achieve instantaneous connections. On the other hand, too long phase settling time can increase the insertion loss. From a practical point of view, the phase shifter size, the power handling, the bandwidth, and the cost influence the design and dictate what kind

of phase shifter should be chosen.

This section covers the general attributes of the microwave phase shifters. The phase shifters can be characterized in several ways, whether they are analog or digital, whether they are passive or active, what technologies they are based on, and how they operate. The discussed phase shifter technologies are semiconductor based monolithic microwave integrated circuits (MMIC), micro-electromechanical systems (MEMS), thin film ferroelectric devices, and thin film ferrites. In addition to these, several operation principles for the phase shifters exist and a few main categories are covered in the thesis. These are switched-line phase shifters (SLPS), loaded-line phase shifters (LLPS), slow-wave phase shifters, and reflection-type phase shifters (RTPS). The phase shifter characteristics are firstly discussed in a general level and, finally, a survey of the available E- and cm-band phase shifters is done.

2.3.1 Analog and Digital Phase Shifters

Phase shifters are generally designed to support maximum of 360° phase shift and they can be either analog or digital. Analog phase shifters provide continuous phase tuning whereas digital tuners can produce discrete phase delays. With the analog phase shifter the phase shift is continuously scaled according to the analog control signal variation. The voltage is most often used as the control signal in these phase shifters and the varactor diode is usually the controlled device to produce the phase shift [36]. However, analog phase shifters are vulnerable to the noise of the control signal and they typically produce harmonic distortion to the phase-shifted signal. Thus, the precise control of the phase shifters may prove to be quite a challenge. This might make the beam control of the multi-element antenna array even more complicated.

Practical phase shifters typically provide few discrete phase shifts, which enables antenna beam-steering with a sufficient accuracy and continuous phase shift is not required. Hence, in phased arrays digital phase shifters are commonly used. Digital phase shifters have discrete phase states and these states are expressed through the phase shifter bits. Bits themselves have two states, they either turn the phase shift on or off. These bits are generally divided so that the first bit adds 180° phase shift, the second 90° phase shift etc. The different states are formed additively from these phase bits and the amount of the bits determines the phase shifter resolution. These bits are controlled by the control signal, which is usually a voltage signal also with the digital phase shifter. The digital phase shifters do not suffer from the noise of the control signal and the performance between units is often more uniform than with the analog ones. Moreover, the digital phase shifters are easy to assemble and a wide range of commercial digital controllers exist without the necessity to design controlling systems from the scratch.

2.3.2 MMIC Phase Shifters

The MMIC phase shifters have advanced steadily during the past decades and there is a wide range of commercially available MMIC phase shifters. These are usually based on GaAs but also SiGe and InP based phase shifters are used. Advantages

of MMIC phase shifters over their ferrite-based counterparts include low power consumption and small size. MMIC phase shifters also support integration on a printed circuit board. General discussion of the MMIC phase shifters is presented in [37].

2.3.3 Switched-line Phase Shifters

The switched-line phase shifter is a true time delay device. This means that the phase response of the shifter is proportional to the frequency of the signal. Thus, the time delay is constant for all the frequencies through the bandwidth. For a phased array the true time delay is a desired feature as the antenna beam alignment is then independent of the frequency. If the phase shift is a constant, the beam will steer with the frequency and this will lead to a degraded scanning performance of the antenna. The beam squint angle is given by [37]

$$\Delta\theta = \arcsin[\sin(\theta)/(1 + \Delta f/f)] - \theta, \tag{22}$$

where $\Delta\theta$ is the beam squint, θ is the beam angle, f is the operation frequency and Δf is the frequency change. For example, for the 71–86 GHz band with the beam at 30° angle, the beam squint between the center frequency $f = 78.5$ GHz and the boundary frequency ($\Delta f = 7.5$ GHz) is $\Delta\theta = 2.845°$. This is relatively large variation and certainly degrades the phased array performance.

The switched-line phase shifter is somewhat intuitive solution to adjust the signal phase. As the physical length of the signal path changes, similarly the electrical length and thus, the phase of the signal varies. The basic SLPS is constructed from two, switchable transmission line paths as shown in Figure 7. One path is chosen as a reference line where the phase shift is set to be 0°. The other path is usually a longer one, which causes the signal to be time-delayed as compared to signal traveled through the reference path. The phase shift can be calculated from (16). Often the switched-line phase shifters are more suitable for large phase variations like 180° and 90° [37]. Nevertheless, it is possible to produce the SLPS with multiple paths or add several phase shifters in series to improve the phase shift or time delay resolution. Furthermore, sometimes switched-line phase shifters are used in combination with other types of phase shifters to achieve better resolution.

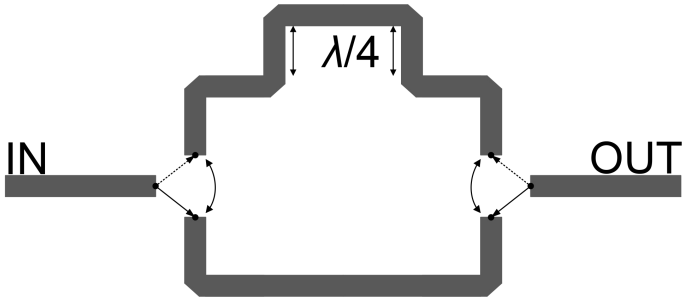

Figure 7: Switched-line phase shifter with a reference line branch below and the phase shifting branch above. The upper branch is $\lambda/2$ longer than the lower branch, providing 180° phase shift. The active branch is chosen with SPDT switches.

Single-pole double throw (SPDT) switches are used in binary SLPSs. SPDT switches can be realized for example with MOSFETs or PIN diodes to change between different branches [37]. The switch normally affects the most the phase shifter properties, such as insertion loss, harmonic distortion, power handling capability, and isolation. If the isolation is poor due to the parasitic capacitance, the leak to the off-path from the on-path is possible. This certainly degrades the phase shifter performance. The isolation is generally desired to be more than 20 dB. The MOSFETs are popular choice for the switches due to the monolithic integrability and low power consumption. However, the MOSFET switches have limited performance at millimeter wave frequencies and the trade-off has to be made between insertion loss and the isolation as presented in [38]. The insertion loss can be decreased by increasing the size of the FET as this decreases the channel resistance but at the same time it increases the gate-to-source capacitance and hence makes the isolation poorer. The capacitance can be adjusted with a shunt inductor but this limits the bandwidth and increases the MOSFET size.

The SLPS can provide a fairly low reflection and they are relatively easy to manufacture. The main disadvantages with the phase shifter are due to switches as discussed above, but also the transmission lines themselves can produce quite high insertion losses especially at the mm-wave frequencies. For example the switched-line phase shifter with FET switches presented in the [39] provides around 13 dB insertion loss over 33–35 GHz bandwidth. Furthermore, the size of the switched-line phase shifter is in the order of wavelengths making it physically large to provide substantial phase shift as discussed in [37].

2.3.4 Loaded-line Phase Shifters

The loaded-line phase shifters are typically narrow-band structures where the phase shift is attained by introducing a reactive element in parallel to the transmission line, i.e. adding a reactive load to the transmission line. As a single reactive element causes reflection, a second identical element is spaced to a $\lambda/4$ distance apart from the first one to cancel out the reflected wave. Due to this matching the loaded-line phase shifters are narrow-band and they are typically used for small phase shifts such as 22.5° or 45° [37], [38]. The phase shift is controlled by tuning the reactive elements, which can be either inductors or capacitors. However, capacitors are normally used, because tunable inductors hardly exist at the millimeter wave frequencies. The inductance tuning is usually realized with a fixed inductor and a tunable capacitor in series, which also narrows the band. The tunable capacitors are often varactors, tunable MEMS capacitors, or switchable capacitor banks. A microfluidic-based tuning solution offering relatively low insertion loss and broadband operation is presented in [40]. However, this technology is yet far from being applied in practice or from being commercialized.

The $\lambda/4$-line between the reactive components can be replaced with a reactive lumped element, and thus, the size of the phase shifter is decreased especially at the lower frequencies. The formed π-network is either of high- or low-pass type depending on the chosen element topology. Similar results can also be achieved

with corresponding T-networks. The possible topologies are presented in Figure 8. The low-pass topologies result in a relative phase advance, whereas the high-pass topologies result in a relative phase delay. The high-pass and low-pass networks are typically used together such that the phase shift is acquired by changing between the networks as with switched-line phase shifters.

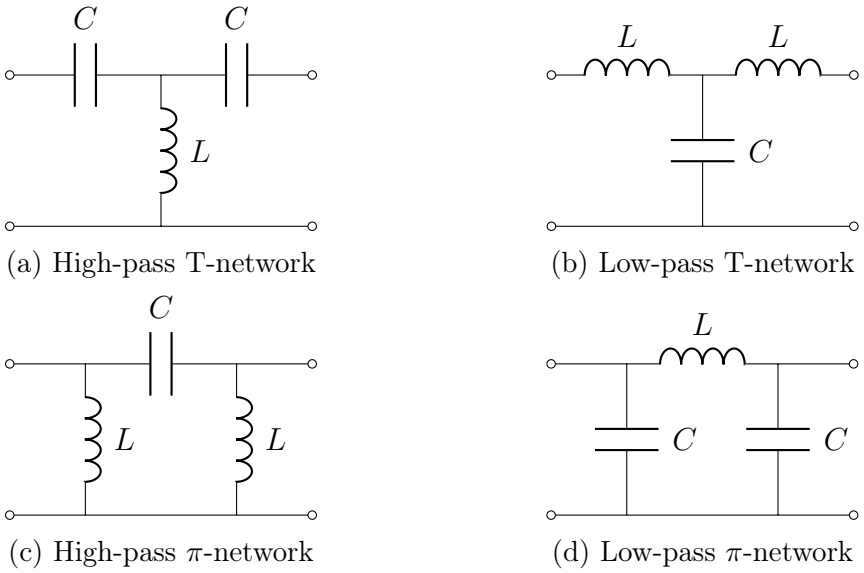

(a) High-pass T-network (b) Low-pass T-network

(c) High-pass π-network (d) Low-pass π-network

Figure 8: Different T (a, b) and π (c, d) filtering network topologies. All the components can be tuned. Tunable capacitors are more often used. Tunable inductors are typically realized with fixed inductors and tunable capacitors.

These phase shifters are called high-pass/low-pass phase shifters or switched-filter phase shifters, the distinction between the aforementioned phase shifter types being vaguely defined. The switched-filter phase shifters will be discussed more later on. However, the phase shift can also be achieved with a single T- or π-cell LLPS by tuning the lumped element values. As stated before, these kinds of single cell elements provide limited phase shift normally up to 90°. The evaluation of phase shift limitations for a low-pass π-network is presented in [41]. It is shown that the phase shift tuning range, but also the insertion loss increases with the tuning range of the varactors, even with ideal elements. Another example of a low-pass LLPS, which has tunable varactors and a transformer-based tunable inductor, is presented in [42]. The proposed system has a simulated phase shift of 48° with an average insertion loss of 3.5 dB at 60 GHz frequency. Although, it must be noted that to cover the whole 360° phase shift several of these phase shifters should be placed in series, which evidently increases the insertion loss to around 25 dB.

As with the switched-line phase shifters, the performance of the switched-filter phase shifters is heavily affected by the switches used to toggle between the order of the pass. PIN diodes and MOSFETs are again mostly used in MMIC realizations. With high-pass and low-pass branches a larger phase shift is achieved and the switched-filter phase shifters provide up to 180° phase shifts [37]. Furthermore the switched-filter phase shifters are relatively easy to manufacture as with the MMIC

technology any lumped element values are effectively possible. The design equations to find out lumped element values for high- and low-pass circuits are presented in [43]. The paper also introduces a 4-bit switched-line phase shifter with 25 dB insertion loss at the 70–85 GHz band.

To prevent the use of SPDT switches and subsequently decrease the insertion losses, the high-pass and low-pass networks can be used alone in filter-bypass circuits. In these circuits single-pole single-throw (SPST) switches are used to bypass the filtering high-pass or low-pass network that causes the phase delay or advance to the contrary of the bypass state. A switched high-pass bypass phase shifter is presented in [44] which demonstrates a 5-bit phase shifter only with 5 dB insertion loss at 19 GHz. Moreover a switched low-pass bypass phase shifter is presented in [45] which demonstrates a 4-bit phase shifter for 28–40 GHz band with an integrated low-noise amplifier. However, these solutions are not yet available at millimeter frequencies due to the limitations of MOSFET switches [38].

2.3.5 Slow-wave Phase Shifters

The slow-wave phase shifters are also known as periodically-loaded transmission line phase shifters, distributed transmission line phase shifters, and synthetic line phase shifters. General description of them is presented in [37] and [46]. They are in principle true time delay phase shifters such as the switched-line phase shifters. As the SLPSs tend to be physically large, the slow-wave phase shifters can be made smaller by periodically loading the transmission line with shunt capacitances. The whole length of the transmission line is periodically loaded, thus increasing the capacitance per unit length of the line. This increases the effective dielectric constant and the characteristic impedance of the line. Furthermore as can be seen in (13), this decreases the phase velocity of the propagating wave, hence the name slow-wave. The decreased phase velocity corresponds to the increased electrical length of the transmission line, and thus, the line can be physically shortened. A circuit model of the slow-wave phase shifter is presented in Figure 9. The transmission line is modeled as an LC circuit and C' is the variable capacitance used to load the transmission line.

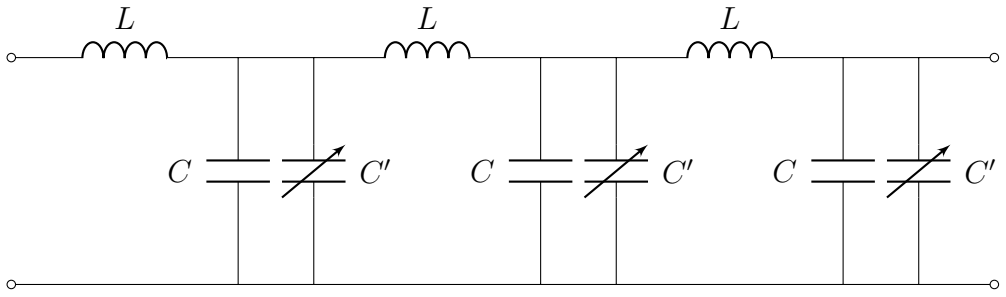

Figure 9: Circuit presentation of the slow-wave phase shifter. C and L represent the transmission line impedance and C' is a variable shunt capacitance used to load the transmission line.

MMIC-based varactors are usable at lower frequencies, where they are often used as shunt capacitances. At the higher frequencies, their performance is often inadequate. A MEMS-based distributed line phase shifter for the 75–110 GHz, i.e. W-band is described in [47]. The used transmission line is a coplanar waveguide and it is fabricated on a glass substrate. Variable MEMS capacitors/switches are used to load the coplanar waveguide. By controlling several capacitors at the same time, the coplanar waveguide is distributed to 3 different parts. Each part provides a different phase shift, and thus, 3 bits are formed. The wanted phase shift is acquired by controlling the MEMS switches of the each part accordingly. As the MEMS switches are very low-lossy, the average insertion loss across the whole W-band is between 2–5 dB which is very low for this high frequencies. The low losses are also due to the decreased length of the transmission line, which could otherwise cause significant dissipation. However, problems might arise from the use of the glass substrate in practice, and also from the amount of MEMS switches needed to have even the smallest phase shift and their reliability.

The distributed line phase shifter can also be slightly different as presented in [48]. The variable capacitances can be implemented as MOSFET switches distributed along the transmission line. The gate capacitance of the common source MOSFET is connected to the transmission line and the slow-wave line is formed. The MOSFET switches are connected to the signal output and by switching the FETs on one at a time, the signal travels different lengths in the slow-wave line, and thus, a wanted phase shift is acquired. The idea is basically the same as used in switched-line phase shifters, here the one varied transmission line is the slow-wave line. The main problem with this structure is that the impedance of the MOSFET switches changes drastically during on and off, which leads to an amplitude and phase errors according to [38]. Furthermore, the power loss and increase in noise are inevitable as not all the input power is lead to the output through the switches.

2.3.6 Reflection-Type Phase Shifters

The phase shifters proposed earlier are of transmission type, meaning the signal phase is varied during the transmission. The reflection-type phase shifter (RTPS) is based on a quadrature coupler and identical reflective loads, i.e. reactive loads. The general schematic of the RTPS is presented in Figure 10. The coupler is a 4-port 90° hybrid and the port 1 is the RF-input port and the port 4 is the RF-output. Ports 2 and 3 are terminated with identical, mismatched loads. The coupler divides the input signal to the ports 2 and 3 such that the signal in port 3 is delayed by 90 ° as compared to the signal in port 2. The two signals reflect from the identical mismatched terminations, interfere destructively in port 1 and constructively in port 4. In other words the input port impedance is always matched and by adjusting the mismatching in ports 2 and 3 the wanted phase variation is achieved at the output port.

The phase can be adjusted by varying the impedance of the reflective loads for instance by using varactors. The inspection of the different type of MMIC reactive loads, such as capacitive load and resonant load, is presented in [49]. The paper

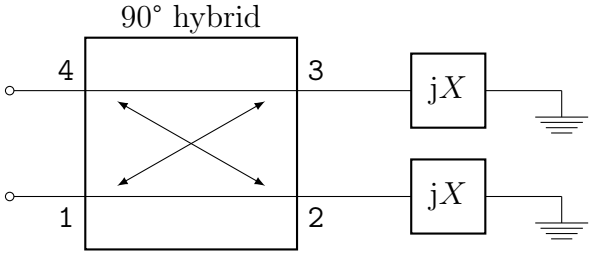

Figure 10: Reflection-type phase shifter can be realized with a 90 ° hybrid, whose two ports are terminated with identical, mismatched loads. The signal is fed to the input port 1 and after the reflection, the shifted signal is then formed at the output port 4.

suggests a dual resonant load (DRL) to be used as a reflective load. The dual resonant load consists of two resonant loads with different resonance frequencies in parallel. The major benefit of the DRL is that it has wider tuning range than the single resonant or capacitive loads. Thus the proposed load can be utilized to achieve full 360° phase shift within a single phase shifter structure. Nevertheless, the design of the DRL and its transformation network might be demanding. If simpler loads are to be used, the wanted control range can also be achieved by stacking several structures in series similarly as with the previous type phase shifters.

Diode and FET switches are also used in the reflective loads, especially for the digital control. The reflective load is a transmission line and its length and thus, its reactance can be varied with switches that are placed along the line. Switches are placed either in parallel or in series which evidently places some restrictions to the load design. Further analysis of the structure can be found in [36]. A schottky diode based load is adopted for a 4-bit E-band phase shifter in [50]. The full 360° phase shift is acquired and the measured insertion loss for 71–75 GHz is 7 dB. However, the phase shifter requires quite large space of 2.05 x 1.05 mm^2 as compared to other E-band phase shifters. A similar but more compact MMIC design is presented in [51] for 94 GHz with insertion loss as well around 7 dB.

The quadrature coupler can be for example a branch-line coupler with lumped elements as in [49], but quite often Lange couplers are used as they provide relatively wide band and occupy a small amount of space [36]. Couplers can also be cascaded so that they help to achieve the larger phase shift. In [52] three Lange couplers are used so that the first coupler is used as a power divider to the two adjacent couplers with the reflective loads. The output of these couplers is finally combined in a Wilkinson power combiner. At the 27–32 GHz band the phase shifter has a low insertion loss of 5 dB and a quite small chip size of 2 x 1.2 mm^2.

The reflection-type phase shifter has in theory low losses as if the loads would be fully reactive there would be no power loss from them. In practice, this is evidently impossible and the loads increase the insertion loss as discussed in [38]. Also, the coupler can have high insertion loss especially at millimeter wave frequencies and it occupies a large space. In addition, it is difficult to realize identical reflective loads. Differences between the two loads result in reflection losses, phase shift errors, and the performance can vary significantly between the different states.

2.3.7 MEMS-based Phase Shifters

Micro-electromechanical systems (MEMS) switches have been widely studied to replace traditional PIN diodes or FET switches. All the previously presented phase shifter types can also be realized with MEMS. The MEMS switch is usually composed of a flexible metallic membrane bridge over a metallic contact beneath it. The parts are normally several microns apart and a DC voltage is applied to connect the flexible bridge to the lower contact. The typical actuation voltage is around 20–100 V [37]. The switching is nearly free of losses as the control voltage is used to attract the parts to each other and it is not depleted in the switch.

The MEMS have an advantage of not being affected by the substrate they are manufactured on. Thus, they can be implemented on materials that are used in the standard IC processes and very close to the antennas that are ceramic, quartz, or PTFE-based. Also, while the FETs and other nonlinear switches have restricted capabilities at the higher millimeter frequencies, the MEMS do not have the same limitations. They often have wider operation bandwidth and significantly lower losses. For instance, for the E-band the reported losses using MEMS are typically 2–3 dB where the FET losses are around 9–10 dB. Additionally, MEMS switches have very low costs. Their performance in phase shifters and phased arrays is more thoroughly reviewed in [36] and [53].

However, the commercial MEMS phase shifters are still quite few and the MEMS are generally thought as unreliable solution especially for long-term applications [37]. The switch must endure billions of cycles and it is also quite vulnerable to the ambient interference. Thus, the packing of the MEMS is more critical than with alternative solutions. Furthermore, even though the manufacturing of MEMS switches themselves is inexpensive, the packaging of the MEMS can increase the costs significantly. Another problem for MEMS switches is that because they are mechanical switches the switching time is relatively slow, typically 1–30 µs as compared to the few nanoseconds that MMIC switches have [36]. This directly limits the scanning rate of a phased array to a level that is not favorable in 5G communications.

2.3.8 Ferroelectric Phase Shifters

The permittivity of ferroelectric material can be modified by applying a DC electric field to the material. This changes the crystalline structure of the ferroelectric material, which causes the permittivity variation and the dielectric constant to change [37]. As can be seen from (12), the propagation constant and thus, the phase is affected by the permittivity variation. The idea of using ferroelectric materials in phase shifters is quite old but the modern development in the manufacturing processes have increased their research in recent years [37].

The typically used ferroelectric material is $Ba_xSr_{1-x}TiO_3$ (BST) where $x = 0.6$ at the room temperature. The fabrication of the proper BST layer is typically the most challenging part of the phase shifter manufacturing. The proper crystalline structure of the BST is crucial to the performance. Thus, the thin film approach is superior when considering the operation, but the thick film deposition is more straightforward and cheaper. One proposal of the thick film BST phase shifter

is presented in [54]. However, the results show very poor performance at higher frequencies with relatively high biasing voltage of 90 V.

A clear and well-defined theoretical model of a thin film phase shifter is presented in [55]. The model is found to match well with simulation and experimental results. The modelled phase shifter is a coupled-line structure where the BST layer is located under the conducting lines. The ordinary thickness for thin film BST layers is around 0.5 µm but the results presented in [55] indicate that the thicker layer, such as 1–2 µm, could result in a better performance. However, it is challenging for the current manufacturing technologies to maintain the required manufacturing precision to produce so thick layers. Other structure is proposed in [56] where the ferroelectric material is used as a part of multilayer approach. The results indicate very low losses especially at the frequencies below 10 GHz. Nonetheless, this proposal is yet to be realized in practice.

The ferroelectric materials can also be used as tunable capacitors and thus, as a part of the previously presented phase shifter types. A digital implementation is also possible and a digital reflection-type phase shifter is presented in [57]. Nevertheless, the performance of the presented phase shifter leaves still much to hope for. The typical control of the ferroelectric phase shifter is analog. A very promising ferroelectric phase shifter is presented for a 20–40 GHz band in [58]. It resembles the loaded-line phase shifter with a low-pass π-network, where the tunable capacitors are ferroelectric varactors. The design is quite compact and the insertion loss is from 2 to 8 dB, though it varies quite much, which is a non-wanted feature. The full 360° phase shift range is achieved with 60-V biasing voltage, which is relatively low for a ferroelectric phase shifter, but the phase shift varies over the band greatly. Although the design is quite promising, the overall performance of the phase shifter must be improved to be more stable over the frequency band.

The ferroelectric phase shifters are potentially low-loss, low-cost, and compact devices but all of these characteristics are yet to be realised in the same phase shifter as noted in [37]. Their performance is not at a suitable level considering the phase shifting range or the biasing voltages often exceeds high levels such as 100 V to achieve convenient range. The ferroelectric phase shifters need more research and are still relatively far from being commercialized.

2.3.9 Ferrite-based Phase Shifters

The ferrite-based phase shifters are discussed in [21] and [37]. They are one of the earliest type of phase shifters used and were commonly used in the early phased array systems. The ferrite-based phase shifters are still dominant in military applications and in high power applications such as radars. While the MMIC, MEMS and ferroelectric phase shifters are mainly planar structures, the ferrite phase shifters can also be used in waveguide structures. The ferrite is a magnetic material that can be magnetized with a bias field. This magnetization changes the permeability of the material. If the ferrite is applied in the vicinity of a transmission line, the propagation constant is affected as can be seen from (12) thus leading to a phase shift.

The ferrite can be used as a continuous phase shifter for example by inserting a ferrite toroid inside a rectangular waveguide and biasing it with a signal line passing through the center of the toroid. By varying the bias current an analog phase shift is achieved. However, a more practical way is to use ferrite digitally by a saturation technique called magnetic hysteresis. When a bias field is applied to the ferrite and removed, the ferrite will not return to its initial demagnetized state but will remain magnetized with a certain magnetic moment. If a new bias field to the opposite direction is applied and again removed, the magnetization will change and the magnetic moment is transformed to the opposite direction. The bias fields should be large enough for the ferrite magnetization to achieve these two states, which are called the saturation magnetization denoted as $\pm M_s$. The single ferrite can only have these two states and the phase shift is determined by the length of the ferrite. In practice several individual toroids are needed to achieve the full 360° phase shift range. Furthermore, the saturation technique allows the biasing to be done with pulses rather than applying a continuous bias current to the system and thus, reduces power consumption. Apart from the saturation technique, the other type of ferrite phase shifters are Faraday rotation phase shifter and Reggia-Spencer phase shifter. Further description of them can be found in [21] and [37].

In conclusion, the ferrite phase shifters have high qualities in their power handling and they have ultra-low losses even at the higher millimeter frequencies. However, they are also regarded very expensive, they can have quite large structures, and they have very high power consumption even with the pulse control. Additionally, the pulse controlling also limits the switching rate between different states to 10–100 µs which makes the ferrite phase shifter relatively slow.

2.3.10 Active Phase Shifters

The majority of the phase shifters used are passive. As the insertion losses are usually the main problem for the phase shifters, the amplification of the transmission signal seems a viable option to increase the phase shifter performance. The active phase shifters discussed in [46] are based on that. They generally exhibit gain and can have smaller chip size and full 360° phase shift in one stage compared to their passive counterparts. The active phase shifters are typically based on vector modulators at mm-wave frequencies.

The active phase shifters based on vector modulators were first reported in the 80s'. One of the first viable suggestions is presented in [59]. The vector modulator is realized by four dual-gate MESFETs, which are used as variable gain amplifiers (VGA), each of them having their own branch. The signal is divided between the amplifiers by 180° and 90° hybrids so that the branch signals are opposite. By varying the gate bias voltage of the FETs, the signal amplitude of each branch is changed. The overall phase shift is obtained by the vector sum of these four orthogonal or opposite signals. Furthermore, the design allows that a signal with any phase and amplitude can be generated so that the phase shifter can be used as a vector generator. However, the amplifiers are typically biased so that they are either on or off. Thus, in a sense the four dual-gate FETs serve as amplifier-switches that are used to control the amplitudes of the branch vectors.

Nevertheless, this kind of design is not reciprocal and requires different transmission and receiver branches in antenna structure. The active phase shifters have not been very popular for their use of multiple switches when compared to their reciprocal passive counterparts. Yet, the improvement of the FET technologies have increased their research in recent years and for example an active phase shifter using vector sum method is presented in [60]. The paper also describes distinctly the needed passive components for a vector modulator phase shifters in general, which are power dividers and combiners and hybrid couplers.

In the previously presented passive phase shifter structures the FETs are used in passive states as switches. However, if they were to be used in active state, they can provide amplification to the phase shifter circuit. These kinds of phase shifters are usually continuous phase shifters with limited phase shift capabilities. Their performance is also often limited to the lower frequencies due to the FET performance deterioration at the higher microwave frequencies. Some of these phase shifters based on resonant circuits are presented in [61]–[63]. One of these [63] demonstrates phase shift at millimeter waves, but it has a tuning range of only 90° and the insertion loss is still 7 dB. In addition, the phase shifter consumes an outrageously large chip area of 125 mm^2.

A quite promising vector modulator-type phase shifter for 15–35 GHz band is presented in [64]. This wideband phase shifter has relatively small size of 0.19 mm^2 with maximum RMS gain error of 2.2 dB. The phase shift range is full 360° with 22.5° resolution. However, the gain decreases with the increase of the frequency and is −7 dB around 30 GHz. Furthermore, the phase shifter noise is not presented in the paper.

Four vector modulator phase shifters for E-band are presented in [65] and [66]. They are all 4-bit digital phase shifters with full phase variation range. The former article [65] presents two similar phase shifters, where the second one has a more compact area at the cost of the lower gain. The average gain of the first phase shifter is around 2.3 dB and 0.83 dB for the second one. Both phase shifters consume relatively low power of 21.6 mW and their average noise figure is above 10 dB. The phase shifters presented in [66] are divided to the transmitter and receiver branch phase shifters. The transmitter phase shifter operates at 80–94 GHz band and the receiver phase shifter at 70–77 GHz band. The 80–94 GHz phase shifter has a large gain deviation through the bandwidth from −4 dB close to maximum of 3.8 dB. Additionally, the 70–77 GHz phase shifter has the maximum gain of 17 dB with only 2 dB peak-to-peak variation and the phase error is less than 8°. Nonetheless, a closer inspection of the noise figures is neglected in the paper.

The active phase shifters have many benefits, such as signal amplification and small size. However, as stated before, their greatest weakness is they are unidirectional and their activity arises many problems. These problems are reported in [46]. The active devices consume power, which turns to heat and often requires special cooling in the antenna system. Furthermore, they add excess noise and nonlinearity to the RF-system chain that must be taken into account. Additionally, the matching network design can be very challenging for the active phase shifters. All in all, they are quite complex structures that can make the design demanding.

2.3.11 Cm-band and E-band Phase Shifters

Even though several types of phase shifters based on different fabrication technologies are presented in the literature, the commercial phase shifters for cm-band and E-band are almost non-existing. In fact, no suitable E-band phase shifter were found considering the design requirements. In practice, the use of commercial phase shifters is preferable as it simplifies and reduces the time taken by the phased array design substantially, and the price of the individual phase shifter can be decreased. Also, the commercial phase shifters can be considered more reliable and they tend to have similar performance between different batches.

The availability of the cm-wave phase shifters is better, although many of them are packaged with SMA-connectors. As the coaxial transmission is not considered, these phase shifters are not suitable for the system. Finally, the only suitable phase shifter with no package connectors and with possibility to planar mounting is found to be TGP2100 from TriQuint. As for the E-band, it is decided to utilize several microstrip line structures, which have known phase shifts against each other. Thus, the proof of concept can be achieved, but if the system is to be realized in practice, the phase shifters should be easy to integrate and reliable and therefore, produced by a special manufacturer.

2.4 Simulation Tools

The structures in this thesis are simulated using 3D EM-simulation software CST Microwave Studios [67]. The simulations are done in the transient solver of CST which is based on FDTD. This allows wide-spectrum simulations in relatively short time. However, the mesh grid in the simulations must be dense enough to correctly model the fine elements like microstrips or bondwires, which on the other hand increases the simulation time.

The simulation results are highly affected by the excitation and whether it is made properly. In CST there are two different excitation ports for S-parameter computation: the discrete and the waveguide ports. The following explains how both of these ports are used in this thesis.

The waveguide ports are used to calculate the eigenmode solution of the electromagnetic field for the specified area along with the line impedance. Thus, the S-parameter calculations are expected to be accurate. In the thesis the most common use for the ports is to excite the waveguides where the electromagnetic fields are limited to the lowest mode. The waveguide ports are also used to excite microstrip lines or coplanar waveguides, but then a port must be defined so that the correct mode is calculated for the line. The rule of thumb is to make waveguide port five times wider than the microstrip width and five times higher than the substrate thickness.

The discrete ports are used in S-parameter mode, meaning they are modeled as lumped elements consisting of a 50 Ω impedance placed parallel to the current source. The inner impedance is thus used to excite and absorb power; the current source is used only if the port is stimulated in the solver. The discrete ports are

placed between the microstrip line and the ground plane and their main use is to serve as the connection points to the S-parameter model of the cm-band phase shifter. As the phase shifter is a two-port device, two discrete ports are required to connect the phase shifter S-parameter model to the simulated structure.

3 Transitions between Waveguides and PCB

As presented in Section 1, the feeding network and the horn antenna are based on the rectangular waveguide. The phase shifters are mounted to a multilayer printed circuit board, thus the transitions are required from the waveguide to the PCB and from the PCB to the antenna. For the sake of simplicity, the microstrip line is chosen to be used as a transmission line structure on PCB over the other planar structures. The main goal is to design the transitions as lossless as possible so that the transmitted power is at maximum. The transitions have first been studied and designed for E-band structure and based on that the design for cm-band structure transitions is done. This chapter presents the transitions used in the final design. First, the transition design and the design guidelines in general are considered. After that, a more thorough survey for both frequency ranges is done separately. Finally, some concluding remarks on how to improve the transitions further are given.

3.1 Transition Design

The transition outlines from the side are presented in Figure 11. Basically, there are two transitions in one element branch. The inbound signal is fed through the RWG and coupled to a microstrip probe that continues as the microstrip line on the PCB. The phase variation is done on the PCB by the corresponding phase shifter, and thereafter, the signal is transferred to the horn antenna by coupling the microstrip line to the RWG feed of the antenna. The rectangular waveguides of the feeding network and the antenna feed are identical considering the waveguide height and width and materials. Obviously, both waveguides are also shorted from the other end where the signal should not propagate. Essentially, both transitions and their operation principles are very similar. However, in the waveguide-to-PCB transition, the microstrip line is towards the shorted end of the waveguide, and in the PCB-to-antenna transition, the microstrip line is towards the open end of the waveguide. Subsequently, the whole electric field must propagate through the substrate in the first transition from the feeding network to the PCB which is not necessary in the second transition where the main part of the field can couple straight to the antenna output. Thus, the transitions have a different parameter values when their performance is optimized.

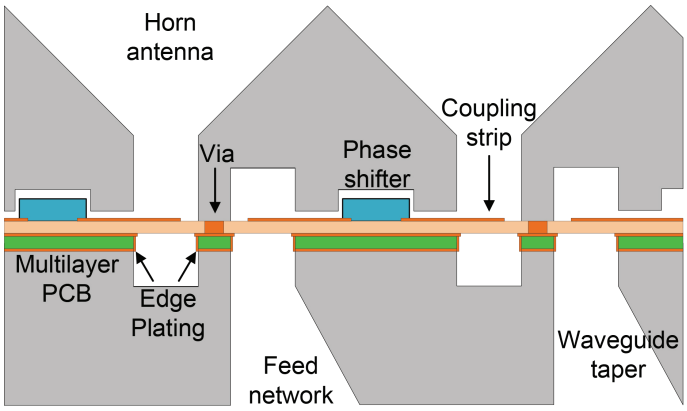

Figure 11: Side view of the transition structure.

The available space for the phase shifters is determined by the element spacing i.e. the horn antenna aperture size. The height of both waveguides are tapered around the PCB to have more space for the phase shifter. For similar reasons the adjacent waveguides share their boundary walls with each other. These issues are discussed more later on.

The entire phased array structure is assembled from three parts: the feeding network, the PCB, and the antenna. Of these the feeding network and antenna parts are manufactured by milling the wanted structures to the metal blocks made from the brass for example. The two blocks are separated by the PCB which is attached between them. As can be seen from Figure 11, this also separates the shorted ends of the waveguides to the their counterpart block. The waveguide of the feeding network has the shorted end divided from the rest of the structure to the antenna part above the PCB. Similar case is with the horn antenna where the shorted end is left on the feeding network part below the PCB.

The top cutaway part of the transition is presented in Figure 12. To ensure that the separated waveguide sections are properly connected to each other, several blind vias are required through the PCB substrate where the waveguides of the antenna part are to be positioned and connected to the PCB. Again, to save space and to minimize the complexity of the manufacturing, the adjacent waveguides share their vias with each other. Furthermore, the vias are plated with metal on the top layer of the PCB. This is to guarantee the connection to the waveguides of the antenna part.

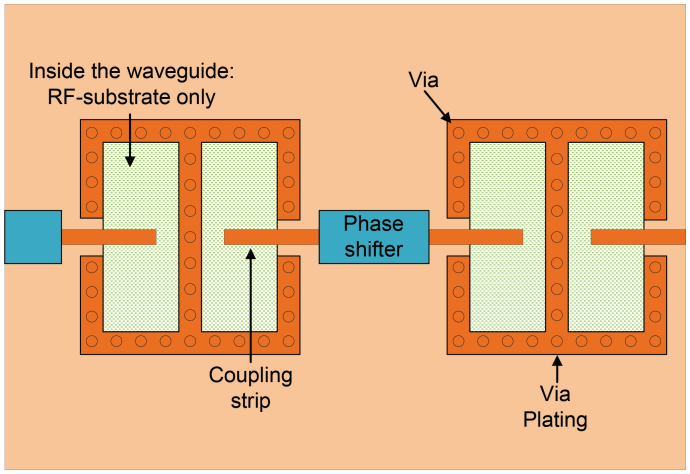

Figure 12: Top view of the transition structure.

To further improve the transition, the part of the PCB that is left inside the waveguide is cut away except the RF-substrate. Thus, a cavity is formed underneath the PCB. Moreover, the cavity is plated with metal as it is more cost-effective and easier to fabricate than the blind vias through the every layer of the PCB. Except the cavity, the rest of the lowest layer of the PCB is metallised so the waveguides of feeding network part are properly connected to it. With the metal-plated cavities and the vias in the substrate the waveguide structures can remain continuous and in galvanic connection through the whole structure. Furthermore, this ensures the

electromagnetic field is contained within the wanted array element and not leaked to the adjacent branches through the PCB. The PCB design and the waveguide design are discussed more thoroughly in the following sections.

The design process utilized in this thesis is the following. Firstly, the simulation model of the waveguide and the microstrip line is built. Then, with the simulation model, a parameter study is conducted to find out which parameters affect the transition the most. Lastly, some of the the parameter values are chosen according to the manufacturing restraints or other design reasons and the remaining free parameters are optimized so that the transition meets the requirements. The transition parameters are discussed more in Section 3.1.4.

Nevertheless, the transitions are not measured in this thesis. They are integral part of the structure and to properly measure both transitions separately, an independent test structures should have been made to fully characterize their performance. However, this is not sensible due to manufacturing time consumption and the design complexity of such measurable test structures. Extensive simulation results are presented for both transitions and the overall performance of them can be evaluated from the phased array measurements.

3.1.1 Literature Survey on Transitions

Several waveguide-to-microstrip transitions are presented in the literature. They can be divided to the following:

- Transition is along the propagation direction of the waveguide.
- Transition couples energy via apertures that are cut in the waveguide.
- Transition is transverse to the propagation direction of the waveguide.

Of these, the transition along the propagation direction is one of the earliest proposals [68].

The transition along the propagation direction of the waveguide often uses ridged waveguide impedance transformers to match the waveguide to the microstrip line. One example of the ridged waveguide impedance transformer utilization is presented in [69] for the 17–22 GHz bandwidth. However, the ridged waveguide structure can be difficult to manufacture precisely at the E-band and even at the cm-band. That is the main reason why the transverse transition utilizing microstrip probes has proven to be very popular at the millimeter-wave frequencies. Furthermore, the transitions along the propagation direction of the waveguide would increase the overall height of the antenna structure and the wanted low-profile design could not be achieved.

The transverse transitions generally have microstrip probes entering the waveguides through a small aperture in the broad sidewall of the waveguide. It is also notable that compared to the transition design presented in this thesis, the transverse transitions presented in the literature do not normally have the substrate filling the whole cross-sectional area of the rectangular waveguides. Rather, they are restricted close to the probe leaving the majority of the waveguide empty.

One of the earliest proposals using the larger microstrip probe patch is presented in [70]. The probe patch is inserted inside the waveguide and its impedance is

matched to the 50 Ω microstrip line with a quarter-wave impedance transformer. The paper presents four different designs so that the frequency band from 26 GHz to 110 GHz is covered. The measured results show that the insertion loss near the cm-band for a single transition is about 0.06 dB when not taking into account the waveguide losses or the microstrip losses. The return loss is more than 21 dB. The insertion loss is approximately 0.2 dB and the return loss is better than 15 dB for the single E-band transition.

However, another configuration for the probe orientation can also be used. The probe configuration presented in [70] and in this thesis have the the probe and the surface of the substrate facing the direction of the propagation. In the alternative configuration the microstrip also enters the waveguide through the same sidewall as in the previously mentioned cases but now the microstrip line is translated 90° along its axis so that the probe and the substrate align along the direction of the propagation. This longitudinally mounted patch is referred commonly to as an E-plane probe. The clear explanation of both configurations and the experimental results for the E-plane probes with different dielectric substrates for the 85–120 GHz band are presented in [71]. Another quite thorough and analytical transition analysis of the E-plane probe for the 26.5–40 GHz band is conducted in [72].

The E-plane probe has been quite popular in millimeter wave applications as it is quite wideband. Generally, the E-plane probe has limited substrate width, length, and thickness. These are required so that the unwanted TE or TM modes are not excited in the probe and the following microstrip line. The transition presented in [73] describes a method enabling a large substrate size compared to conventional E-plane probes. The experimental results from 66 GHz to 98 GHz show that the transition insertion loss is varying between 0.25 dB and 0.42 dB. Although microstrip lines are commonly used as E-plane probes, other possibilities exist. Another transition covering the frequency band from 75 GHz to 110 GHz is presented in [74] and the E-plane probe is constructed from the suspended stripline. The benefit of this design is that no matching network is required for the probe. However, another transition between the suspended line and the microstrip line is demanded which on the other hand complicates the design.

Majority of the transitions presented in the literature utilize PTFE-based substrates, which have small dielectric constant. PTFE-based RT/duroid 5880 with $\varepsilon_r = 2.2$ is commonly used. Furthermore, the transitions are commonly assembled using standard waveguides like WR-10 and WR-12 for the E-band and WR-34 and WR-28 for the cm-band. The waveguide dimensions are not normally varied from the standard dimensions. However, the paper [75] presents a transition structure using the E-plane probe in the WR-28 waveguide with reduced height. The simulated insertion loss is less than 0.15 dB and the return loss is above 20 dB from 26.5 GHz to 37 GHz. Nonetheless, no further examination of the effect caused by the reduced height to the transition is conducted.

To summarize, the E-plane probe is quite attractive solution for the waveguide-to-PCB transition but the main problem with the utilization of the E-plane probes in the planar array is that the each row of the array would require their own separate PCB. Thus, the complexity of the design proposed in this thesis would increase

substantially and the assembly of the structure could be very difficult. The design goal for the transition structure presented in this thesis is to be relatively simple as it is to be repeated multiple times in the final solution. Therefore, a single PCB board for which the probes are designed is the most appealing solution.

3.1.2 PCB Design for Transitions

The PCB structures can be divided to single-layer, double-layer, and multilayer structures. The layers refer to the quantity of the conducting layers in the circuit board structure. The substrate films in the structures are referred to as cores. A single-layer PCB has the conducting layer on the other side of the substrate and in the double-layer PCB the substrate is stacked between two conducting layers as presented in the microstrip line Section 2.2.1. The multilayer PCB has additional inner conducting layers in addition to the outer layers.

The phase shifters in the phased array design are to be controlled electrically. The control is generally realized by DC control lines that are embedded in the PCB. For such purpose, a multilayer PCB is required as the control lines can not be inside or on the substrate layer as it would affect the RF-performance. Electrically controlled phase shifters also require biasing voltages and separate control lines for each phase variation bit. For a single, 5-bit, digitally controlled phase shifter this suggests that 6 different lines are required, resulting to 96 control lines for the 4 by 4 array. It is not feasible to integrate so many lines on a single layer, especially when parts of the PCB are allocated to the waveguides, and thus, control line routing is not permitted in those sections. Hence, multiple control line layers are required. The general concept of the multilayer PCB outline is presented in Figure 13.

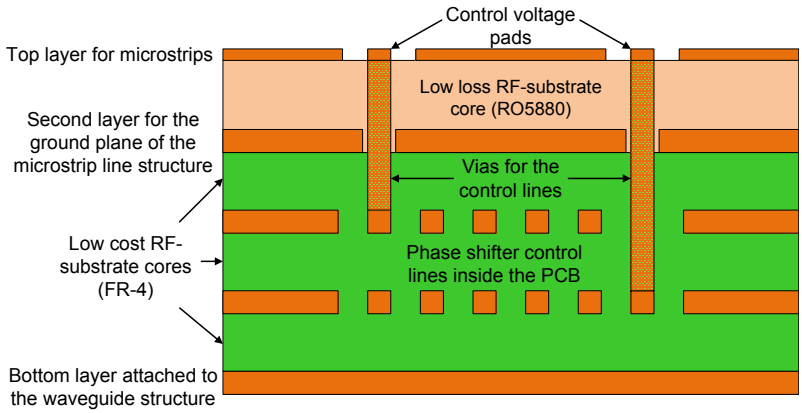

Figure 13: Side view of the multilayer PCB structure.

The top layer is the conducting metallic layer where the RF-signal is transmitted. It is on top of the substrate film and a ground layer, the whole structure fundamentally representing a double-layer PCB. The substrate material should have low losses at mm-wave frequencies. However, they are typically relatively expensive, and the available substrate cores are typically very thin, around few hundreds µm. Hence, to make the PCB structure more rigid a low-cost RF-substrate film (such as FR-4)

is often attached below the ground plane. Due to the manufacturing purposes, the substrates are normally available as the single layer boards. Essentially, these boards are stacked together with other single layer PCBs to form a multilayer structure. The conducting layers that remain between the substrates can be utilized for the control lines but the outermost conducting layer should be left without any control routes as it is used to properly connect the PCB to the feeding network structure.

The simplest transmission structure to design and manufacture on PCB is a microstrip line structure and it is used in the final design. Also, the coplanar waveguide structure is regarded as a possible solution but the transition to the single microstrip line is more straightforward to design and the attachment of the chosen phase shifters is less problematic. With different phase shifter structures the CPW might be more convenient. However, with CPW the multilayer PCB structure would require several vias between the inner metallic layers and the ground planes of the CPW to ensure that the parasitic capacitance do not affect the RF-performance of the transmission line. This would further complicate the design and manufacturing.

As discussed in the previous section, the PCB requires some additional design around the transition parts depending on how the waveguides are connected to the board. Blind vias are utilized through the substrate and plated on the top layer to ensure proper connection to the waveguides of the antenna part. Similar vias are utilized throughout the whole structure and the diameter of the vias is restricted by the wall thickness of the waveguides and of course the manufacturing capabilities.

To further improve the transition, the lower layers of the PCB are removed inside the rectangular waveguide except the top substrate core and the microstrip line. The formed cavity is also plated with metal to enhance the transition performance and to prevent the electromagnetic fields to be excited inside the multilayer PCB. The cavity is presented from the side in Figure 14 and is manufactured by milling process with special tools.

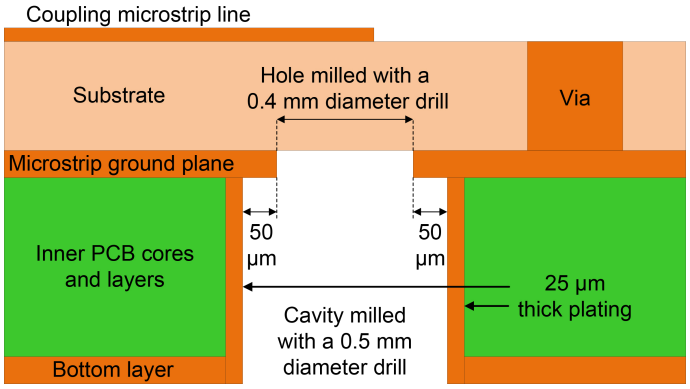

Figure 14: Side view of the cavity made on the PCB to enhance the transition performance. The cavity is plated with 25 µm thick metal.

Due to the manufacturing purposes, a 50-µm wide step is left on the metal plane closest to the substrate to ensure that the substrate is not penetrated by the process. Also, the milling cutters or drills used to make the cavity can not produce exact 90° corners as they have circular profiles. This must be taken into account in the

manufacturing and the simulations. The drill has a 0.4-mm diameter for the milling of the closest metal layer near the substrate and a tool with 0.5-mm diameter is used for the other layers. The metal plating applied to the the lower layers has a thickness of 25 µm. The step size, the drill sizes, and the thickness of the metal plating are restraint by the manufacturing process and therefore identical in both E-band and cm-band structures.

The top substrate is required to exhibit low losses. It needs to be thin as the final structure is required to be as low-profile as possible and to save space for the phase shifters. RT/duroid 5880 ($\varepsilon_r = 2.20$, $\tan\delta = 0.0009$ @10 GHz) with the thickness of 127 µm is finally chosen as the substrate material for both E-band and cm-band structures. The substrate has a low dielectric constant which is assumed to be beneficial from the transition point of view. FR-4 is used for the inner substrate cores. Copper is used as the conductor metal in the conducting layers.

The thickness and the dielectric constant of the substrate along with the thickness and the width of the strip are the main parameters that affect the characteristic impedance of the microstrip line. The impedance of the line is generally chosen to be well matched to the phase shifter impedance. However, for the E-band structure the microstrip line width is optimized for the transition along with other parameters. This can be done as no commercial phase shifters are utilized. The phase shifters are designed separately and their impedance can be chosen according to the optimized line impedance.

For the cm-band, the line width is chosen to be left out of the transition parameter study as the line impedance should be determined according to the impedance of the phase shifter. Initial line impedance is decided to be 50 Ω as the available phase shifter is matched to that impedance.

3.1.3 Waveguide Design for Transitions

The transitions require two rectangular waveguides: one connected to the feeding network and the other connected to the horn antenna. These waveguides are designed to have equal height and width with each other to simplify the design. The dimensions of the waveguides utilized in the transitions are set partly according to simulation studies of the feeding network. Obviously the waveguides utilized in the feeding network must have equal dimensions with the waveguides used in the transitions for the subsequent integration of the different designs. The dimensions are set so that only TE_{10} mode can exist in the waveguide. The standard WR-12 waveguides are utilized in the the E-band design. The width a of the cm-band waveguide is determined using (18). The waveguide height b is decided to be the half of the width i.e. $b = a/2$. The dimensions are more clearly presented in Figure 15.

Both waveguides are tapered to arrange more space for the phase shifter. As presented in Section 2.2.3 and in (18) the waveguide height can be tapered without affecting the propagating wave modes inside the RWG. In the E-band structure, the tapered height is optimized separately. In the cm-band structure, the waveguide height after the tapering is half of the initial height $b_{\text{tapered}} = b/2$. The height could be reduced even more to make more room for the phase shifter but this also

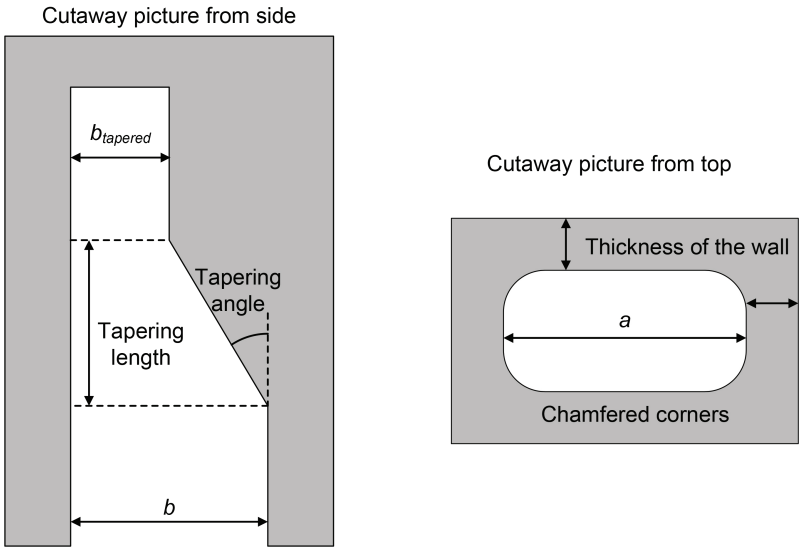

Figure 15: Cutaway view of the waveguide from the side and the top. The dimension parameters of the waveguide are presented. The transition to the PCB is not shown.

deteriorates the transition performance as the transitions become more sensitive to parameter variations. Especially at the E-band such behaviour is unwanted as the the manufacturing errors can have relatively large effect on the parameter values. Furthermore, the tapering is designed to be low-gradient as too abrupt change might cause reflections inside the waveguide.

First, the electromagnetic wave is fed through the tapered RWG and it then couples to the microstrip line on top of the low-loss substrate. In the aforementioned coupling, the wave mode changes from the TE_{10} mode to the quasi-transverse electromagnetic mode, QTEM. In this mode the electromagnetic field is also distributed above the substrate and the conducting line, and thus, a slot in a waveguide is required for the field to pass from the waveguide to the PCB. Evidently the space above the PCB must also be left free of metal in the area of the phase shifter.

In the second transition from the microstrip to the antenna waveguide, the mode changes back to the TE_{10} from the QTEM. Again, the antenna waveguide is tapered similarly as in the previous transition to provide more space for the phase shifter. A broader insight of the mode changes is not presented in this thesis as it would require a substantial amount of theoretical discussion, numerical calculation, and simulations that are not essential for the final design.

The brass is chosen to be the waveguide material as it is quite inexpensive and suits well for milling. The future design is aimed to be manufactured by the plastic injection molding techniques followed by metallization. The injection molding process supports the waveguide structures with the minimum wall thickness of 0.5 mm so this is chosen as the wall thickness for the E-band and cm-band waveguides. Furthermore, the wanted waveguide structures are milled in the brass blocks and as with the PCB, the right-angle corners are not possible because the milling is done with a spinning. The E-band and the cm-band structures have milling tools of different sizes as the E-band structure requires more precise milling.

3.1.4 Transition Parameters

Some parameters are tuned in E-band and cm-band structures to achieve the required electrical properties and others are fixed due to the manufacturing constrictions. The parameters presented in Table 3 are fixed for both frequency bands.

Table 3: Fixed parameter values of the transition structures.

Parameter Description	**Value**
Waveguide wall thickness	0.5 mm
Microstrip thickness, t	18 µm
Substrate thickness	127 µm
Drill diameter in the cavity milling	0.4 mm & 0.5 mm
Cavity plating	25 µm
Step inside the cavity	50 µm

The rest of the parameters related to the transition system are presented in Table 4. The sensitivities of the parameters related to electrical performance are studied by simulations and the found sensitivities are listed in Table 4. Sensitivity defines how much electrical performance is changed due to a small variation in the parameter value. The findings of this parameter study are based on the E-band structure simulations presented in the following section.

Table 4: Transition structure parameters.

Parameter Description	**Sensitivity**
Waveguide width, a	Low
Waveguide height, $b = a/2$	Low
Waveguide height after tapering, b_{tapered}	Medium
Length of the tapered part of the feeding network waveguide	Not studied
Microstrip width, w	Medium
Microstrip length inside the feeding network waveguide, d_1	High
Microstrip length inside the antenna feed waveguide, d_2	High
Microstrip distance from the shorted end of the feeding network, h_1	High
Microstrip distance from the shorted end of the antenna feed, h_2	High
Slot height in the waveguide for the microstrip	Low
Slot width in the waveguide for the microstrip	Low
Antenna aperture size	Not studied
Drill diameter in the waveguide milling	Not studied
Via radius	Low
Via spacing	Low
Thickness of the rest of the PCB board	Low

The most sensitive parameters are found to be the microstrip length inside the waveguide d_1 and d_2 and the microstrip distance from the short-circuited end of the waveguide h_1 and h_2. These parameters are presented in Figure 16. An initial guess for the distance to the shorted end of the waveguide is thought to be around $h_1 = h_2 = \lambda/4$. Theoretical explanation is that the reflected waves from the short-circuited end are at the same phase as the wave reaching the microstrip resulting into a strong coupling. However, the final optimized results prove the optimal distance to be a bit less. One explanation for this is that the propagating wave must travel through the substrate which has a larger dielectric constant than air. Thus, the wavelength of the propagating wave decreases inside the substrate affecting the electrical length of the structure. Therefore, the optimal dimension where the opposing waves are in constructive interference is less than $\lambda/4$.

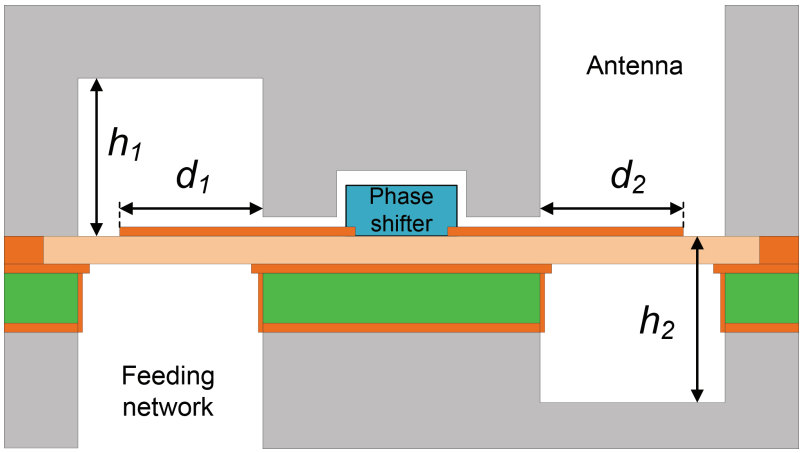

Figure 16: Main parameters of the transition tuning.

The microstrip length inside the waveguide is limited by the tapered waveguide height. Obviously the microstrip is forbidden to be in contact with the waveguide as it would mean a shorted circuit. An adequate gap is required between the stripline and the waveguide wall so that the coupling is effective.

As stated before, the waveguide dimensions are determined mainly by the feeding network dimensions. However, the lengths of the waveguides can be chosen freely, and they are fixed to some round figures to ease the manufacturing. Because the structure is desired to be a low profile, the dimensions should not be excessively large. Gradients in tapered waveguides should be low, i.e. transitions should be smooth to facilitate manufacturing and to avoid reflections.

Obviously, some parameters such as the tapered waveguide height and the microstrip length inside the waveguide are dependent on each other with respect to the sensitivity: when one parameter is altered, the sensitivity of the other is changed. However in such cases, the parameter which is assumed to have worse manufacturing accuracy, is considered the more sensitive one. Also, the waveguides are considered somewhat fixed structures and tuning is mainly realized varying PCB-parameters.

The slots in the waveguides for microstrip lines have width and height that can be chosen quite freely. Evidently, the dimensions are restricted by the waveguide

dimensions but very large dimensions for the slot are not necessity. However, the width and height of the slot must be relatively larger than the microstrip thickness and width so that the propagating TEM-wave is not compromised by the slot. Good rule of thumb is to choose the slot width to be several microstrip line widths and then round it up to some reasonable value. Accordingly, the slot height should be several times the substrate thickness.

The diameter of the vias is restricted by the waveguide thickness to the maximum of 0.5 mm. The minimum diameter and the required space between adjacent vias is determined by the manufacturing capabilities. As the waveguide dimensions are different between E-band and cm-band structures, the quantity and the parameters of the vias are chosen accordingly.

Furthermore, the overall PCB thickness also varies between the different structures. The E-band structure does not require control lines implemented into the PCB, hence a thinner board is suitable. Yet, the FR-4 core is required to make the board more rigid. The cm-band structure requires several control lines, and thus, the board becomes thicker. The thickness of the PCB does not affect the transition almost at all as long as the cavities of the PCB are plated thoroughly. The only restriction is that the thickness can not exceed the parameter h_2, the microstrip distance from the short end of the antenna feed.

3.2 E-band Transitions

The transition study for E-band is started by first designing the transition from the waveguide to the PCB as that is also the first transition in the operational system. The transition is designed to be as simple as possible to ease the manufacturing process as the design dimensions can be fractions of the wavelength. The wavelength λ for E-band (71–86 GHz) varies from 3.49 mm to 4.22 mm thus necessitating a very precise manufacturing. Even though the E-band phase shifters in this thesis are fixed, the transition design should be such that the fixed phase shifters could be replaced with adjustable phase shifters in the future.

Firstly, the simulation models and the optimized parameters are presented. Subsequently, the simulation results for the given parameters are described. Finally, the available room for the phase shifter, which is affected e.g. by the antenna element spacing, is evaluated. If the area for the phase shifter is not sufficient, the transition structure must be reshaped without affecting the transition performance. The proposed solution is described in Section 3.2.3.

3.2.1 E-band Simulation Models and Parameters

The simulation model of the waveguide-to-PCB transition is presented in Figure 17a. This particular model is for the E-band structure but as said, both models are identical. The dimensions are scaled according to the wavelength excluding some manufacturing-dependent parameters, such as the wall thickness of the waveguides. The waveguide is excited with a CST waveguide port presented in Section 2.4 from the bottom of the waveguide so it is not visible in the figure. The transmission

monitoring is done with similar port on the PCB cut-out, marked with number 2. The waveguide tapering and the slot for the microstrip line are also visible in the aforementioned figure. The simulation model of the PCB-to-waveguide transition structure is presented in Figure 17b. It is somewhat similar to the previous model but here the waveguide port is used to excite the PCB and the microstrip line and the transmission is evaluated by the waveguide port inside the waveguide which is not visible in the figure. These structures are connected to each other with the phase shifter between them in the final simulation model.

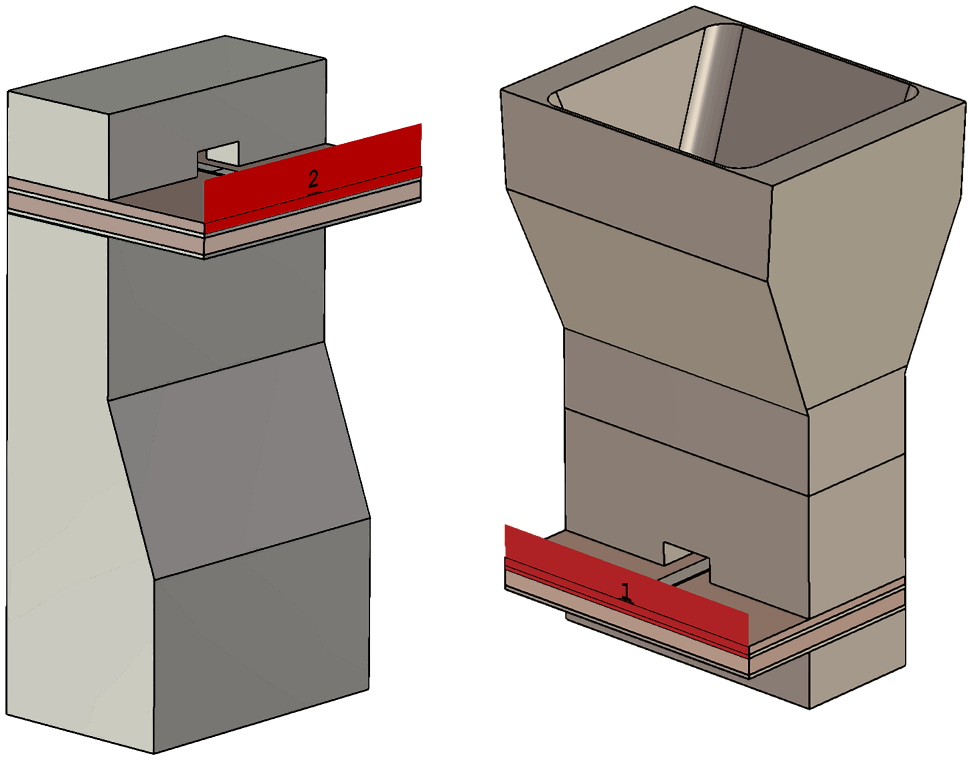

(a) (b)

Figure 17: Simulation models of the E-band transition structure: (a) the waveguide-to-PCB transition and (b) the PCB-to-antenna transition.

The parameters are numerically optimized in CST Microwave Studio for the highest possible transmission coefficient. After the optimization, a study is conducted to determine the range in which the errors in manufacturing are tolerable without harming the overall performance of the transitions. The target for the single transition performance is to have the transmission coefficient higher than -0.6 dB and the reflection coefficient below -10 dB across the whole band. Table 5 lists the optimized parameters.

It is notable that the microstrip width is one of the optimized parameters and the microstrip line impedance is around 68 Ω. As the commercial microwave phase shifters are commonly matched to 50 Ω, a separate impedance transformer or match-

Table 5: E-band transition structure parameters.

Parameter Description	**Value**
Waveguide width, a	2.7 mm
Waveguide height, $b = a/2$	1.35 mm
Waveguide height after tapering, b_{tapered}	0.6 mm
Length of the tapered part of the feeding network waveguide	2 mm
Microstrip width, w	0.22 mm
Microstrip length inside the feeding network waveguide, d_1	0.52 mm
Microstrip length inside the antenna feed waveguide, d_2	0.52 mm
Microstrip distance from the shorted end of the feeding network, h_1	0.52 mm
Microstrip distance from the shorted end of the antenna feed, h_2	0.56 mm
Slot height in the waveguide for the microstrip	0.3 mm
Slot width in the waveguide for the microstrip	0.7 mm
Antenna aperture size	3.1 mm
Drill diameter in the waveguide milling	0.4 mm
Via radius	0.05 mm
Via spacing	0.1 mm
Thickness of the PCB board	427 µm

ing network should be implemented. Other possibility is to redesign the microstrip width for the 50-Ω impedance but then the transition must be tuned accordingly. However, this can be very suitable option as the area for the phase shifter is limited and introducing new elements to the transmission line consumes valuable space. As the E-band phase shifters for this work are designed individually, the line impedance can be taken into account early in the design process.

3.2.2 Simulation Results of the E-band Transition

The simulations are carried out in the CST Microwave Studios and the reflection and the transmission coefficients are calculated to evaluate the transition performance. The reflection coefficient is evaluated by S_{11}-parameter and the transmission coefficient is evaluated by S_{21}-parameter.

The simulated S-parameter results of the waveguide-to-PCB transition are presented in Figures 18a and 18b. The reflection coefficient is well below -10 dB, almost less than -14 dB for the majority of the band. The main resonance is around 74 GHz. These results are backed up by the transmission results which indicate that the transmission coefficient is higher than -0.4 dB almost for the whole band. The lower part of the band is not as well matched as the rest of the band.

Simulated reflection and transmission of the PCB-to-antenna transition are presented in Figures 19a and 19b. Now the reflection is stronger than in the waveguide-to-PCB transition. It is below -15 dB while the transmission is more than -0.3 dB. The main resonance is around 77 GHz where the transition performance is almost

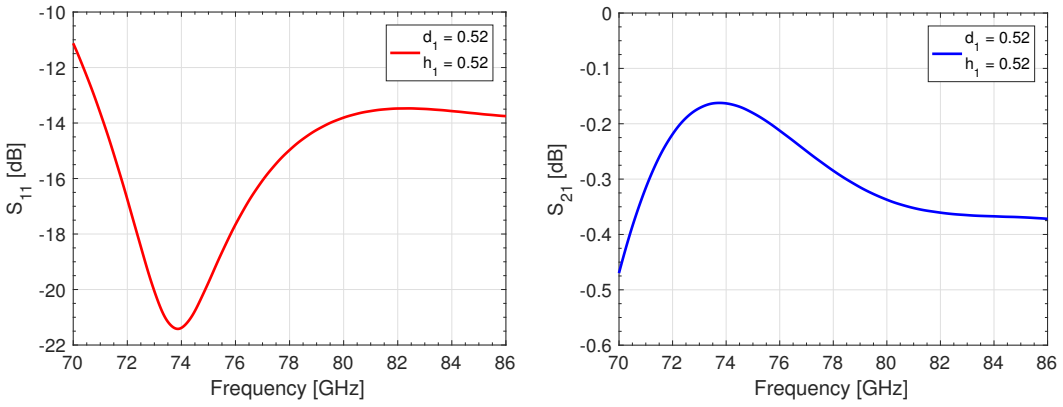

(a) (b)

Figure 18: Simulated results of the waveguide-to-PCB transition: (a) reflection coefficient and (b) transmission coefficient. Dimensions are in millimeters.

perfect without considering the material losses.

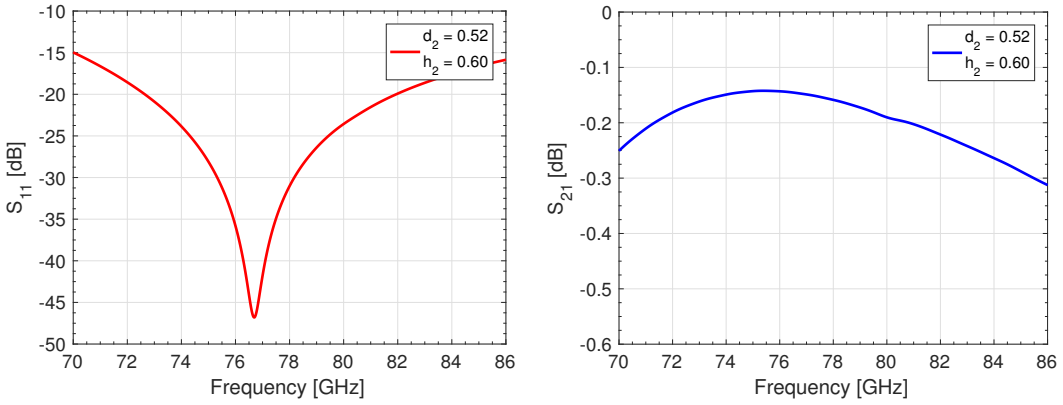

(a) (b)

Figure 19: Simulated results of the PCB-to-antenna transition: (a) reflection coefficient and (b) transmission coefficient. Dimensions are in millimeters.

A sensitivity analysis is performed for the most significant parameters, d_1, d_2, h_1, and h_2. As previously mentioned, d_1 and h_1 are parameters related to the waveguide-to-PCB transition and d_2 and h_2 are related to the PCB-to-antenna transition. The analysis is performed for both transitions separately. It is done by varying one transition parameter while keeping the other parameter constant at the optimized value. Thus, the effect of parameter value change to the transition performance can be evaluated. Also, the previously presented optimized results can be seen as the reference values in the result figures. Both reflection and transmission results of the parameter sensitivity analysis are presented.

The waveguide-to-PCB transition parameters d_1 and h_1 are evaluated in Figures 20 and 21. Of these d_1 is clearly more sensitive to the variation, with value $d_1 = 0.52$ mm the resonance is the strongest. A change in d_1 alters the reflection and

transmission coefficient and if the transmission coefficient should be above −0.6 dB, $d_1 = 0.52$ mm can be varied ±30 µm.

The parameter h_1 on the other hand is not that sensitive. It can be seen from Figure 21a how the change of the distance h_1 moves the main resonance frequency over the bandwidth. However, even though the reflection coefficient improves quite dramatically at the higher frequencies, the matching deteriorates especially at the lower band. Still, around ±60µm variation is allowed from the value $h_1 = 0.52$ mm to achieve the required performance.

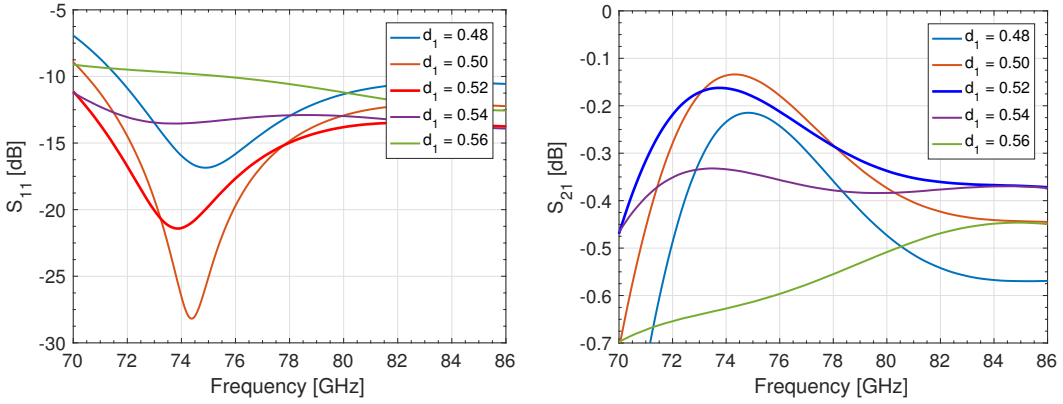

(a) (b)

Figure 20: Sensitivity analysis results of the waveguide-to-PCB transition parameter d_1: (a) reflection coefficient and (b) transmission coefficient. Dimensions are in millimeters.

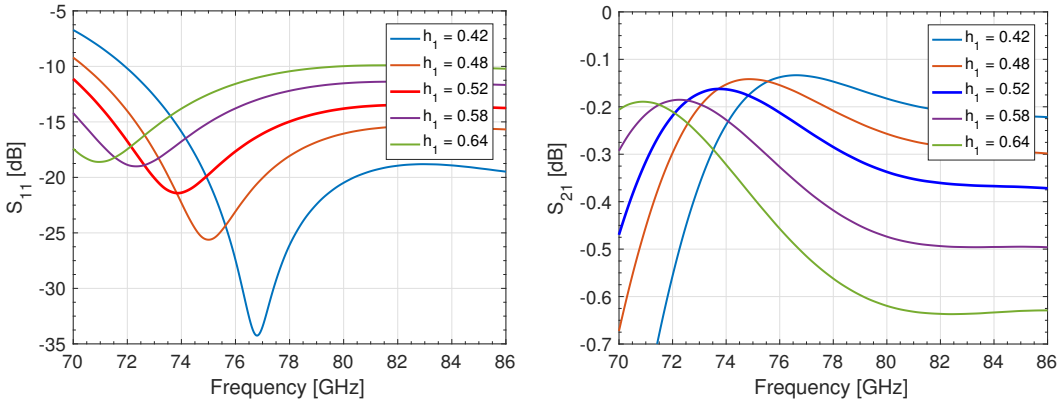

(a) (b)

Figure 21: Sensitivity analysis results of the waveguide-to-PCB transition parameter h_1: (a) reflection coefficient and (b) transmission coefficient. Dimensions are in millimeters.

The effect to PCB-to-antenna transition parameters d_2 and h_2 are shown in Figures 22 and 23. The parameter variation shows correspondence to the waveguide-to-PCB results and the behaviour is similar with the respecting parameters. In the

PCB-to-antenna transition the optimized main resonance is at 77 GHz and the allowed variation from $d_2 = 0.52$ is again ± 30 µm. However h_2 can be varied much more freely, almost ± 100 µm.

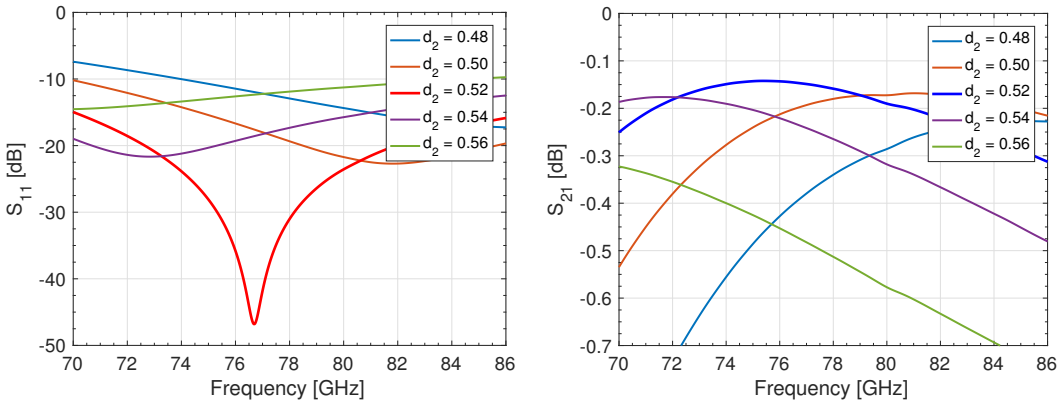

(a) (b)

Figure 22: Sensitivity analysis results of the PCB-to-antenna transition parameter d_2:(a) reflection coefficient and (b) transmission coefficient. Dimensions are in millimeters.

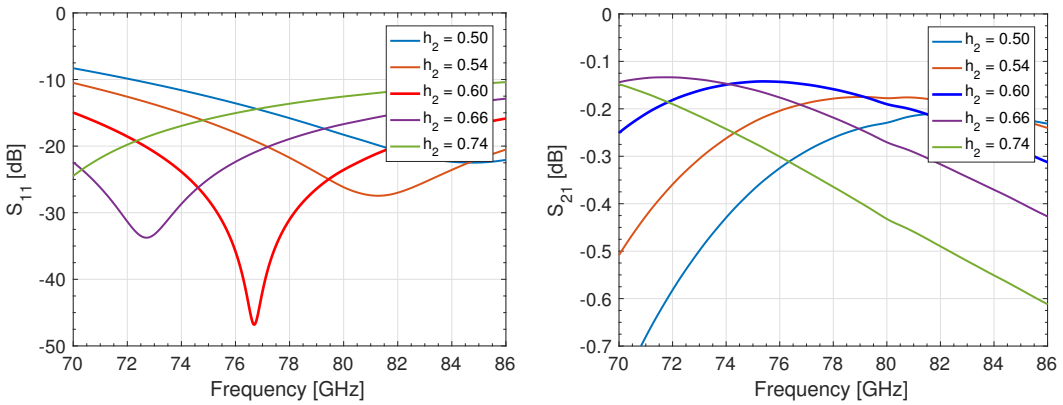

(a) (b)

Figure 23: Sensitivity analysis results of the PCB-to-antenna transition parameter h_2: (a) reflection coefficient and (b) transmission coefficient. Dimensions are in millimeters.

3.2.3 Required Space for the Phase Shifter

The antenna study suggested that the desired horn element spacing should be $\lambda/2$. However, the width of the feeding waveguide is set to be 2.7 mm to accommodate the TE_{10} mode. This is greater than $\lambda/2$ which is 1.75 mm – 2.11 mm over the E-band. As the beam-steering range is aimed to be the same in both directions, the elements are designed to be symmetrical. Thus, the horn antenna elements have a

square profile and the size of the one end is 3.1 mm. The elements are spaced next to each other with a 0.1-mm separation between the two adjacent edges. Thus, the gap from the center of one antenna element to another is 3.2 mm. Furthermore, this indicates that there is a 1.1 by 3.2 mm^2 space for the phase shifter installation. The 1.1-mm space is left between the waveguide of the feeding network and the antenna. Perpendicular to that, the 3.2-mm space can be used without affecting the adjacent elements. The dimensions are presented from the side in Figure 24 and from the top in Figure 25.

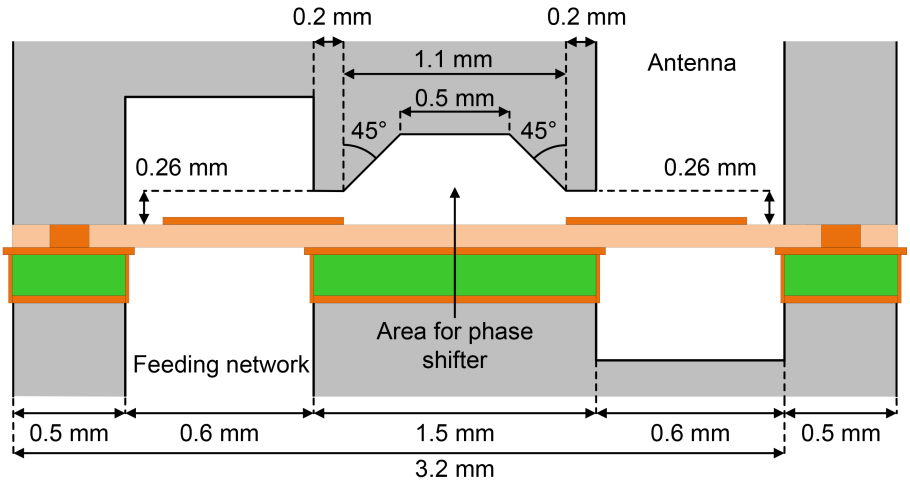

Figure 24: Side view of the area for the phase shifter.

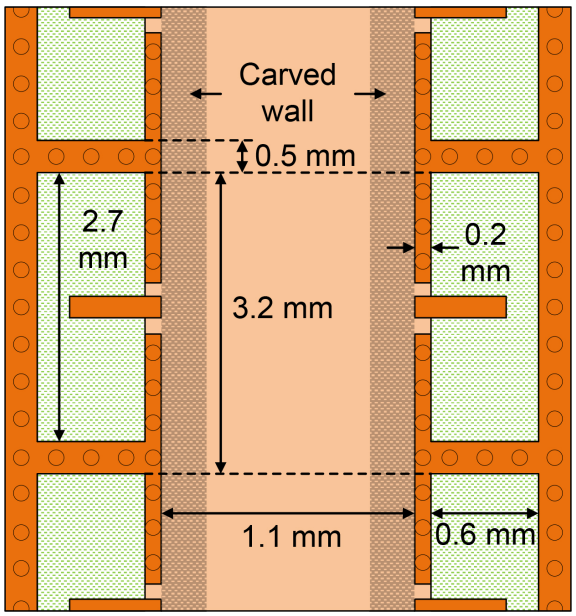

Figure 25: Top view of the area for the phase shifter.

As mentioned before, the phase shifters need more space to be mounted and the waveguides are tapered to fit the phase shifter between the two transitions. However, this tapering is not sufficient for the phase shifter implementation. Hence, the walls of the waveguides are carved and reshaped as presented in Figure 24 to make more space for the phase shifter. Carving the walls of the waveguides does not affect the transition, and it is thus a suitable solution to add more room for the phase shifter. Also, it is seen feasible with respect to the injection molding.

Other techniques to increase the area for the phase shifter include manipulation of the waveguide dimensions. The waveguides can be filled with dielectric material which allows more compact waveguide width or they can be tapered more. Further tapering of the transition waveguides is studied more thoroughly of these two options. However, even though the height of the waveguides can be reduced quite much, the structure becomes too sensitive to the small parameter changes, hence being very challenging to manufacture. The sensitivity analysis is conducted for the waveguide which is tapered to the height of 0.43 mm. This structure tolerates only ± 10 µm variation for the microstrip distance d_1 and d_2 which is extremely hard to achieve with available manufacturing technologies.

3.3 Cm-band Transitions

The E-band simulations are conducted before the cm-band simulations and many findings of the previous work are employed to conduct the cm-band simulations more efficiently. Similar parameters are utilized and the initial parameter values are acquired by scaling the E-band structure dimensions for the cm-band structure. The wavelength λ for the cm-band (26–30 GHz) varies from 9.99 mm to 11.53 mm.

In the following, the simulation model and the optimized parameters for the cm-band structure are presented. Thereafter, the simulation results for the given band are examined. However, opposite to the E-band structure where more space for the phase shifters is demanded, the cm-band structure dimensions are relatively large compared to the chosen phase shifter chip. Thus, no additional space for the phase shifter integration is required than is provided by the initial design.

3.3.1 Cm-band Simulation Models and Parameters

Opposed to the E-band structure where the transitions were studied separately, in the cm-band simulation model these two transitions are studied together from the start. The two parts are connected to each other with straight microstrip line which will be replaced with the phase shifter in the final design. The simulation model is presented in Figure 26. The waveguide port is used to excite the waveguide of the feeding network and a similar port is utilized inside the waveguide of the antenna to evaluate the transmission coefficient.

Similarly to the E-band, the cm-band parameters are numerically optimized in CST Microwave Studio with emphasis on the high transmission coefficient. The sensitivity analysis is also performed again to the most significant parameters, d_1, d_2, h_1, and h_2. The optimized parameters are presented in Table 6.

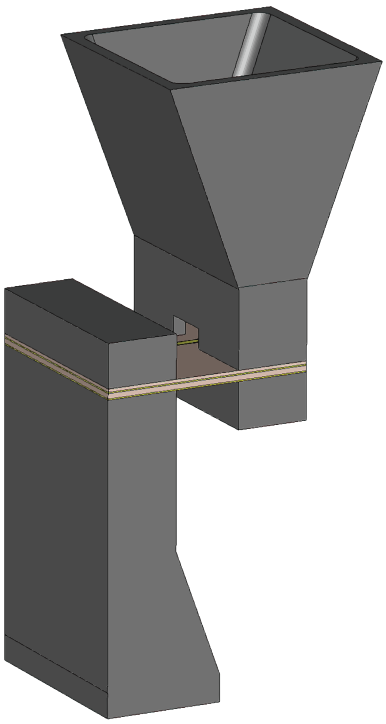

Figure 26: Simulation model of the cm-band transition structure.

Table 6: Cm-band structure transition parameters.

Parameter Description	**Value**
Waveguide width, a	7.4 mm
Waveguide height, $b = a/2$	3.7 mm
Waveguide height after tapering, $b_{\text{tapered}} = b/2$	1.85 mm
Length of the tapered part of the feeding network waveguide	5 mm
Microstrip width, w, Scaled for 50 Ω	0.34 mm
Microstrip length inside the feeding network waveguide, d_1	1.66 mm
Microstrip length inside the antenna feed waveguide, d_2	1.62 mm
Microstrip distance from the shorted end of the feeding network, h_1	1.25 mm
Microstrip distance from the shorted end of the antenna feed, h_2	1.85 mm
Slot height in the waveguide for the microstrip	0.8 mm
Slot width in the waveguide for the microstrip	2 mm
Antenna aperture size	7.8 mm
Drill diameter in the waveguide milling	1 mm
Via radius	0.1 mm
Via spacing	0.2-0.25 mm
Thickness of the PCB board	927 µm

3.3.2 Simulation Results of the Cm-band Transition

Both transitions are simulated together and the reflection and transmission coefficients of the whole structure are presented in the following. Figure 27a presents the simulated reflection coefficient and Figure 27b the simulated transmission coefficient. Optimized parameters are used in the simulations.

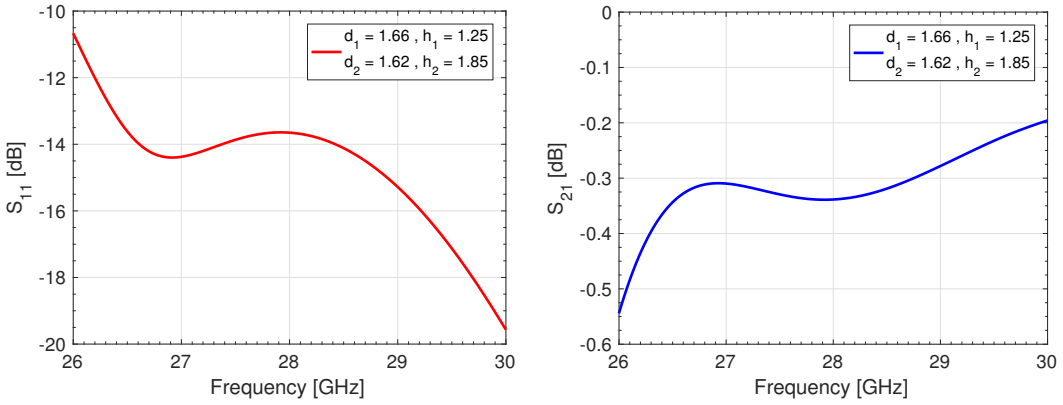

(a) (b)

Figure 27: Simulated results of the cm-band transition structure: (a) reflection coefficient and (b) transmission coefficient. Dimensions are in millimeters.

The reflection coefficient of the structure is around -14 dB for the most of the band. The matching is a bit poorer at the lower frequencies and on the contrary, the main resonance is at the higher frequencies. The transmission coefficient corresponds very well to the reflection coefficient results and the coefficient is above -0.3 dB for the majority of the band.

Once again the parameter sensitivity analysis is performed to d_1, d_2, h_1, and h_2. The analysis is performed to the one transition parameter at a time by varying the chosen parameter while keeping the other three parameters constant at the optimized values. The effect of the parameter value change to the transition performance is evaluated and the previously presented optimized results are seen as the reference values at the result figures. Both S_{11} and S_{21} of the parameter sensitivity analysis are presented.

The sensitivity analysis results of the parameters d_1 and d_2 are presented in Figures 28 and 29, respectively. Like with the E-band parameters, the change of the d_1 and d_2 values affects the magnitude level of the matching. Actually as the strip lengths are decreased, the matching improves at the main resonance frequency, but the overall matching across the whole band degrades. Especially, the lower part of the bandwidth becomes poorly matched. Furthermore, the cm-structure is not as sensitive to the parameter variation as the E-band structure. Both d_1 and d_2 can be changed about ± 60 µm from their optimized values for the transmission coefficient still to remain above -0.8 dB and the reflection below -9 dB across the whole band.

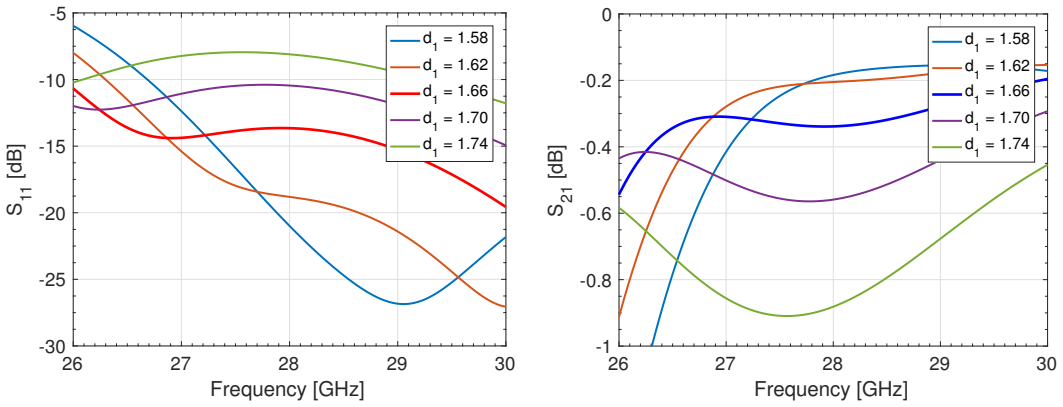

(a) (b)

Figure 28: Sensitivity analysis results of the transition parameter d_1: (a) reflection coefficient and (b) transmission coefficient. Dimensions are in millimeters.

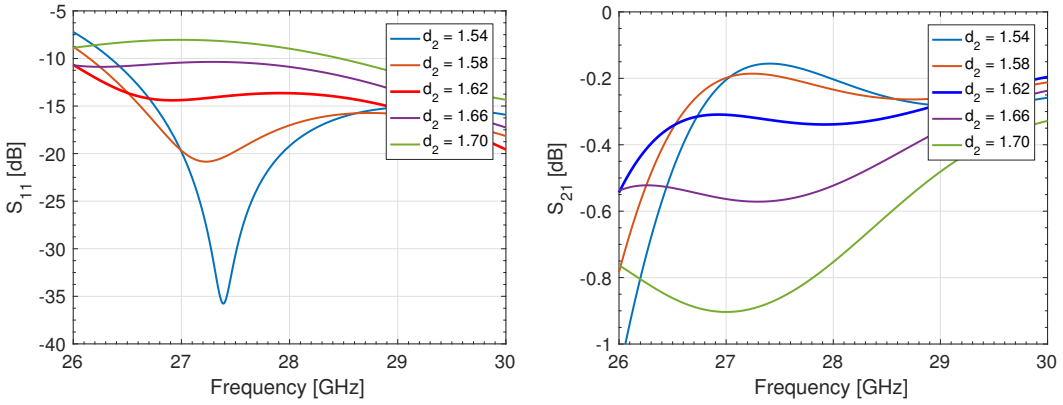

(a) (b)

Figure 29: Sensitivity analysis results of the transition parameter d_2: (a) reflection coefficient and (b) transmission coefficient. Dimensions are in millimeters.

The sensitivity analysis results of the parameters h_1 and h_2 are presented in Figures 30 and 31. With the E-band structures the change of h_1 and h_2 values clearly moves the main resonance from one frequency to another. With the cm-band structure analysis no similar correspondence is found. However, the E-band transitions are evaluated separately, while the cm-band transitions are combined and the effect is thus perhaps smaller. Moreover, the parameter change actually has a very little effect to the overall transition performance. The transmission coefficients are more than -0.4 dB for the frequencies above 27 GHz with the most of the inspected h values. The optimal values can be varied quite freely ± 100 µm without the transmission coefficients dropping below -0.6 dB and the reflection coefficient exceeding -10 dB.

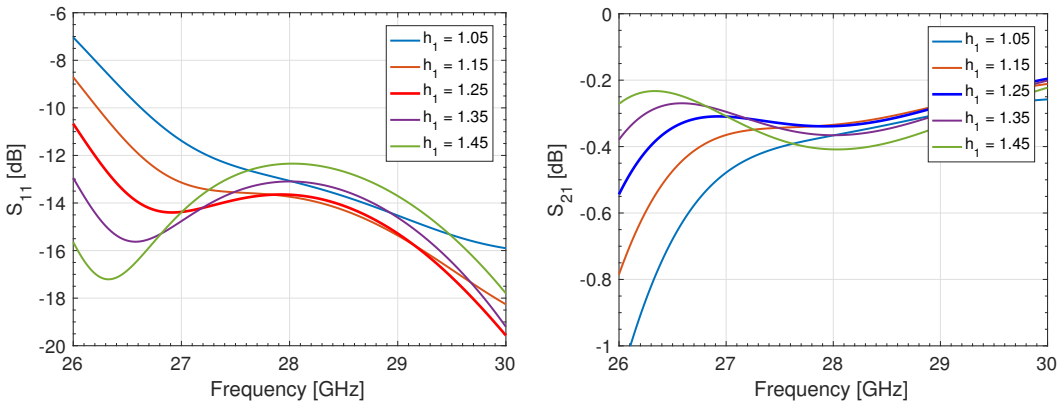

(a) (b)

Figure 30: Sensitivity analysis results of the transition parameter h_1: (a) reflection coefficient and (b) transmission coefficient. Dimensions are in millimeters.

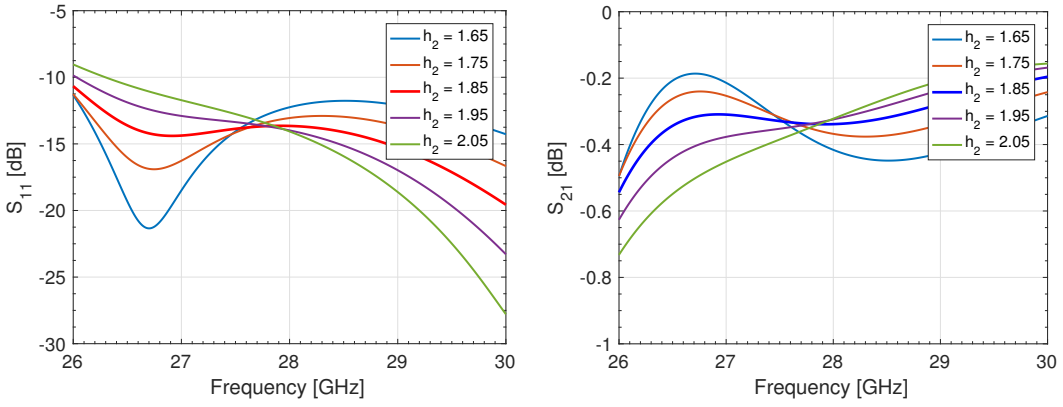

(a) (b)

Figure 31: Sensitivity analysis results of the transition parameter h_2: (a) reflection coefficient (b) transmission coefficient. Dimensions are in millimeters.

3.4 Further Improvements to the Transitions

The simulation results show that the proposed transitions have fairly good performance over the desired frequency bands and that they have some tolerance to the manufacturing errors. However, few improvements could be done for the future applications to improve the performance and error tolerance.

The literature study shows that the many transition solutions have a larger microstrip patch as a probe. This probe patch is matched to the nominal microstrip line with a quarter-wave impedance transformer. The utilization of the patch could decrease the reflection coefficients and increase the transmission coefficients even further; quite promising results are reported for example in [70]. However, such probe and impedance transformer can be problematic in the given structure as the space for the phase shifters is already restricted. The proposed additions to the design might reduce the available space even more and they also make the design and potentially the manufacturing more complicated.

The proposed design has the whole cross-sectional area of the waveguide filled with the substrate whereas the transitions presented in the literature have substrate only in the near vicinity of the probe patch [70], [71], [73], and [74]. Thus, in the design presented in this thesis, the propagating wave must travel through the substrate which can be a performance degrading factor. Removal of the substrate from the sides of the probe could potentially increase the transition performance, but it can also compromise the PCB integrity. The possibility to manufacture such structure should be investigated before the design is changed. Furthermore, the removal of the substrate could suggest quite large variations to the transition parameters, especially on h_1 and h_2. Yet, more research and simulations for such structures would be beneficial.

Other ways to increase the transition performance, i.e. the probe matching to the waveguide include ridged waveguide impedance transformers. The ridges are often utilized to match the microstrip line that is along the propagation direction of the waveguide. However, matching in the case where the coupling is transverse to the propagation direction should be looked more in-depth. For the waveguide-to-coaxial transitions such transformer structures exist but whether they could be used for the microstrip line is uncertain. Such structure could also lead to the design where the height of the waveguide is tapered even more than in the existing structure, leaving more space for the phase shifter.

Finally, it is proposed that the matching could be improved by filling the waveguides with some dielectric material to decrease the characteristic impedance of the propagating wave closer to the characteristic impedance of the microstrip line. However, it would require extensive research to ensure that the proposal is valid and that the dielectric losses inside the waveguide would not increase too much to deteriorate the performance.

4 Phase Shifter Characterization and Measurements

Transition structures without phase shifters are presented in the previous chapter. The final functional phased array requires integration of the phase shifters on the PCB. In addition, as stated in Section 2.3, the phase shifters are the key components of the phased arrays and their performance as a part of the antenna system is the main interest of this study. Thus, their characteristics should be known for the construction of the complete phased array model.

This chapter presents the characterization and the measurements of the phase shifters for both E-band and cm-band. Firstly, the E-band phase shifters are presented. These phase shifters are self-designed at Aalto University, and the working principle of the device is briefly discussed along with the simulated results. After that, the measurement results for the given phase shifters are discussed. Secondly, the commercial phase shifters for the cm-band are experimentally characterized with a self-designed test structure. Experimental characterization is aimed to result in a phase shifter model that can be utilized in designing the antenna prototype. Thirdly, the test structure for the cm-band phase shifters made by Nokia Bell Labs is presented and evaluated. Finally, concluding remarks are given and the future work for the phase shifter integration is discussed.

4.1 E-band Phase Shifter Characterization

As stated in Section 2.3.11, no suitable commercial phase shifters are found for the E-band antenna. Therefore, fixed microstrip line-based phase shifters are designed and implemented to demonstrate the antenna beam-steering. First, the design of the E-band phase shifters is introduced along with the simulated S-parameter results. Finally, the measured results of the E-band phase shifter performance are shown.

4.1.1 E-band Phase Shifter Design

It is shown in (16) that the phase can be controlled by varying the microstrip length. E-band phase shifters are microstrip line-based true time delay phase shifters with different fixed lengths. The shortest line is chosen to be the reference line with 0° phase shift and the other lines are made longer to achieve the desired time delays. The E-band phase shifter is designed to have similar performance as the 5-bit cm-band phase shifter, i.e. the phase tuning range is full 360° and the resolution is 11.25°. The resolution requirement suggests that 32 phase shift states are needed, directly leading to the design of 32 different phase shifters.

The main restriction for the design is dictated by the available area for the phase shifter as discussed in Section 3.2.3. The available space from transition to transition is 1.1 mm. The space in this direction is limited by the waveguides of the feeding network and the antenna. Adjacent array elements restrict the space to 3.2 mm in the perpendicular direction. Due to these restrictions, the phase shifter length is chosen to be adjusted in the direction of the adjacent elements. In reality, the whole 3.2 mm space cannot be utilized as some distance should be left

between the adjacent phase shifters since if they are too close to each other, mutual coupling occurs. However, this restriction is later shown not to be a problem with the proposed design.

Figure 32 shows the phase shifter structure from the top. To ensure that the structure has enough length for the 360° phase variation, two meanders are introduced somewhat symmetrically. The phase shifter design is very simple, allowing the phase shift to be controlled by changing only one design parameter. Variable x denotes the length parameter that is changed to achieve the needed phase shift. The input and output are kept at the same center location through the variation, i.e. the meanders are brought closer or further from each other while x is changed.

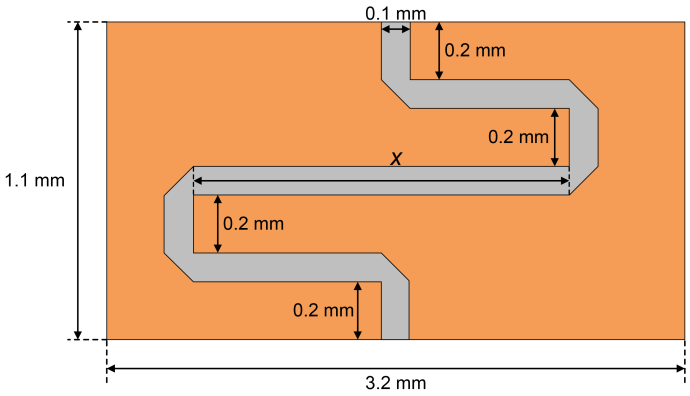

Figure 32: E-band phase shifter structure from the top. x denotes the varied length parameter.

Since the space limitation from transition to transition is the strictest, the width of the phase shifter line is chosen according to it. The microstrip line cannot be bended to follow the edge of the allocated space as the line would then be in contact with the waveguide wall. Thus, a 0.2-mm space is left between both the microstrip and waveguide, and the parallel microstrip lines. Especially, with the parallel lines some distance is required to avoid coupling as much as possible. It is suspected that too strong coupling due to narrow spacing might make the phase shifter to resemble a filter.

After the safe distances, a 0.3-mm space is left for the microstrip line. As three parallel lines are required to have two meanders, the width for the equal lines is 0.1 mm. However, this produces some transmission losses to the final system due to the mismatch between the transition structures and the phase shifter. The microstrip lines in the transition structures have the width of 0.22 mm opposed to the 0.1-mm line of the phase shifter. Nevertheless, this must be accepted as there is no place for the matching circuits in the structure.

4.1.2 E-band Phase Shifter Simulations

Simulations indicate that x should be tuned from 0.40 mm to 1.90 mm to have 360° phase shift. Furthermore, the available space is adequate for the phase shifter implementation. The phase shift is a linear function of the microstrip line length,

thus the tuning range 0.40–1.90 mm is discretely divided to 32 phase states. In theory, each state has 11.25° phase difference with adjacent states. However, in the final fabricated antenna prototype, all the states are not required for the operative demonstration of the beam-steering array. Table 7 presents the most frequently used values of x for the phase shifters. In addition, the simulated phase shift values at 73.5 GHz are presented. The measurement results of these phase shifters are presented in the following section.

Table 7: Mostly used phase states of the E-band phase shifter in the antenna prototype.

State	x [mm]	Simulated phase shift [°]
1	0.40	Reference, 0
2	0.448	9.88
6	0.64	53.12
9	0.786	88.68
10	0.834	100.66
11	0.892	115.26
16	1.124	174.09
17	1.174	186.73
18	1.222	198.81
21	1.366	234.68
24	1.50	267.47
25	1.56	282.00
28	1.706	317.17
29	1.774	333.55
31	1.85	351.94
32	1.90	364.11

The designed phase shifters are simulated in CST. Figure 33 presents the simulated reflection and transmission coefficients for the chosen phase states 1, 9, 17, 25 and 32. These states are chosen as they cover the whole tuning range of x and they have also significantly different phase shifts. The states are used to describe the phase shifters in the subsequent simulations and measurements.

Figure 33a shows that the reflections are effectively nonexistent at the reference state, while the matching is worse at higher states where the resonance occurs at lower frequencies. However, when x is increased enough, a new resonance is formed at the higher frequencies as seen from the graph of state 32. It is assumed that the weakened matching and the new resonance might be caused by the coupling between the adjacent microstrip lines of the phase shifter. Coupling is the weakest in the reference state where the line is shortest. With the following states, the coupling becomes stronger. However, when the length is long enough, the interference caused by the coupling improves the matching. This theory is backed up by the transmission

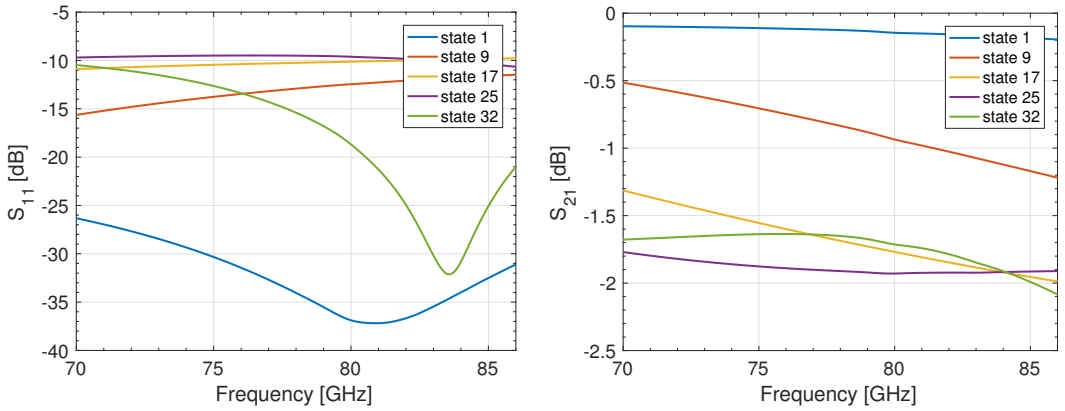

(a) (b)

Figure 33: Simulated results of the E-band phase shifter: (a) reflection coefficient and (b) transmission coefficient.

coefficient results in Figure 33b. The dielectric losses rise along with the microstrip line length, and even though the matching for the state 32 improves, these losses are still quite high. This can especially be seen around 84 GHz frequency, when comparing losses and matching of the states 17, 25, and 32. The conductor losses are not taken into account in the simulations: perfect electric conductor (PEC) is used to simulate the microstrip lines to reduce the simulation time.

Figure 34 presents the phase shifting capabilities of the designed phase shifter. Figure 34a shows the transmission coefficient phase of the states 1, 9, 17, 25, and 32 over the frequency. Figure 34b describes the phase shift as a function of x at 73.5 GHz frequency. The relation between the phase and x is almost linear.

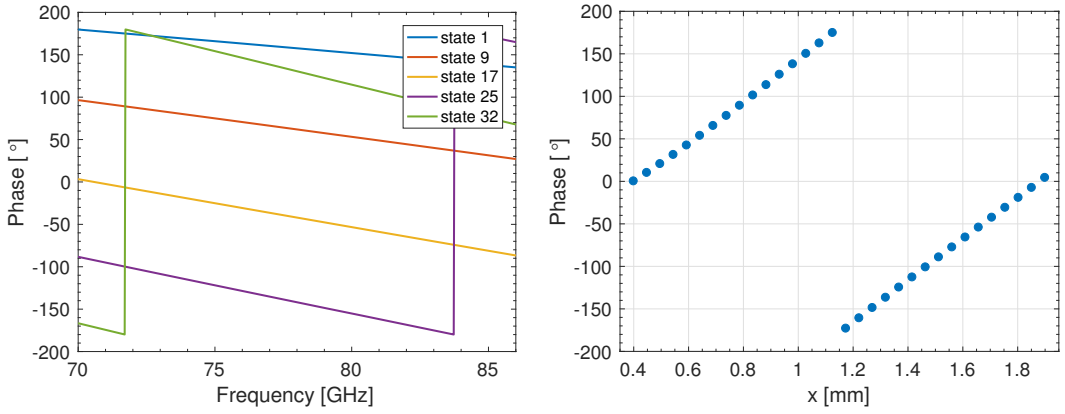

(a) (b)

Figure 34: Simulated (a) transmission coefficient phase and (b) transmission coefficient phase as a function of x at 73.5 GHz.

Phase shifters are also simulated as a part of the transition structure. Figure 35 shows the simulated reflection and transmission coefficient. Figure 35a shows that the main resonance frequency shifts to lower frequencies with higher states.

However, a new resonance appears at the upper band when the states are high enough as suggested by the reflection coefficient of the state 25.

The total simulated transmission losses are a bit higher than what the individual transition and phase shifter simulations suggest. This is primarily caused by mismatch between transitions and the phase shifter. The simulator is utilized to calculate the line impedances of the microstrip lines in phase shifters and transitions and their values are found to be about 98 Ω and 69 Ω, respectively.

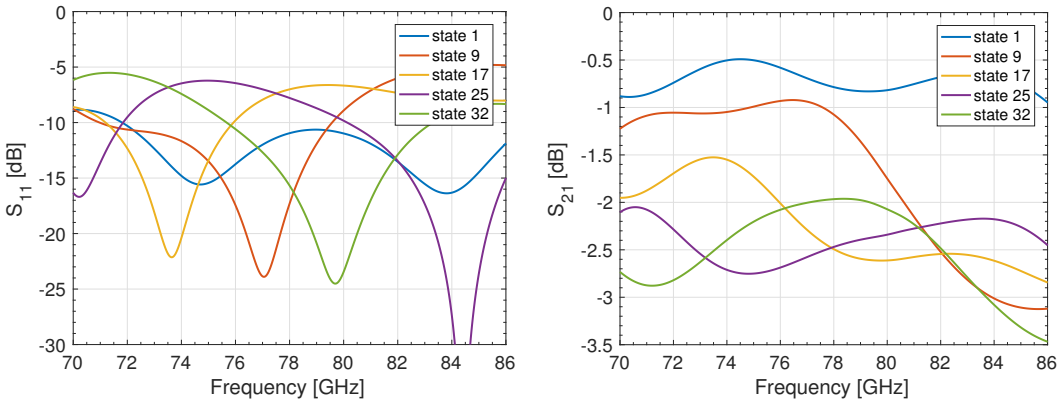

(a) (b)

Figure 35: Simulated results of the E-band phase shifter as a part of the transition structure: (a) reflection coefficient and (b) transmission coefficient.

4.1.3 E-band Phase Shifter Measurements

To ensure that the designed phase shifters work as intended, a specially made test structure is fabricated. The test structure contains the aforementioned 16 different phase shifters (states, see Table 7) that are to be measured. The measurements are carried out in a probe station at Aalto University. For the probe station measurement purposes, a matching circuit is designed to be used with each phase shifter. Figure 36 presents the measured test structure of the phase shifter.

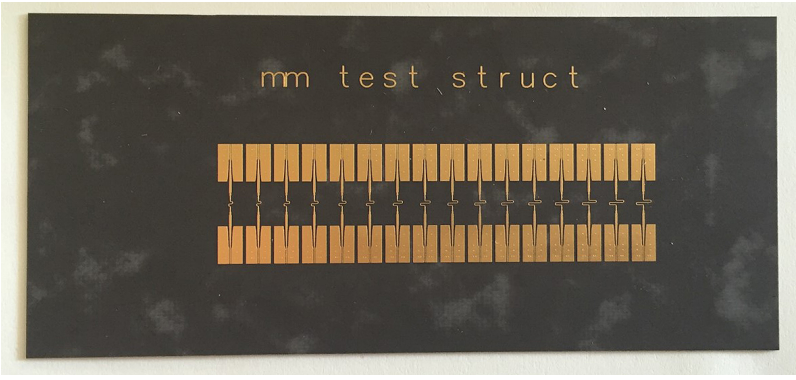

Figure 36: Photograph of the measured E-band phase shifter test structure.

Figure 37a shows the reflection coefficient and Figure 37b shows the transmission coefficient of the fixed phase shifters of states 1, 9, 17, 25, and 32. The results show that the measured losses are much higher than what is anticipated based on the simulation results. Some of the mismatch shown especially in Figure 37a can be explained by the non-ideal performance of the matching networks. However, the matching between the coplanar probe and the test board is not well-known and it is most probably the main cause of the poor matching. Additionally, the conductor losses of phase shifters, which were neglected in simulations, are present. However, the phase shifter performance through measurements should be studied more as the possibility of simulation errors cannot be omitted either.

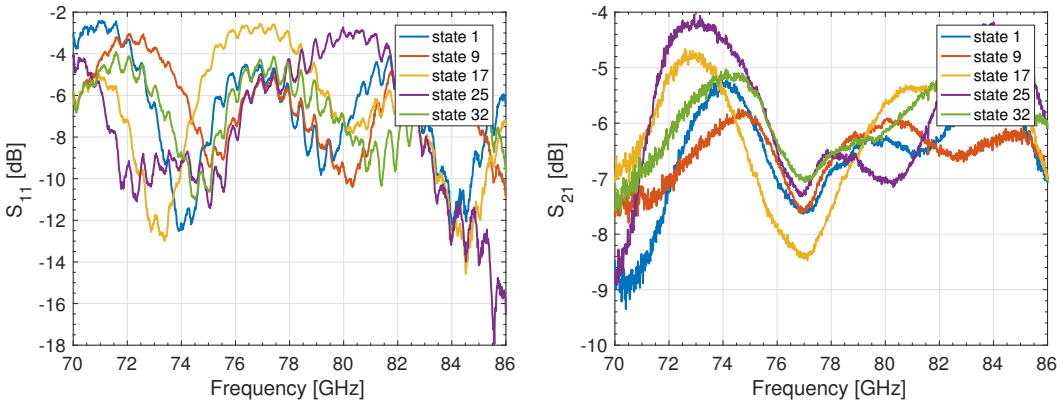

(a) (b)

Figure 37: Measured results of the E-band phase shifter: (a) reflection coefficient and (b) transmission coefficient.

Phase response of the designed phase shifters is the most important factor for the beam-steering demonstration. Figure 38 presents the phase response of all the important states. The phase shifts between different states are similar to the simulated values, although some variation exists. For example, the phase difference should be larger between the states 1 and 9, and on the contrary, smaller between the states 16 and 17. Furthermore, the measurements show that states 18 and 21 do not have any apparent phase shift between them as neither do the states 24 and 25. These are thought to be caused by the manufacturing flaws as very precise lengths of microstrip line are required for correct phase shifts and even the slightest errors have a significant effect on the performance.

In addition, the measured phase is evaluated as a function of x at 73.5 GHz and compared to the simulated results. Figure 39 shows the measured and simulated phase response as a function of x. The measured response has fewer evaluation points than the simulated response but still a similar linear correlation behaviour can be seen, although the measured points are more scattered. This is again thought to be mainly caused by the uncertainties of the manufacturing process.

For the beam-steering demonstration, several PCBs for the phased array are manufactured. Each board has different configuration of fixed phase shifters so that the antenna beam can be controlled. The measured and simulated antenna patterns

with different phase shifter configurations are out of the scope of this thesis, but can be found in [15].

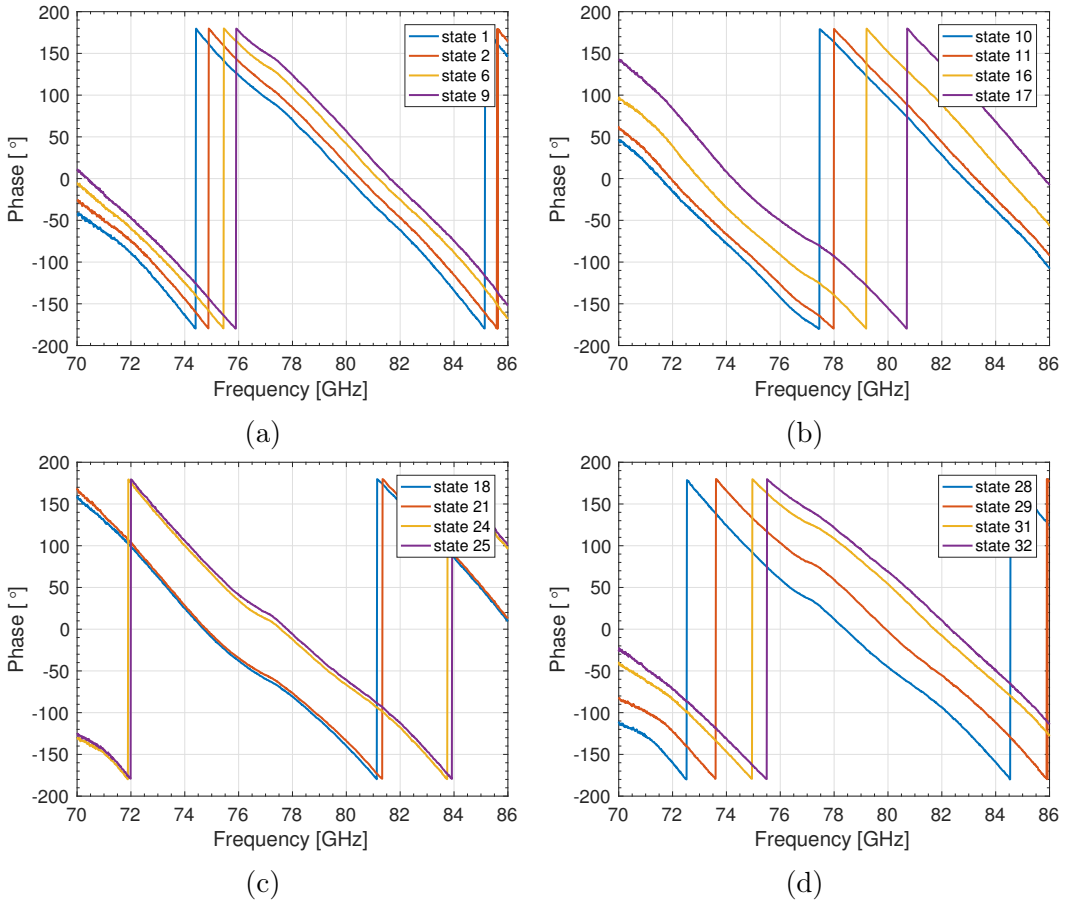

Figure 38: Measured phase response of the E-band phase shifter for states (a) 1, 2, 6, 9, (b) 10, 11, 16, 17, (c) 18, 21, 24, 25, and (d) 28, 29, 31, and 32.

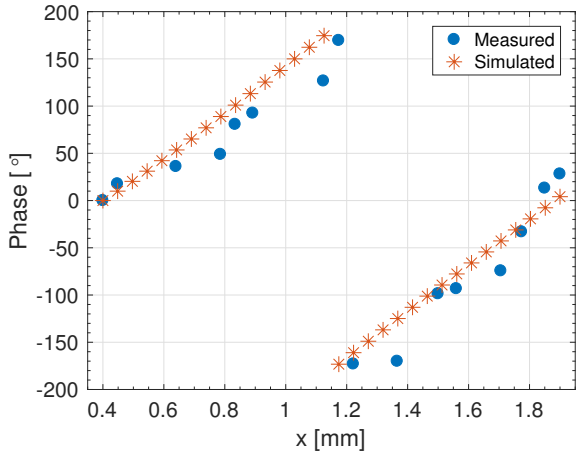

Figure 39: Measured and simulated phase response as a function of x at 73.5 GHz.

4.2 Cm-band Phase Shifter Characterization

Phase shifter is experimentally characterized by attaching it on a particular test bed, which has necessary coaxial connectors for RF-input and -output and pins for supply- and control-voltage lines. Furthermore, the intention is to build a simulation model of the test structure. The final model of the phase shifter is then made by comparing the simulated and measured results. This model can be then utilized to further optimize the transition for the cm-band.

Nokia Bell Labs had also manufactured their own test structure, later on referred to as a NBL (Nokia Bell Labs) board, to characterize the phase shifter. The test board is measured and simulated at Aalto University to ensure the phase shifter performance and to duplicate the measurements done by the Nokia Bell Labs.

This section first describes the used phase shifter and its characteristics according to the manufacturer. Then, the simulation model of the phase shifter is presented along with the designed test structures. After that, the measured test structure results are presented. Finally, the simulated and measured results of the NBL board are shown.

The S-parameter measurements in this section are done using Keysight PNA Vector Network Analyzer. A pair of 2.4-mm coaxial cables is used to connect the test structures to the network analyzer. A pair of 2.4-mm coaxial end-launch connectors from Southwest Microwave are utilized to feed the RF-signal in the test structures. As some of the measurements are done to find out the transmission phase response of the tested device, proper handling of the measurement cables is important. During the calibration, the cables are attached close to their final positions in the measurements, and during the measurements, they should not be touched. This reduces the possible phase errors in the measurements caused by the coaxial cable movement.

4.2.1 Cm-band Phase Shifter Overview

The phase shifter for cm-band is chosen to be TGP2100 from TriQuint [76]. The digital 5-bit phase shifter is reported to have 360° phase range. The 5-bit operation further indicates that the phase shifter resolution is 11.25° and 32 different states are required to cover full tuning range. Similarly to the E-band phase shifter, the first state is a reference state for which no phase shift is applied.

Figure 40 presents the phase shifter structure. The outer dimensions of the phase shifter are 1.88 x 0.75 mm^2 and the chip is 0.1 mm thick. The input and output pads for the RF-signal locate at the short ends of the chip. The phase shifter is supplied with a 5-V DC-voltage and the supply voltage input pad is located on the long side of the chip. The degree of the phase shift is controlled through five pads, which are fed with 5-V DC-voltages. These pads are located on the other long side of the chip. The RF- and DC-grounds of the phase shifter locate on the bottom of the component [77]. Due to this, the phase shifter must be attached either to the pad connected to the PCB ground with vias or directly to the ground plane. The RF-signal lines, and supply- and control-voltage lines are connected to the phase shifter with wire bonding and its effects to the phase shifter performance are discussed later on.

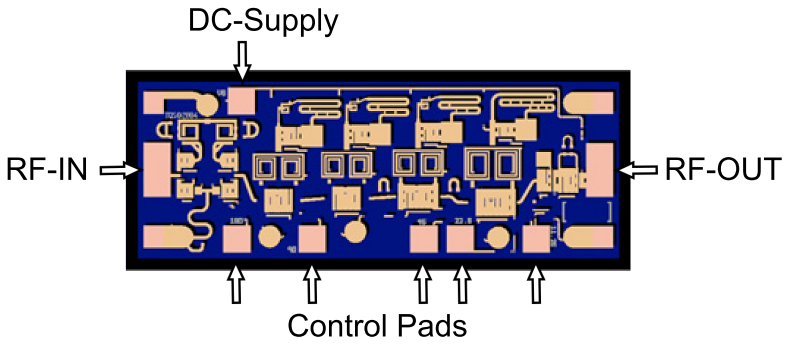

Figure 40: Picture of TGP2100 adapted from [76].

TGP2100 is optimized to operate at 28–32 GHz frequency range, but it can perform also at lower frequencies so that the whole cm-band (26–30 GHz) is covered. However, the insertion loss and the phase error are presumed to increase outside the specified range. The phase shifter characteristics are discussed in more detail in [76], and the S-parameters utilized in the following simulations can be found in [78].

4.2.2 Cm-band Phase Shifter Simulations

TriQuint provides S-parameters, which they have measured, for the phase shifter. Based on the e-mail conversation with the TriQuint representatives [77], the S-parameters are referenced to the RF-pads of the phase shifter, i.e. they do not take into account the effect of the wire bonding. Therefore, the influence of the bond wires, which are used to connect the phase shifter RF-pads to the RF-signal lines, must be simulated and researched. Figure 41 shows the reflection coefficient and the transmission coefficient of TGP2100 for few chosen states based on the reported S-parameters. The chosen states are the same used to describe E-band phase shifters as they cover the whole phase tuning range and thus, give a comprehensive presentation of the phase shifter performance.

Figure 41a shows how the matching deteriorates at the lower frequencies of the cm-band right outside the specified operation range. However, as seen in Figure 41b, the phase shifter transmission coefficient is also very low at the optimized range, less than -6 dB. Additionally, even more losses are predicted from the wire bonding, and thus, the total losses will be quite high.

Figure 41c describes phase response of the phase shifter transmission coefficient. The phase shift between different states remains virtually unchanged across the whole cm-band. Furthermore, the phase delay increases almost linearly with the state index of the phase shifter at 28 GHz frequency (41d), although some minor variation can be seen.

The cm-transition structure is simulated in Section 3.3 where the phase shifter

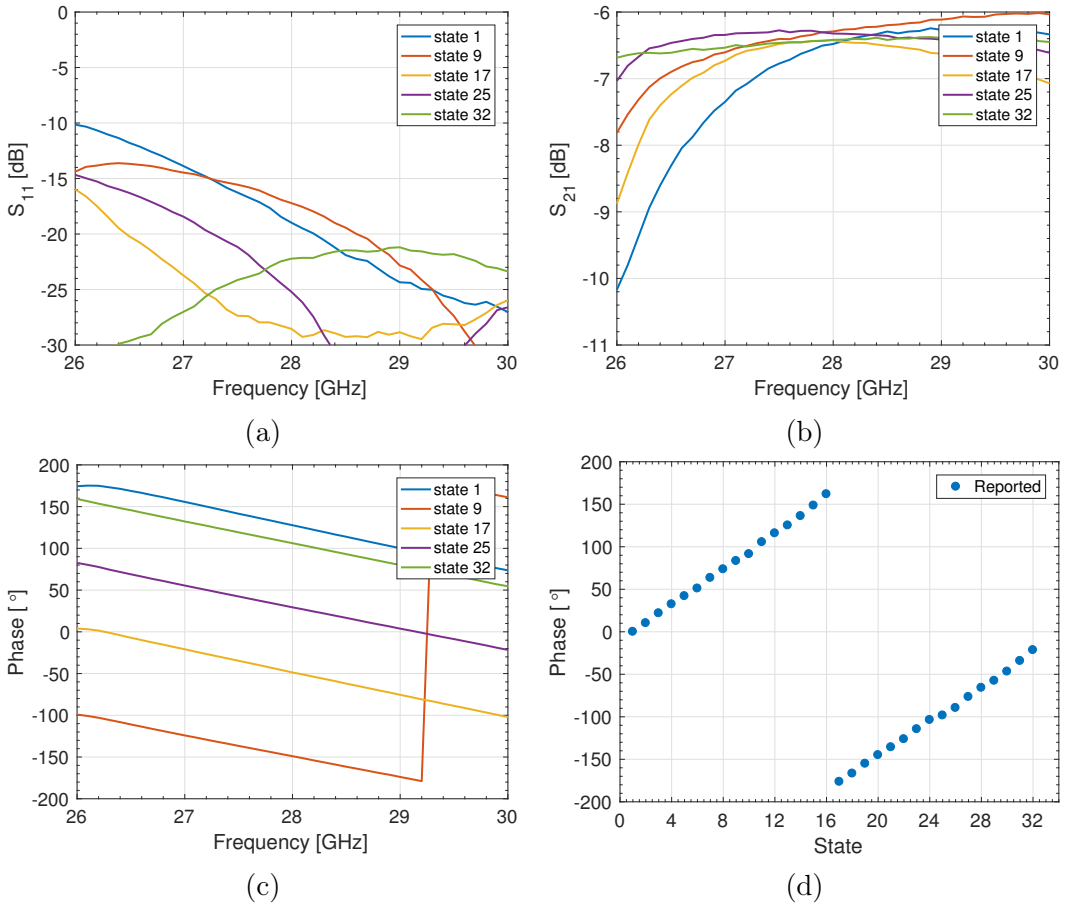

Figure 41: Reported S-parameters of TGP2100: (a) reflection coefficient, (b) transmission coefficient, (c) transmission coefficient phase, and (d) transmission coefficient phase for different states at 28 GHz [78].

is replaced with a straight microstrip line. To see how the phase shifter affects the overall transition performance, the transition simulation is updated. The simulated reflection coefficient, transmission coefficient, and the phase response of the transition with TGP2100 are presented in Figure 42. The influence of the bond wires is neglected in the following simulations such that the TGP2100 S-parameter representation, which neglects the effect of the bond wires, is directly connected to the microstrip line ends in the simulator.

Simulation results show that the main losses in the transition will be due to the phase shifters. As expected, the main losses in the phased array system are caused by the phase shifters because the feeding network has high efficiency. Furthermore, the results indicate that the additional matching network between the microstrip and the phase shifter might not actually improve the matching level at the frequencies above 28 GHz. The matching could be improved at the lower frequencies, although this would necessitate a matching network, which might be difficult to fit in the limited space. Before such design is considered, the measurement results should be acquired to back up the simulation results. To confirm that the real phase shifters

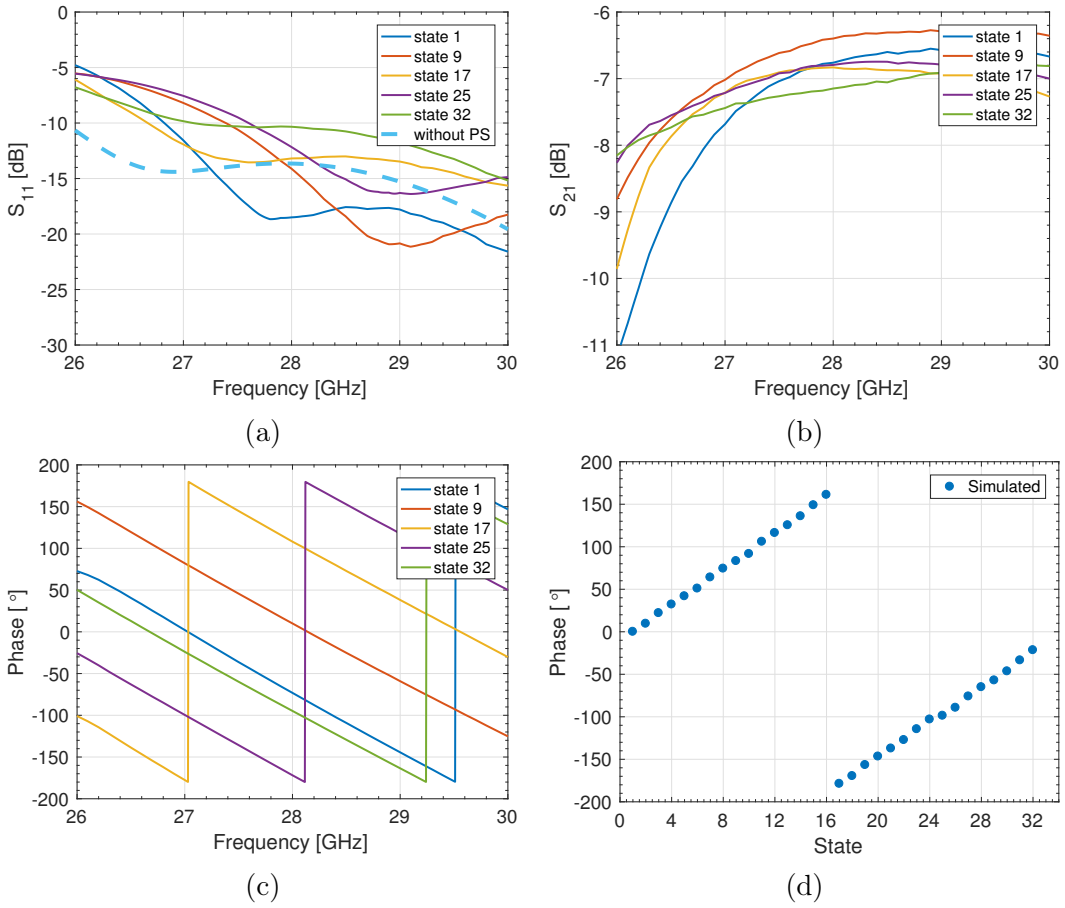

Figure 42: Simulated results of the transition structure with TGP2100 phase shifter: (a) reflection coefficient, (b) transmission coefficient, (c) transmission coefficient phase, and (d) transmission coefficient phase for different states at 28 GHz.

behave as simulated, the test structures for their measurement are fabricated and described in detail in the following section.

4.2.3 Cm-band Phase Shifter Measurements

The following test structures are fabricated and measured for the phase shifter and the wire bonding characterization:

- Test structure with integrated phase shifter and the supply and control lines.
- Microstrip lines that are connected to each other with wire bonding.
- Straight microstrip line as a reference.

First the phase shifter test structure is discussed. In the early stages of the test structure design, the phase shifter grounding proved to be a somewhat challenging problem. By examining the TGP2100 data sheet, the grounding structures were not clearly defined and at first the two pads next to the RF-signal input and output were thought to be RF-ground pads as the structure resembled that of a coplanar

waveguide. The bottom side of the phase shifter was falsely thought to be only DC-ground. So, in the early test structure designs there was a pad for DC-grounding but it was not properly connected to the RF-ground, thus making the measurements with these test structures impractical. When the issue with the phase shifter ground was solved, a new test structure was designed.

The structure is designed to mirror the final phase shifter integration plan as accurately as possible. As presented in Figure 43, in the test structure a cavity is milled on the substrate for the phase shifter. This way the phase shifter can be directly mounted to the ground plane. The milling procedure has to be highly accurate as well to uncover the metal layer as the substrate is only 127 µm thin and the metal layer even thinner (50 µm in the proposed PCB structure at the cm-band, 18 µm in the test structure). The milling for the test structure is done at the premises of the Aalto University and the old unused test structures have been utilized to find out that the cavity can be fabricated with adequate precision.

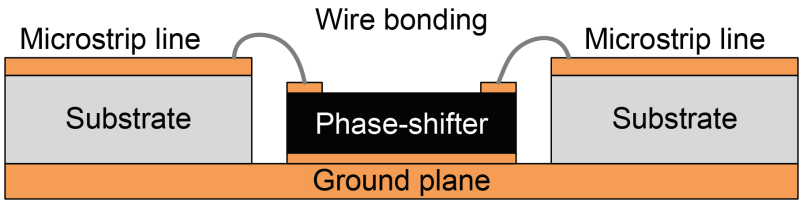

Figure 43: Cross-cut of the new test structure with a cavity for the phase shifter.

The final test structure is designed in the Mentor Graphics PADS PCB Design Software. Figure 44 presents the fabricated test structure without the phase shifter and a close-up of the wire-bonded phase shifter. The RF-signals are transmitted through 0.34-mm wide microstrip lines while 0.15-mm wide lines are used for the supply and control voltages. A 2.10 x 0.95 mm^2 area is allocated in the middle of the board for the phase shifter mounting, and the area is decided to be a bit larger than the actual phase shifter so the integration of the chip is not restricted by the board.

To minimize the losses and to ensure that the wire bonding works as intended, the distances between TGP2100 I/O-pads and the corresponding microstrip lines on the PCB board are minimized. In the optimal case, the phase shifter is properly attached exactly in the middle of the milled cavity, and the distance from the I/O-pad to the microstrip line is 330 µm. However, as seen in Figure 44b, the cavity in the test structure is not exactly in the middle of the board and the bond wire length in the input is a bit longer than anticipated. Nevertheless, this is not a significant error and as the final PCB for the phased array is ordered from the specialised manufacturer, the cavity will be placed accurately where it is supposed to be.

The positions of the supply- and control-voltage lines on the PCB board are thought to be less crucial as the DC-performance is not considerably affected by the length of the bond wire. In the optimal case, the distance from pad to line is about 700 µm. Additionally, the control-voltage lines are not aligned with the corresponding pads on the phase shifter as a 150-µm distance is required to be left between each line due to manufacturing constraints. However, this only has to

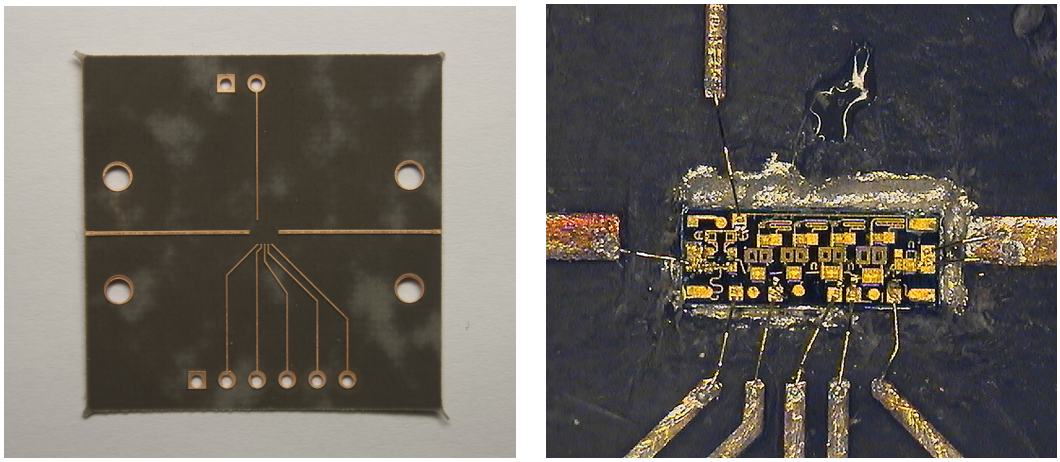

(a) (b)

Figure 44: (a) Fabricated phase shifter test structure and (b) wire-bonded phase shifter in the same structure.

be considered in the practical realization and it does not affect the phase shifter controlling.

The test structures are fabricated on a 127-µm thick RT/duroid 5880 board with a 18-µm thick copper coating on both sides. The RF-signal is measured with two 2.4-mm coaxial end-launch connectors and the supply and control voltages are connected to the board with pin connectors. No additional substrate cores or metal layers are attached to the board to ensure the connection of the end-launch connectors to the RF-ground. However, the board is too thin to support the connectors and therefore a separate steel plate is placed under the substrate board to reinforce it.

Two phase shifters were attached to the test boards at Aalto University and the process required heating up the substrate board. During the process, the board started to bend due to the increasing temperature, which was thought to be caused by the different thermal expansion coefficients of the PTFE-based substrate and the metallic ground layer. However, the attachment was still successful and the test boards with phase shifters were sent to VTT Oulu, for wire bonding. Yet other problems arose. First, the phase shifters were not mounted well enough for the wire bonding and therefore, had to be removed, cleaned, and reattached to the board. Then the substrate bending caused problems to the wire bonding. While connecting the next wire, the previously connected bond wire came loose because the substrate bended under the pressure from the wire bonding tool. To prevent this, a conductive glue was used to ensure that the bond wires stay connected. In the end, only the other phase shifter test board was successfully wire bonded. However, when this test structure was measured back at Aalto University, it turned out to be malfunctional.

The phase shifter could have been malfunctional because of unsuccessful wire bonding, or the phase shifter chip may have been broken during the excessive attachment process. To prevent this from happening with the phased-array PCB, the phase shifters are chosen to be integrated by VTT Oulu since they know how to take into account the requirements of the wire bonding. Furthermore, the final PCB

structure is thicker than the test structure and therefore, more rigid. Thus, it is assumed that the heating will not have similar harmful effect on the PCB structure and the wire bonding.

Although the phase shifter test structure proved to be a failure, the test structures for the evaluation of the wire bonding were successfully fabricated. Figure 45 shows the test board design where 470-µm gap in a straight microstrip line is crossed with two bond wires. The reflection and transmission coefficients of the structure are measured. The results are compared to those of a straight, intact microstrip line section of the same length to find out the insertion loss caused by the bond wires.

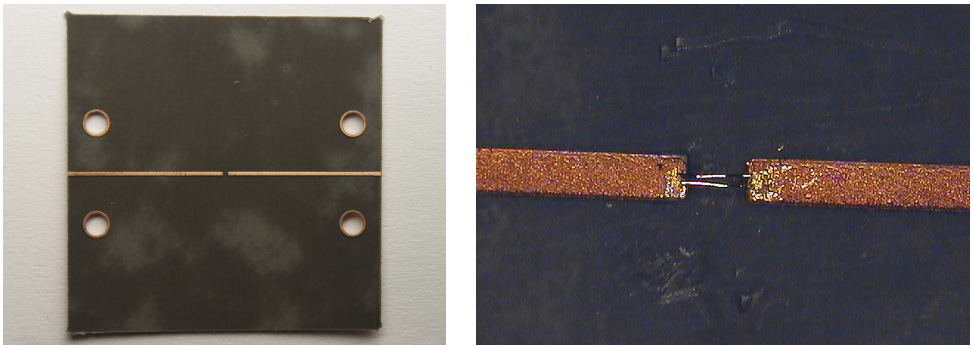

(a) (b)

Figure 45: (a) Overview of the fabricated test structure and (b) closeup of the wire-bonded gap.

Figure 46 presents the reflections and transmissions of the wire-bonded microstrip line and the straight microstrip line. The reflection coefficients of both structures are quite high and the mismatch is caused by the end-launch connectors. This can be seen from the results of the straight microstrip line in Figure 46a.

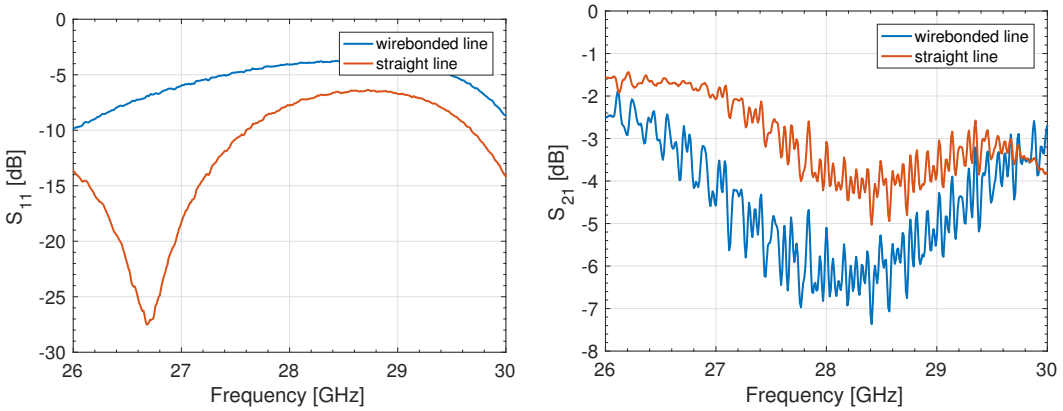

(a) (b)

Figure 46: Measurement results of the straight microstrip line and the wire-bonded microstrip line: (a) reflection coefficient and (b) transmission coefficient.

The reflection is well matched in approximately 4 GHz periods which indicates that the propagating wave is reflected back 26 mm away from the source, when

taking into account the effective relative permittivity of the microstrip line. The distance of 26 mm is approximately the distance between the end-launch connectors and therefore, the source of reflections.

The transmission coefficient results are evaluated to find out the losses of the wire bonding. Figure 46b shows that these losses are about 2 dB when two bond wires are used in a single connection. The phase shifter input and output are both wire bonded with two wires, and therefore, a total loss of about 4 dB is expected to show in the final structure.

4.2.4 Simulations and Measurements of the NBL board

Nokia Bell Labs manufactured their own test structure for the phase shifter measurements [79]. The manufactured test structure is a multilayer PCB board that has a 0.254-mm thick RO4350B ($\varepsilon_r = 3.66$) as a substrate. The substrate is backed by a 0.18-mm thick prepreg layer and a 0.7-mm thick FR4 layer. The copper metal foil is 18 µm thick with gold plating. The outer dimensions of the board are 20 x 20 mm^2. The phase shifter is attached into the middle of the board and it is wire bonded to the board by Nokia Bell Labs. A two-pin connector is used for the phase shifter supply and a six-pin connector is used for the control voltages. In both pin-connectors, one of the pins is connected to the ground plane while the others are fed with 5-V DC-voltages. The phase shift is further controlled by a separate control board in which the control voltages are turned on/off according to the desired phase state. The RF-signal is measured through two 2.4-mm coaxial end-launch connectors. Figure 47 shows the NBL board with the connectors.

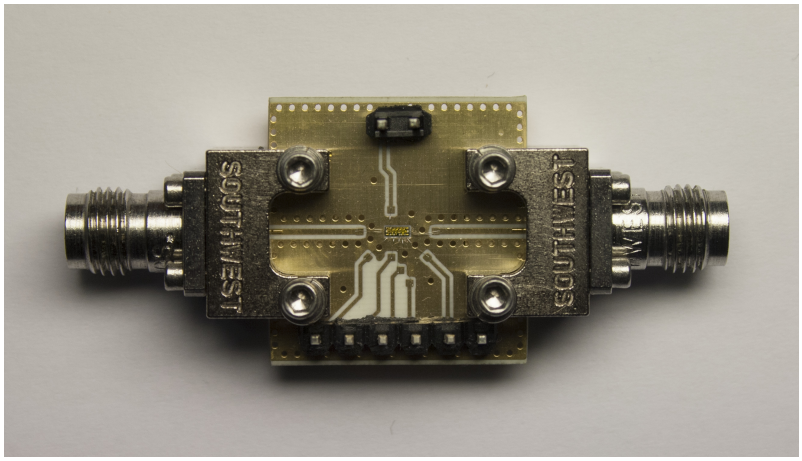

Figure 47: NBL board with the end-launch connectors on the side. The supply-voltage pins are on the top and the control-voltage pins are on the bottom.

Figure 48 shows the measurement setup. The test board is supplied by the HM7042-3 power supply with 5-V DC-voltage. The phase shifter is controlled with a specially made control board which is mechanically operated to switch the state of the phase shifter. All the 32 different states are measured during the testing.

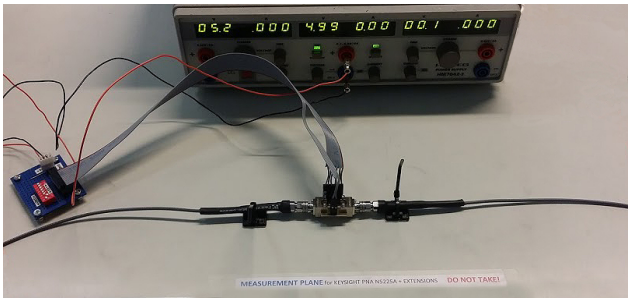

Figure 48: Measurement setup of the NBL board. The test board is connected to a VNA through coaxial cables and controlled with a blue control board on the left. HM7042-3 on the top supplies the control board with 5-V supply voltage.

The measured results of the reflection and the transmission coefficients are presented in Figure 49. Yet again, the results for the phase shifter states 1, 9, 17, 25, and 32 are discussed. The measured results are substantially worse than anticipated based on the initial TGP2100 simulations. The matching in all states is poor and the transmission coefficient magnitude change between different states does not appear to follow any clear pattern. Furthermore, the phase shifts are not what expected as shown in Figure 49d: the phase shift between the different states at 28 GHz is not linear and only 150° tuning range is achieved.

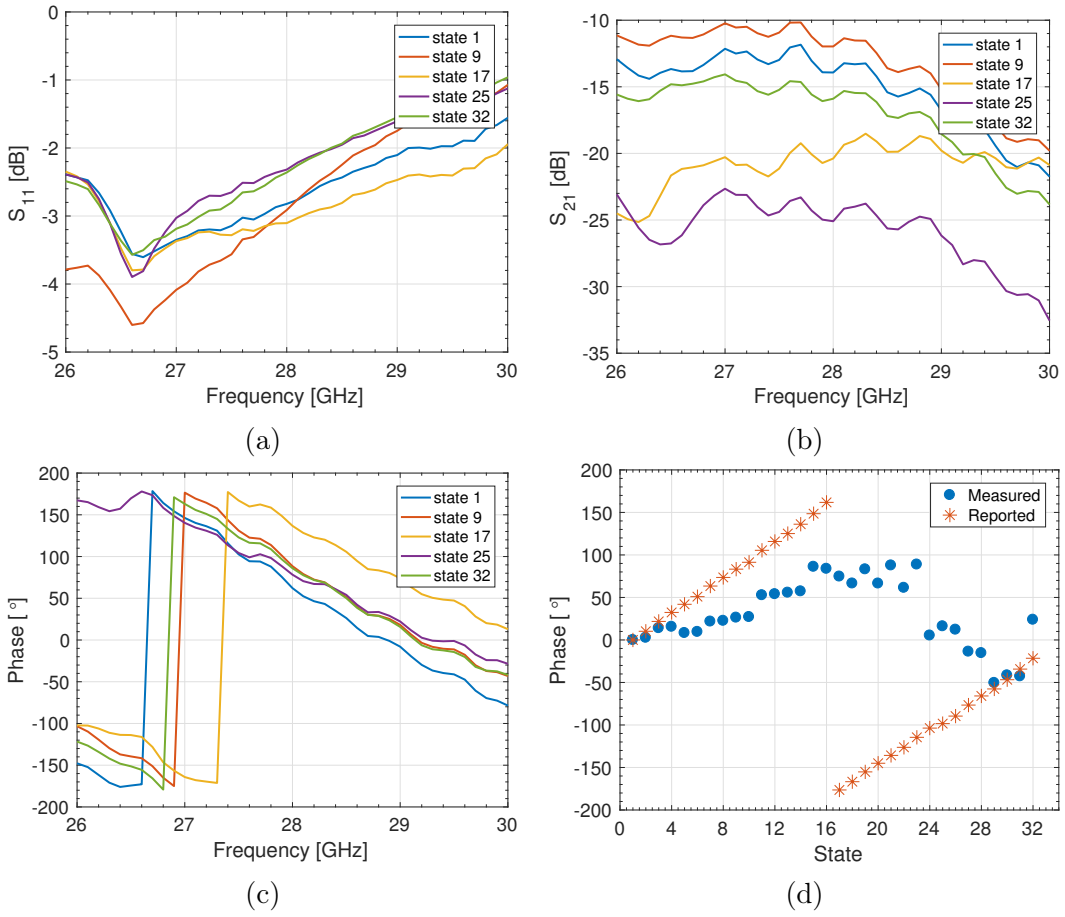

Figure 49: Measured results of the NBL board: (a) reflection coefficient, (b) transmission coefficient, (c) transmission coefficient phase, and (d) transmission coefficient phase for different states at 28 GHz.

A review of the NBL test structure indicates that the RF-ground connection of the phase shifter is defected, which would explain the poor performance. However, a simulation model is still fabricated with aspiration to understand the phase shifter operation better and to validate the measured results.

The simulation model of the NBL board shown in Figure 50 is based on the PADS-model which was used to fabricate the actual board. This way the simulation model is highly realistic. Nevertheless, the connectors, the wire-bonded connections to the supply and control pads, and the DC-voltages are not modelled in the simulations. Especially the DC-voltages are omitted, as the internal operation or connections of the phase shifter are not known.

The phase shifter is modelled as a block of GaAs with a layer of PEC on the bottom representing the phase shifter ground. The outer dimensions of the modelled block are similar to the real component. On the top of the GaAs block, two pads of PEC represent the RF input and output pads. The bond wires are also modelled from the microstrip lines to the pads as PEC wires with the diameter of 25 µm. The mesh grid is made dense enough through the whole structure, particularly near the bond wires so they are simulated correctly.

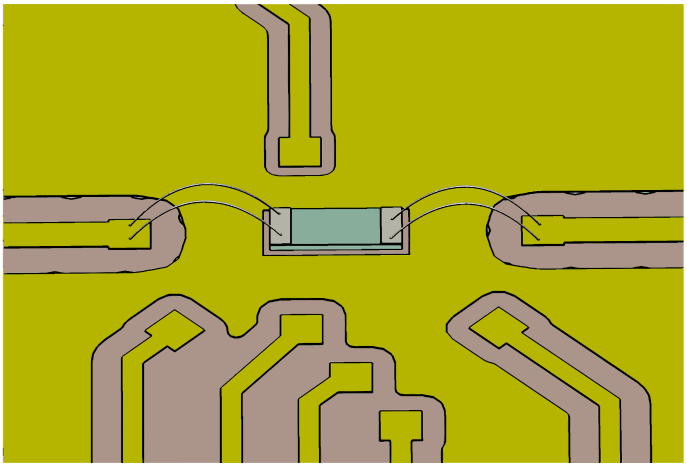

Figure 50: NBL board simulation model.

The phase shifter is a 2-port device and the S-parameter file from the manufacturer is used to represent the functionality of the device. In the simulations, the S-parameter file of the chosen state is connected between the two discrete ports that are placed on both sides of the modelled phase shifter. The positioning of the discrete ports is important: the results depend highly on where they are located.

The phase shifter is not connected to the NBL board ground well, which causes the component to be floating in the RF-sense. The reason might be that the silver epoxy used to glue the component on the PCB from the bottom side is not providing good RF-connection. To simulate this, the discrete ports are first connected between the RF-pads and the phase shifter ground plane as presented in Figure 51a. For comparison, another port configuration is simulated and shown in Figure 51b. This second configuration describes the phase shifter operation when connected to the RF-ground.

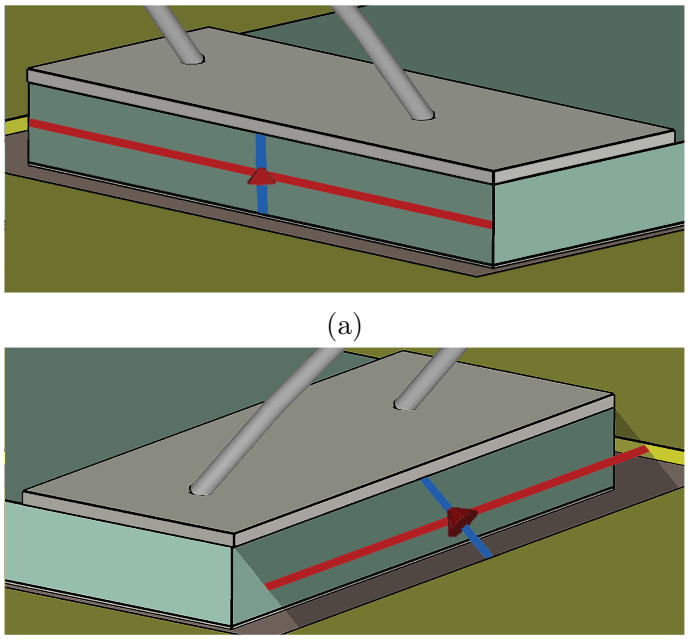

(a)

(b)

Figure 51: Simulation model of the NBL board with (a) discrete port in a phase shifter model, i.e. floating and (b) port connected between the global ground plane and the phase shifter model.

The simulated reflection and transmission coefficients of both simulation configurations are shown in Figure 52. Neither of the simulation configurations has similar results as the measured test board. The simulated results show that the phase shifter should not work in practice, if the phase shifter ground is not properly connected to the PCB ground. On the other hand, even if the ground connection is established, the NBL board would not cover the whole cm-band, since the structure is well-matched only at 27.5 GHz frequency. Furthermore, the measured state 9 transmission coefficient result is a bit similar with the simulated ones. With the other states, the the transmission coefficient trend is somewhat similar, but level in measurements is much lower.

As the measured phase shifter performance is somewhere between the two simulated case, it is concluded that the phase shifter model is inadequate. The phase shifter is modeled only as a GaAs block and the internal electric connections between the RF-input and -output are not considered. Based on this, the RF-signal is most likely transmitted through the phase shifter by unknown means, and thus, the measured results do not correlate with the simulations.

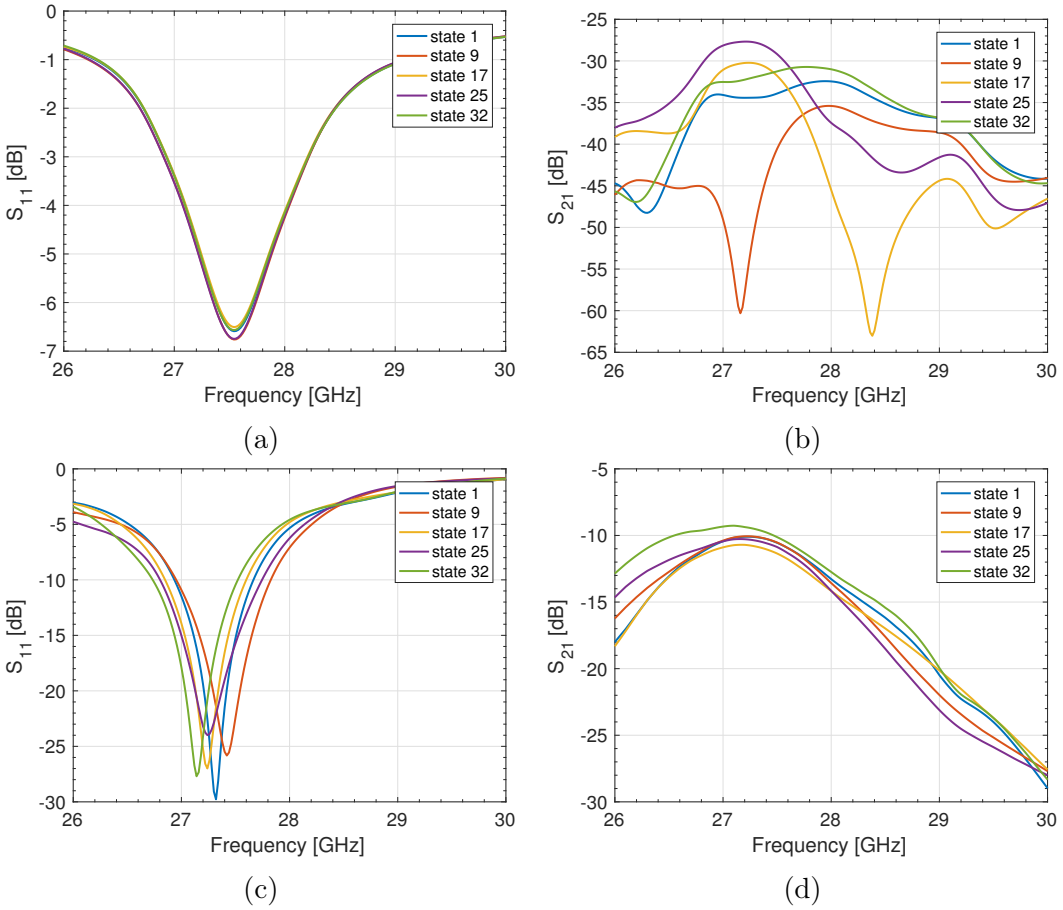

Figure 52: Simulated results of the NBL board with floating ports: (a) reflection coefficient and (b) transmission coefficient. Simulated results of the NBL board with ports connected to the ground: (c) reflection coefficient and (d) transmission coefficient.

4.3 Summary of the E-band and Cm-band Phase Shifter Characterization

The designed E-band fixed phase shifters are simulated, fabricated, and measured. In [15] it is described how the beam-steering can be done with these phase shifters and they fulfill their role in the proof of concept design. Thus, the proposed phased array concept is feasible for E-band but the electrical beam-steering is not yet available. For E-band, electrically tunable phase shifters are still required and they should be preferably digitally controlled. However, the available space between the transitions restricts the phase shifter outer dimensions strictly. The used phase shifter technologies and types determine mainly the phase shifter performance but the packaging can be as important feature to take into account as shown with the cm-band phase shifter.

The cm-band phase shifter is simulated and test structures are fabricated but the measurements of the phase shifter are not successful due to the test boards failure to operate. It is mainly because the wire bonding of TGP2100 has proven to be quite difficult and also relatively lossy. The failure in the cm-band phase shifter measurements shows that the packaging of the phase shifter should be chosen carefully, possibly in a way the phase shifter integration is facile and the connections are not vulnerable for the external disturbances. For example, the wire-bonded phase shifters could be packaged so that the packaging shields the bond wires during the phase shifter installation. Another possibility is to use flip-chip components instead of the ones requiring wire bonding.

The lessons learnt from the manufacturing mistakes in the test structure fabrication are taken into account in the final PCB design of the cm-band phased array. The phase shifter mounting in the cavity in particular must be done properly with respect to the wire bonding. In addition, the indium solder used at Aalto University to attach the chip to the board is not strong enough for proper connection and the chips should be attached better. As the PCB of the phased array is thicker than the one of the test boards, the bending caused by the heating should not be a problem, but it should still be considered in the process. Furthermore, the PCB is fabricated by the specific manufacturer, and thus, the cavities for phase shifter can be done with high precision. The next step is to fabricate the final PCB and the rest of the antenna array for measurements. Additionally, a separate PCB with straight microstrip lines instead of the phase shifters is manufactured to characterize the phase shifters further.

5 Summary and Conclusions

In this thesis, the integration of phase shifters in an antenna array that might suit for 5G base stations have been studied. This includes the phase shifter study at millimeter-wave frequencies, the design of the waveguide-to-PCB transitions, and the characterization of the phase shifters. The main objectives of the thesis are to design the transition structures for the E-band and cm-band antennas, and to understand the design requirements and challenges of the phase shifter integration for the proposed antenna prototypes.

The phase shifters are the key components in the phased arrays and their performance affects the antenna performance significantly. The phase switching time has to be fast, since the 5G base stations require high-speed beam-steering. Furthermore, as the number of the base stations is increased, the power consumption of the single station should be low not to increase the total power consumption dramatically. Thus, the insertion loss of the phase shifter must be minimized, since it being the main cause of the total losses in phased arrays along with the feeding network losses.

The phase shifters are categorized in several ways, and this thesis discusses mainly the different phase shifter types and their manufacturing technologies. The main focus is on researching the phase shifters that can have planar mounting on PCB. The phase shifts are traditionally controlled by microwave switches or tunable varactors, depending on the phase shifter type. The MMIC-based phase shifters are used most commonly. However, at the higher millimeter-wave frequencies, they tend to have high losses and degraded performance. MEMS-based phase shifters have generally much lower insertion losses, but they are often considered slow and unreliable for 5G antenna applications. Of the other manufacturing technologies, the ferroelectric phase shifters are still far from being commercialized and the ferrite-based phase shifters are physically large and power consuming, therefore they are not suitable for proposed antenna structure.

No phase shifter type has any clear advantages compared to the others, although the digital control is preferable over analog one. Furthermore, most of the reported phase shifters are passive, while active shifters may offer lower insertion loss at the expense of increased power consumption. However, the heat transfer due to power dissipation must be taken into account with active phase shifters, which affects the integration design.

The waveguide-to-PCB transitions are designed for both frequency bands. The propagating wave is coupled between the waveguide and the microstrip probe, since the microstrip line is used on the PCB. The waveguides are tapered to make more space for the phase shifter and the PCB is specially designed to improve the transition efficiency. The length of the microstrip inside the waveguide and the microstrip distance from the shorted end of the waveguide are the most important parameters in the transition optimizing. A sensitivity analysis of these parameters is presented. It suggests the microstrip distance from the shorted end can be chosen more freely, while the microstrip distance inside the waveguide must not vary from the optimized value more than ± 30 µm at E-band and ± 50 µm at cm-band.

The designed transitions have good simulated performance and they are suitable for the base station prototypes. The combined E-band transitions have 0.7 dB insertion loss across the 71–86 GHz band, and the reflections are less than −12 dB. The cm-band transitions has 0.35-dB insertion loss across the 26–30 GHz band, and the reflections are less than −12 dB. The transitions can be further improved by removing the extra substrate inside the waveguide and improving the microstrip line probe design. However, the available space for the phase shifter is limited and large phase shifter designs including the matching networks are not applicable.

Commercial phase shifters are not found for the E-band antenna, therefore they are self-designed. E-band phase shifters are fixed microstrip line-based true time delay phase shifters. The designed structures are fabricated and measured, and the measured phase response is similar to the simulated one. The phase shifters are suitable for the proof-of-concept design to demonstrate the beam-steering of the E-band antenna prototype.

TGP2100 phase shifter from TriQuint is chosen for cm-band, since it is the only commercial phase shifter supporting integration on the planar transmission line. The RF- and DC-signals are connected to the device with bond wires and a special cavity is made on PCB for the phase shifter attachment. A test structure is made to characterize the cm-band phase shifter, but the measurement results are not valid, as the test board is malfunctional. It is unclear whether the problem is in wire bonding or if the phase shifter chip has been damaged during the installation. Nevertheless, the cm-band phase shifters are simulated as a part of the cm-band transition structure showing that TGP2100 is suitable for the cm-band antenna prototype. Other test structures are fabricated and measured to find out the losses due to wire bonding, because the transmission losses of the final antenna are caused mainly by insertion losses of the phase shifter and the wire bonding.

Nokia Bell Labs manufactured their own test structure (NBL board), which is simulated and measured. However, it is detected that the RF-ground connection of the phase shifter is defected. The component was glued with silver epoxy to the PCB and therefore, it should be well connected. It is concluded, that the silver epoxy might not be suited to provide the connection to the RF-ground. The effect of the grounding is then evaluated with different simulations.

The lessons learned from the manufacturing mistakes of the cm-band test structure are taken into account to produce a working PCB design with phase shifters properly installed. The bond wires are mechanically vulnerable and they must be handled with care during the integration. Another possibility is to utilize flip-chip components instead of the ones requiring wire bonding or use packaging to shield the bond wires.

To summarize the thesis, the phase shifter integration designs for the 5G base station antenna prototypes are presented. The designed structures are made for E-band and cm-band and they are suitable to be installed in the antennas for the beam-steering demonstration. Future work includes finalizing the cm-band PCB design and integrating phase shifters on it, and after that, the cm-band antenna prototype fabrication and its measurements. Additionally, the phase shifters will be characterized further to develop a more extensive simulation model of the device.

References

[1] Cisco, *Cisco VNI forecast and methodology, 2015-2020*, accessed January 2017. [Online]. Available: http://www.cisco.com/c/en/us/solutions/collateral/service-provider/visual-networking-index-vni/complete-white-paper-c11-481360.html.

[2] M. Agiwal, A. Roy, and N. Saxena, "Next generation 5G wireless networks: A comprehensive survey," *IEEE Communications Surveys Tutorials*, vol. 18, no. 3, pp. 1617–1655, Feb. 2016.

[3] Nokia, *looking ahead to 5G*, accessed January 2017. [Online]. Available: https://networks.nokia.com/sites/default/files/document/5g_white_paper_0.pdf.

[4] Huawei, *5G radio access*, accessed January 2017. [Online]. Available: https://www.ericsson.com/res/docs/whitepapers/wp-5g.pdf.

[5] Ericsson, *From today to tomorrow, huawei microwave & mm-wave whitepaper*, accessed January 2017. [Online]. Available: http://www-file.huawei.com/~/media/CORPORATE/PDF/white%5C%20paper/huawei%5C%20microwave%5C%20whitepaper-2016.pdf.

[6] J. G. Andrews, S. Buzzi, W. Choi, S. V. Hanly, A. Lozano, A. C. K. Soong, and J. C. Zhang, "What will 5G be?" *IEEE Journal on Selected Areas in Communications*, vol. 32, no. 6, pp. 1065–1082, Jun. 2014.

[7] M. Shariat, M. Dianati, K. Seppänen, T. Suihko, J. Putkonen, and V. Frascolla, "Enabling wireless backhauling for next generation mmwave networks," in *2015 European Conference on Networks and Communications (EuCNC)*, Jun. 2015, pp. 164–168.

[8] A. F. Molisch, *Wireless Communications*, 2nd ed. Chichester, United Kingdom: Wiley, 2011, 827 pages.

[9] J. Ala-Laurinaho, J. Aurinsalo, A. Karttunen, M. Kaunisto, A. Lamminen, J. Nurmiharju, A. V. Räisänen, J. Säily, and P. Wainio, "2-D beam-steerable integrated lens antenna system for 5G E-band access and backhaul," *IEEE Transactions on Microwave Theory and Techniques*, vol. 64, no. 7, pp. 2244–2255, Jul. 2016.

[10] J. Säily, M. Pokorný, M. Kaunisto, A. Lamminen, J. Aurinsalo, and Z. Raida, "Millimetre-wave beam-switching rotman lens antenna designs on multi-layered LCP substrates," in *2016 10th European Conference on Antennas and Propagation (EuCAP)*, Apr. 2016, pp. 1–5.

[11] T. Zvolensky, D. Chicherin, A. V. Räisänen, and C. Simovski, "Leaky-wave antenna based on microelectromechanical systems-loaded microstrip line," *IET Microwaves, Antennas Propagation*, vol. 5, no. 3, pp. 357–363, Feb. 2011.

[12] K. K. Karnati, M. E. Trampler, and X. Gong, "A monolithically BST-integrated Ka-band beamsteerable reflectarray antenna," *IEEE Transactions on Antennas and Propagation*, vol. 65, no. 1, pp. 159–166, Jan. 2017.

[13] N. Ojaroudiparchin, M. Shen, and G. F. Pedersen, "8x8 planar phased array antenna with high efficiency and insensitivity properties for 5G mobile base stations," in *2016 10th European Conference on Antennas and Propagation (EuCAP)*, Apr. 2016, pp. 1–5.

[14] T. Sehm, "Mm-wave phase shifters and switches," Doctoral dissertation, Radio Laboratory, Helsinki University of Technology, Espoo, Finland, Feb. 2000.

[15] M. M. Islam, R. Luomaniemi, M. K. Leino, J. Song, R. Valkonen, J. Ala-Laurinaho, and V. Viikari, "E-band beam-steerable and scalable phase antenna array," unpublished.

[16] R. Montoya Moreno, "Beam steerable 26 – 30 GHz antenna for a fifth generation cellular base station," Master's thesis, RAD Department, Aalto University, Helsinki, Finland, 2016, p. 66.

[17] W. L. Stutzman, *Antenna Theory and Design*, 3rd ed. Hoboken, NJ, USA: John Wiley & Sons, 2011, 822 pages.

[18] C. A. Balanis, *Antenna Theory : Analysis and Design*, 3rd ed. Hoboken, NJ, USA: John Wiley & Sons, 2005, 1117 pages.

[19] R. J. Mailloux, *Phased Array Antenna Handbook*. Boston, MA, USA: Artech House, 1994, 536 pages.

[20] A. Räisänen and A. Lehto, *Radiotekniikan perusteet*, in Finnish, 13th ed. Helsinki, Finland: Otatieto, 2011, 286 pages.

[21] D. M. Pozar, *Microwave Engineering*, 4th ed. Hoboken, NJ, USA: John Wiley & Sons, 2012, 732 pages.

[22] A. H. Sihvola and I. V. Lindell, *Sähkömagneettinen kenttäteoria. 2, Dynaamiset kentät*, in Finnish, 4th ed. Helsinki, Finland: Otatieto, 2004, 200 pages.

[23] A. Lehto and A. Räisänen, *Millimetriaaltotekniikka*, in Finnish, 2nd ed. Helsinki, Finland: Otatieto, 2002, 188 pages.

[24] A. Lehto and A. Räisänen, *RF-ja mikroaaltotekniikka*, in Finnish, 8th ed. Helsinki, Finland: Otatieto, 2006, 271 pages.

[25] I. V. Lindell, *Aaltojohtoteoria*, in Finnish, 2nd ed. Espoo, Finland: Otatieto, 1997, 345 pages.

[26] F. J. Tischer, "Experimental attenuation of rectangular waveguides at millimeter-wavelengths," in *Microwave Symposium Digest, 1977 IEEE MTT-S International*, Jun. 1977, pp. 492–494.

[27] D. Deslandes and K. Wu, "Integrated microstrip and rectangular waveguide in planar form," *IEEE Microwave and Wireless Components Letters*, vol. 11, no. 2, pp. 68–70, Feb. 2001.

[28] D. Deslandes and K. Wu, "Accurate modeling, wave mechanisms, and design considerations of a substrate integrated waveguide," *IEEE Transactions on Microwave Theory and Techniques*, vol. 54, no. 6, pp. 2516–2526, Jun. 2006.

[29] F. Xu and K. Wu, "Guided-wave and leakage characteristics of substrate integrated waveguide," *IEEE Transactions on Microwave Theory and Techniques*, vol. 53, no. 1, pp. 66–73, Jan. 2005.

[30] M. Pasian, M. Bozzi, and L. Perregrini, "A formula for radiation loss in substrate integrated waveguide," *IEEE Transactions on Microwave Theory and Techniques*, vol. 62, no. 10, pp. 2205–2213, Oct. 2014.

[31] E. Miralles, H. Esteban, C. Bachiller, A. Belenguer, and V. E. Boria, "Improvement for the design equations for tapered microstrip-to-substrate integrated waveguide transitions," in *2011 International Conference on Electromagnetics in Advanced Applications*, Sep. 2011, pp. 652–655.

[32] C. Rave and A. F. Jacob, "A design approach for tapered waveguide to substrate-integrated waveguide transitions," *IEEE Transactions on Microwave Theory and Techniques*, vol. 64, no. 8, pp. 2502–2510, Aug. 2016.

[33] Z. Kordiboroujeni and J. Bornemann, "Efficient design of substrate integrated waveguide power dividers for antenna feed systems," in *2013 7th European Conference on Antennas and Propagation (EuCAP)*, Apr. 2013, pp. 352–356.

[34] F. Parment, A. Ghiotto, T. P. Vuong, J. M. Duchamp, and K. Wu, "Double dielectric slab-loaded air-filled SIW phase shifters for high-performance millimeter-wave integration," *IEEE Transactions on Microwave Theory and Techniques*, vol. 64, no. 9, pp. 2833–2842, Sep. 2016.

[35] M. Bozzi, A. Georgiadis, and K. Wu, "Review of substrate-integrated waveguide circuits and antennas," *IET Microwaves, Antennas Propagation*, vol. 5, no. 8, pp. 909–920, Jun. 2011.

[36] G. M. Rebeiz and G.-L. Tan, "MEMS phase shifters," in *RF MEMS*, G. M. Rebeiz, Ed. Hoboken, NJ, USA: John Wiley & Sons, 2003, ch. 9.

[37] R. R. Romanofsky, "Array phase shifters: Theory and technology," in *Antenna Engineering Handbook*, J. L. Volakis, Ed., 4th ed. New York, NY, USA: McGraw-Hill, 2007, ch. 21.

[38] Y. Yu, P. Baltus, and A. van Roermund, *Integrated 60GHz RF Beamforming in CMOS*, ser. Analog Circuits and Signal Processing. Dordrecht, Netherlands: Springer, 2011, 118 pages.

[39] K. Maruhashi, H. Mizutani, and K. Ohata, "Design and performance of a Ka-band monolithic phase shifter utilizing nonresonant FET switches," *IEEE Transactions on Microwave Theory and Techniques*, vol. 48, no. 8, pp. 1313–1317, Aug. 2000.

[40] P. Meineri, D. Dubuc, and K. Grenier, "Liquid-based tunable loaded-line phase shifter," in *2012 42nd European Microwave Conference (EuMC)*, Oct. 2012, pp. 719–722.

[41] F. Ellinger, H. Jackel, and W. Bachtold, "Varactor-loaded transmission-line phase shifter at C-band using lumped elements," *IEEE Transactions on Microwave Theory and Techniques*, vol. 51, no. 4, pp. 1135–1140, Apr. 2003.

[42] S. Shamsadini, S. Shamsinejad, P. Mousavi, and K. Moez, "Improved 60GHz loaded-line phase shifter using tunable inductor," in *2016 IEEE International Symposium on Antennas and Propagation (APSURSI)*, Jun. 2016, pp. 1141–1142.

[43] H. S. Lee and B. W. Min, "W-band CMOS 4-bit phase shifter for high power and phase compression points," *IEEE Transactions on Circuits and Systems II: Express Briefs*, vol. 62, no. 1, pp. 1–5, Jan. 2015.

[44] C. F. Campbell and S. A. Brown, "A compact 5-bit phase-shifter MMIC for K-band satellite communication systems," *IEEE Transactions on Microwave Theory and Techniques*, vol. 48, no. 12, pp. 2652–2656, Dec. 2000.

[45] B. W. Min and G. M. Rebeiz, "Single-ended and differential Ka-band BiCMOS phased array front-ends," *IEEE Journal of Solid-State Circuits*, vol. 43, no. 10, pp. 2239–2250, Oct. 2008.

[46] E. Adabi Firouzjaei, "Mm-wave phase shifters and switches," Doctoral dissertation, EECS Department, University of California, Berkeley, USA, Dec. 2010. [Online]. Available: `http://www2.eecs.berkeley.edu/Pubs/TechRpts/2010/EECS-2010-163.html`.

[47] J.-J. Hung, L. Dussopt, and G. M. Rebeiz, "Distributed 2- and 3-bit W-band MEMS phase shifters on glass substrates," *IEEE Transactions on Microwave Theory and Techniques*, vol. 52, no. 2, pp. 600–606, Feb. 2004.

[48] D. W. Kang and S. Hong, "A 4-bit CMOS phase shifter using distributed active switches," *IEEE Transactions on Microwave Theory and Techniques*, vol. 55, no. 7, pp. 1476–1483, Jul. 2007.

[49] F. Ellinger, R. Vogt, and W. Bachtold, "Ultracompact reflective-type phase shifter MMIC at C-band with 360° phase-control range for smart antenna combining," *IEEE Journal of Solid-State Circuits*, vol. 37, no. 4, pp. 481–486, Apr. 2002.

[50] T. Liu, K. Han, and J. Zhang, "Design and realization of E-band 4-bit phase shifter MMIC," in *2015 IEEE 16th International Conference on Communication Technology (ICCT)*, Oct. 2015, pp. 661–663.

[51] S. E. Shih, D. W. Duan, O. Fordham, M. Parmar, K. Tornquist, X. Zeng, P. Chang-Chien, and R. Tsai, "A W-band 4-bit phase shifter in multilayer scalable array systems," in *2007 IEEE Compound Semiconductor Integrated Circuits Symposium*, Oct. 2007, pp. 1–4.

[52] C. Mengyi, L. Yang, W. Jiaxing, Z. Jiaxin, M. Xiaohua, and H. Yue, "Ka-band full-360° analog phase shifter with low insertion loss," *Journal of Semiconductors*, vol. 35, no. 10, pp. 105005.1–5, 2014. [Online]. Available: `http://stacks.iop.org/1674-4926/35/i=10/a=105005`.

[53] M. C. Scardelletti, G. E. Ponchak, A. J. Zaman, and R. Q. Lee, "RF MEMS phase shifters and their application in phase array antennas," in *2005 IEEE Annual Wireless and Microwave Technology Conference, 2005.*, Apr. 2005, pp. 191–194.

[54] K. S. K. Yeo, M. J. Lancaster, B. Su, T. W. Button, M. Kittilä, J. Hagberg, and S. Leppävuori, "High frequency thick film BST ferroelectric phase shifter," *Integrated Ferroelectrics*, vol. 61, no. 1, pp. 65–70, 2004.

[55] R. R. Romanofsky and A. H. Qureshi, "A model for ferroelectric phase shifters," *IEEE Transactions on Magnetics*, vol. 36, no. 5, pp. 3491–3494, Sep. 2000.

[56] W. Kim, M. F. Iskander, and C. Tanaka, "High-performance low-cost phase-shifter design based on ferroelectric materials technology," *Electronics Letters*, vol. 40, no. 21, pp. 1345–1347, Oct. 2004.

[57] V. Sherman, K. Astafiev, A. Tagantsev, N. Setter, I. Vendik, and O. Vendik, "Design and investigation of ferroelectric digital phase shifter," in *Microwave Conference, 2001. 31st European*, Sep. 2001, pp. 1–4.

[58] Z. Zhao, X. Wang, K. Choi, C. Lugo, and A. T. Hunt, "Ferroelectric phase shifters at 20 and 30 GHz," *IEEE Transactions on Microwave Theory and Techniques*, vol. 55, no. 2, pp. 430–437, Feb. 2007.

[59] M. Kumar, R. J. Menna, and H.-C. Huang, "Broad-band active phase shifter using dual-gate MESFET," *IEEE Transactions on Microwave Theory and Techniques*, vol. 29, no. 10, pp. 1098–1102, Oct. 1981.

[60] S. J. Kim and N. H. Myung, "A new active phase shifter using a vector sum method," *IEEE Microwave and Guided Wave Letters*, vol. 10, no. 6, pp. 233–235, Jun. 2000.

[61] H. Hayashi and M. Mauraguchi, "An MMIC active phase shifter using a variable resonant circuit," *IEEE Transactions on Microwave Theory and Techniques*, vol. 47, no. 10, pp. 2021–2026, Oct. 1999.

[62] D. Viveiros, D. Consonni, and A. K. Jastrzebski, "A tunable all-pass MMIC active phase shifter," *IEEE Transactions on Microwave Theory and Techniques*, vol. 50, no. 8, pp. 1885–1889, Aug. 2002.

[63] S. R. Ryu, H. Vardhan, B. Banerjee, and R. Prakash, "Continuous active phase shifter design and analysis for millimeter-wave circuits," *IEEE Transactions on Circuits and Systems II: Express Briefs*, vol. 60, no. 10, pp. 627–631, Oct. 2013.

[64] S. P. Sah, X. Yu, and D. Heo, "Design and analysis of a wideband 15-35-GHz quadrature phase shifter with inductive loading," *IEEE Transactions on Microwave Theory and Techniques*, vol. 61, no. 8, pp. 3024–3033, Aug. 2013.

[65] D. Pepe and D. Zito, "Two mm-wave vector modulator active phase shifters with novel IQ generator in 28 nm FDSOI CMOS," Accepted for publication in *IEEE Journal of Solid-State Circuits*, 2016, [Online]. Available: `http://ieeexplore.ieee.org/document/7676347/`.

[66] I. Sarkas, M. Khanpour, A. Tomkins, P. Chevalier, P. Garcia, and S. P. Voinigescu, "W-band 65-nm CMOS and SiGe BiCMOS transmitter and receiver with lumped I-Q phase shifters," in *2009 IEEE Radio Frequency Integrated Circuits Symposium*, Jun. 2009, pp. 441–444.

[67] CST manual: Ports. Available with the CST Microwave Studios. accessed 13.10.2016.

[68] J. C. Hoover and R. E. Tokheim, "Microstrip transmission-line transitions to dielectric-filled waveguide (correspondence)," *IEEE Transactions on Microwave Theory and Techniques*, vol. 15, no. 4, pp. 273–274, Apr. 1967.

[69] H.-W. Yao, A. Abdelmonem, J.-F. Liang, and K. A. Zaki, "Analysis and design of microstrip-to-waveguide transitions," *IEEE Transactions on Microwave Theory and Techniques*, vol. 42, no. 12, pp. 2371–2380, Dec. 1994.

[70] Y. C. Shih, T. N. Ton, and L. Q. Bui, "Waveguide-to-microstrip transitions for millimeter-wave applications," in *1988 IEEE MTT-S International Microwave Symposium Digest*, vol. 1, May 1988, pp. 473–475.

[71] Y.-C. Leong and S. Weinreb, "Full band waveguide-to-microstrip probe transitions," in *1999 IEEE MTT-S International Microwave Symposium Digest (Cat. No.99CH36282)*, vol. 4, Jun. 1999, pp. 1435–1438.

[72] T. Q. Ho and Y. C. Shih, "Spectral-domain analysis of E-plane waveguide to microstrip transitions," *IEEE Transactions on Microwave Theory and Techniques*, vol. 37, no. 2, pp. 388–392, Feb. 1989.

[73] A. U. Zaman, V. Vassilev, P. S. Kildal, and H. Zirath, "Millimeter wave E-plane transition from waveguide to microstrip line with large substrate size related to MMIC integration," *IEEE Microwave and Wireless Components Letters*, vol. 26, no. 7, pp. 481–483, Jul. 2016.

[74] E. S. Li, G. X. Tong, and D. C. Niu, "Full W-band waveguide-to-microstrip transition with new E-plane probe," *IEEE Microwave and Wireless Components Letters*, vol. 23, no. 1, pp. 4–6, Jan. 2013.

[75] Y. Xiao, L. Ye, G. Cai, and Q. H. Liu, "A full Ka-band half height waveguide to microstrip transition," in *2015 Asia-Pacific Microwave Conference (APMC)*, vol. 1, Dec. 2015, pp. 1–3.

[76] TGP2100 datasheet, accessed January 2017. [Online]. Available: `http://www.triquint.com/products/p/TGP2100`.

[77] TriQuint representative Leo Ivriss, private communications to clarify TGP2100 grounding, September 2016. [Online]. Available: `http://www.triquint.com/support`.

[78] TGP2100 S-parameters, accessed January 2017. [Online]. Available: `http://www.triquint.com/products/p/TGP2100`.

[79] Zhou Du, private communication considering the NBL board design, August 2016.